Radio Propagation Channel Characterization and MIMO Over-the-Air Testing

Ji, Yilin

Publication date:
2020

Document Version
Publisher's PDF, also known as Version of record

RADIO PROPAGATION CHANNEL CHARACTERIZATION AND MIMO OVER-THE-AIR TESTING

BY
YILIN JI

DISSERTATION SUBMITTED 2020

AALBORG UNIVERSITY
DENMARK

Radio Propagation Channel Characterization and MIMO Over-the-Air Testing

Ph.D. Dissertation

Yilin Ji

Dissertation submitted Jun 22, 2020

Dissertation submitted: Jun 22, 2020

PhD supervisor: Prof. Gert Frølund Pedersen
Aalborg University

Assistant PhD supervisor: Assoc. Prof. Wei Fan
Aalborg University

PhD committee: Professor Søren Holdt Jensen (chairman)
Aalborg University

Professor Matthias Hein
Ilmenau University of Technology

Professor Thomas Kürner
Technische Universität Braunschweig

PhD Series: Technical Faculty of IT and Design, Aalborg University

Department: Department of Electronic Systems

ISSN (online): 2446-1628
ISBN (online): 978-87-7210-661-8

Published by:
Aalborg University Press
Kroghstræde 3
DK – 9220 Aalborg Ø
Phone: +45 99407140
aauf@forlag.aau.dk
forlag.aau.dk

Printed in Denmark by Rosendahls, 2020

Curriculum Vitae

Yilin Ji

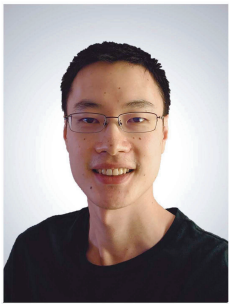

Yilin Ji was born in 1991 in Shanghai, China. He received his B.Sc. degree in Electronics Science and Technology and M.Eng degree in Integrated Circuit Engineering from Tongji University, China, in 2013 and 2016, respectively. In 2013 he had been an exchange student in Universitat Politècnica de Catalunya, Spain, for 6 months. In 2016 he was employed as a guest researcher at the Antennas, Propagation and Millimeter-wave Systems (APMS) section at Aalborg University, Denmark. Since 2017 he has been employed as a Ph.D. fellow in the same section. In 2019, he visited Volvo Cars, Sewden, as a visiting researcher. His main research areas are radio propagation channel and MIMO OTA testing.

Abstract

This thesis mainly covers two research topics, i.e. radio propagation channel characterization and multiple-input multiple-output (MIMO) over-the-air (OTA) testing, for future generation communication systems.

It is expected that millimeter-wave frequency bands and massive MIMO would be part of the key features of future generation communication systems since theoretically, they can offer a huge boost to network capacity. For channel estimation, the potential ultra-wide bandwidth and large array aperture of the systems may cause the far-field and narrowband assumption to be invalid. Therefore, we need to use the spherical wave model instead to reduce model mismatch. Moreover, a channel estimation algorithm is proposed to accelerate the estimation speed without the narrowband assumption. We compared our estimation results with those estimated from the conventional estimation algorithm, and the estimation error is significantly reduced with our approach. Channel statistics such as delay spread and angular spread are also drawn from the estimates of multipath components (MPCs) in connection with the geometry-based stochastic channel model (GSCM).

The use of the spherical wave model allows us to estimate the location of the scatterers in the environment. Those scatterers can be thought of as virtual anchors to estimate the user location with trilateration. Therefore, we also make use of the proposed channel estimation algorithm to localize the user. Since the scatterer locations are estimated directly from measurement data, the map of the environment is not needed, which is the advantage of our localization approach. The results from an experiment including both line-of-sight and non-line-of-sight scenarios show the proposed localization principle works.

Antenna correlation (or its special case, spatial correlation) is an important measure for both antenna design and propagation channels. For example, a lower antenna correlation is always targeted for MIMO antenna design because a lower antenna correlation means more antenna diversity and spatial multiplexing to the MIMO systems as long as the channel can support. The antenna correlation can be calculated from both the power angular spectrum and channel coefficients, which does not necessarily reach the same result.

We used the spread function to express both the power angular spectrum and the channel coefficients, and show their difference analytically.

The prefaded signal synthesis (PFS) and the plane wave synthesis (PWS) are the two main channel emulation methods under the multiprobe anechoic chamber (MPAC) setup for MIMO OTA testing. Though they utilize the same setup, there is a difference in the emulated channels due to their different emulation principles. We derived the joint spatial-temporal correlation function for both methods. The result shows the emulated channel has a cluster-wise Kronecker structure between the joint Doppler-AoD (angle of departure) domain and the AoA (angle of arrival) domain with the PFS method. In comparison, the emulated channel with the PWS method is more faithful to the target channel. Moreover, we showed the PFS method is weak at emulating clusters of small angular spread.

Finally, MIMO OTA testing is also investigated for vehicular communication. Antenna arrays mounted on cars may not have a large effective aperture themselves, but part of the car body may scatter the radiation. Therefore, that part of the car body also needs to be considered as part of the antennas, which enlarges the effective aperture. For the PFS method under the MPAC setup, the test area needs to enclose the whole aperture of the device-under-test (DUT). Since the required number of probe antennas is directly connected to the size of the test area, we studied the required number of probe antennas for cars through simulation. Three measures including the average received power, branch power ratio, and antenna correlation, are used to assess the emulation accuracy. Our results show 16 probe antennas are needed for a two-element shark-fin antenna mounted at the back center of the car roof to achieve low emulation error. The throughput was also measured with the PFS method and, additionally, the wireless cable method as a reference. In the measurement, only 8 probe antennas were used with the PFS method. However, the expected emulation error from the insufficient number of probe antennas did not influence the throughput significantly, since the results from the PFS method were very much in line with those from the wireless cable method.

Resumé

Denne afhandling omhandler overordnet to forskningsemner, karakterisering af radioudbredelse og over-the-air (OTA) test af multiple-input multiple-output (MIMO) systemer for fremtidige generationer af kommunikationssystemer.

Det forventes at millimeterbølge-frekvensbånd og massive MIMO vil være nogle af de vigtigste egenskaber ved fremtidige generationer af kommunikationssystemer, eftersom de teoretisk set kan give en stor forbedring i netværkskapacitet. Den mulige brug af store båndbredder (ultra wideband) og store array-aperturer kan betyde at antagelser om fjernfelt og smalbånd (narrowband) bliver ugyldige i forbindelse med kanalestimering. For at reducere modelfejl er det derfor nødvendigt at bruge en model baseret på kuglebølger. Derudover foreslås der en algoritme som accelererer kanalestimeringen uden at bruge smalbåndsantagelsen. Vi har sammenlignet vores estimeringsresultater med dem opnået ved hjælp af en konventionel estimeringsalgoritme, og estimeringsfejlen er reduceret betydeligt med vores tilgang. Kanalstatistikker såsom delay spread og angular spread er også beregnet ud fra de estimerede multipath components (MPCs) i forbindelse med den såkaldte geometry-based stochastic channel model (GSCM).

Brug af kuglebølgemodellen muliggør estimering af placeringen af spredere i miljøet. Disse spredere kan opfattes som virtuelle ankre i forbindelse med bestemmelse af placeringen af en bruger ved hjælp af trilateration. Derfor bruger vi også den foreslåede algoritme til at lokalisere brugeren. Eftersom placeringen af sprederene estimeres direkte ud fra måledata er der ikke brug for kort over miljøet, hvilket er fordelen med vores lokaliseringstilgang. Resultaterne fra et eksperiment som inkluderer både line-of-sight and non-line-of-sight scenarier viser at det foreslåede princip virker.

Antennekorrelation (eller specialtilfældet spatial korrelation) er en vigtig metrik indenfor både antennedesign og udbredelseskanaler. En lav antennekorrelation er for eksempel altid målet ved MIMO antennedesign idet en lav korrelation resulterer i større antennediversitet og spatial multipleksing i MIMO systemerne, forudsat at kanalen understøtter det. Antennekorrelationen kan beregnes ud fra både power-angular spektret og ud fra kanalko-

efficienter, men giver ikke nødvendigvis det samme resultat. I arbejdet anvendte vi spredingsfunktionen til at udtrykke både power-angular spektret og kanalkoefficienter og viser forskellen analytisk.

Prefaded signal synthesis (PFS) og plane wave synthesis (PWS) er de to vigtigste metoder til kanalemulering i forbindelse med multiprobe anechoic chamber (MPAC) optillinger til MIMO OTA test. Selvom de anvender den samme opstilling af udstyr er der forskel på de emulerede kanaler på grund forskellen i emuleringsprincip. Vi har udledt den spatial-temporære korrelationsfunktion for begge metoder. Resultatet viser at for PFS metoden har den emulerede kanal Kronecker struktur på cluster-niveau imellem Doppler-AoD (angle of departure) domænet og AoA (angle of arrival) domænet. Til sammenligning er de emulerede kanaler under PWS metoden mere tro mod den ønskede kanal. Derudover er det vist, at PFS metoden er svag til at emulere cluster med lille angular spread.

Endelig, blev MIMO OTA testing undersøgt i forbindelse med kommunikation til kørende enheder. Selvom et antennearray monteret på en bil måske ikke selv har et stort apertur, kan dele af bilen sprede udstrålingen. Disse dele af bilen må betragtes som dele af antennerne, og fortørrer således deres effektive apertur. For PFS metoden i en MPAC opstilling er det nødvendigt at testområdet omfatter hele aperturet af enheden under test (device-under-test, DUT). Eftersom det nødvendige antal antenneprober står i direkte forbindelse med størrelsen af testområdet blev det via simuleringer undersøgt hvor mange probeantenner der er nødvendige for biler. Tre metrikker blev brugt til at bedømme emuleringsnøjagtigheden, average received power, branch power ratio, og antennekorrelation. Vores resultater viser at 16 probeantenner er nødvendige for at opnå en lav emuleringsfejl for en to-element hajfinne-antenne monteret centreret bagerst på biltaget. Throughput blev også målt med PFS metoden i tillæg til referencemålinger med wireless cable metoden. Ved målingerne med PFS metoden blev der kun brugt 8 antenneprober, men den forventede emuleringsfejl, grundet det utilstrækkelige antal antenneprober, påvirkede kun throughput lidt, eftersom resultaterne med PFS metoden er tæt på dem opnået med wireless cable metoden.

Contents

Thesis Details

Thesis Title:	Radio Propagation Channel Characterization and MIMO Over-the-Air Testing
PhD Candidate:	Yilin Ji
Supervisors:	Prof. Gert Frølund Pedersen - Aalborg University Assoc. Prof. Wei Fan - Aalborg University

This thesis is submitted as partial fulfilment of the requirements for the degree of Doctor of Philosophy (PhD) from Aalborg University, Denmark. The thesis is compiled as a collection of papers resulting in the main part of the thesis being scientific papers published in, or submitted to, peer-reviewed journals and conferences. The work presented in the thesis is the result of three years of research, in the period June 2017 – May 2020, as a PhD fellow in the Section of Antennas, Propagation and Millimeter-wave Systems (APMS), Department of Electronic Systems, Aalborg University.

The main body of this thesis consist of the following papers:

A. Y. Ji, W. Fan, and G. F. Pedersen, "Channel characterization for wideband large-scale antenna systems based on a low-complexity maximum likelihood estimator", *IEEE Transactions on Wireless Communications*, vol. 17, no. 9, pp. 6018–6028, 2018.

B. Y. Ji, J. Hejselbæk, W. Fan, and G. F. Pedersen, "A Map-Free Indoor Localization Method Using Ultrawideband Large-Scale Array Systems", *IEEE Antennas and Wireless Propagation Letters*, vol. 17, no. 9, pp. 1682–1686, 2018.

C. Y. Ji, W. Fan, P. Kyösti, J. Li, and G. F. Pedersen, "Antenna Correlation under Geometry-Based Stochastic Channel Models", *IEEE Antennas and Wireless Propagation Letters*, vol. 18, no. 12, pp. 2567–2571, 2019.

D. Y. Ji, W. Fan, G. F. Pedersen, and X. Wu, "On Channel Emulation Methods in Multiprobe Anechoic Chamber Setups for Over-the-Air Testing", *IEEE Transactions on Vehicular Technology*, vol. 67, no. 8, pp. 6740–6751, 2018.

E. Y. Ji, W. Fan, M. Nilsson, L. Hentilä, K. Karlsson, F. Tufvesson, and G. F. Pedersen, "Virtual Drive Testing Over-the-Air for Vehicular Communications", *IEEE Transactions on Vehicular Technology*, vol. 69, no. 2, pp. 1203–1213, 2020.

According to the Ministerial Order no. 1039 of August 27, 2013, regarding the PhD Degree § 12, article 4, statements from each co-author about the PhD students contribution to the above-listed papers have been provided to the PhD school for approval prior to the submission of this thesis. These co-author statements have also been presented to the PhD committee and included as a part of their assessment.

In addition to the listed papers as the main content of this thesis, the following papers were also either authored or co-authored during the PhD studies. As these papers are not a part of the main body of this thesis they have not been included in print. The reader is therefore kindly referred to their respective publishing channels as listed hereafter.

1. W. Fan, P. Kyösti, Y. Ji, L. Hentilä, X. Chen, and G. F. Pedersen, "Experimental Evaluation of User Influence on Test Zone Size in Multi-Probe Anechoic Chamber Setups", *IEEE Access*, vol. 5, pp. 18545–18556, 2017.

2. J. Hejselbæk, Y. Ji, W. Fan, and G. F. Pedersen, "Channel Sounding System for MM-Wave Bands and Characterization of Indoor Propagation at 28 GHz", *International Journal of Wireless Information Networks*, vol. 24, no. 3, pp. 204–216, 2017.

3. Y. Ji, W. Fan, and G. F. Pedersen, "Channel estimation using spherical-wave model for indoor LoS and obstructed LoS scenarios" *11th European Conference on Antennas and Propagation (EUCAP 2017)*, 2017.

4. F. Zhang, W. Fan, Y. Ji, M. Gustafsson, T. Jamsa, G. Steinböck, P. Kyösti, and G. F. Pedersen, "Performance testing of massive MIMO base station with multi-probe anechoic chamber setups", *12th European Conference on Antennas and Propagation (EuCAP 2018)*, 2018.

5. A. W. Mbugua, W. Fan, Y. Ji, and G. F. Pedersen, "Millimeter wave multi-user performance evaluation based on measured channels with virtual antenna array channel sounder", *IEEE Access*, vol. 6, pp. 12318–12326, 2018.

6. W. Fan, Y. Ji, F. Zhang, and G. F. Pedersen, "Channel Estimation Algorithms and Their Impact on Wideband Millimeter Wave Channel Characteristics", *2018 2nd URSI Atlantic Radio Science Meeting (AT-RASC)*, 2018.

7. Y. Ji, W. Fan, and G. F. Pedersen, "Wideband Radio Channel Emulation Using Band-stitching Schemes", *14th European Conference on Antennas and Propagation (EuCAP 2020)*, 2020.

8. W. Fan, P. Kyösti, Y. Ji, and G. F. Pedersen, "On Noise and Interference Modeling for Over-the-air Testing of MIMO Terminals", *14th European Conference on Antennas and Propagation (EuCAP 2020)*, 2020.

Preface

Three years of PhD studying comes with tears and joys. I came to Aalborg in 2016 right after I obtained my Master degree in China. Back then, I did not think too much about what to do for the future but one thing was kind of clear to me that if I want to continue my research career, do a PhD. Still cannot say if this is true or not. I started working as a guest researcher in the Antenna Propagation and Millimeter-wave Systems (APMS) section, which was still called APNET when I came at first. I instantly noticed the calm, friendly, but well-organized atmosphere of work and life here in Aalborg because I had been soaked in a completely different one from where I came, competitive, fast-paced, and aggressive, for years. Later when I learned the danish word *Hygge* and *Janteloven*, I found what makes Denmark a place people love. I told myself this is the dream place I want to and will spend a great portion of my life. I guess I was really lucky that both my co-supervisor Wei Fan and main supervisor Gert Frølund Pedersen appreciated my work though my working schedule did not stick to the clock. Thanks for bearing me with that. Later I got the offer of a PhD position. "Think twice before you sign the contract", said a few elderly colleagues to me. I realized I actually got a place to choose on my own instead of just following the flow. Well then, started the new page of my life.

I would like to thank all my colleagues that helped me in the past years for your invaluable input to my research. Our relationships do not stop at work but extend to life. Those fun times are really precious to me. Life-work balance is really important to keep your spirit upright. Also, special thanks to Wei, Jesper, Fengchun, and Jan, who helped me a lot revising the thesis.

Lastly, hope you find the thesis useful.

Yilin Ji
Aalborg University, June 22, 2020

Part I

Introduction

Introduction

1 Introduction

Radio communication technology utilizes radio waves to carry information between two locations. It has been widely used in various applications, e.g. cellular networks, wireless fidelity (WIFI), and Bluetooth. Radio signals are transmitted from a transmitter at one place, propagate in and interact with the environment, and finally being collected at a receiver at another place. This is the fundamental process of radio communication. Compared with wired communication, e.g. landlines and Ethernet, where signals are carried over cables between two locations, radio communication technology brings great convenience to people's daily life and satisfies our ever-growing demands for communication.

As mentioned, radio signals propagate in the environment before reaching the receiver. In the literature, the environment in which radio signals propagate between the transmitter and the receiver is usually termed as radio propagation channel, or in short, channel. Different propagation scenarios, e.g. indoor/outdoor, urban/rural, and terrestrial/satellite, will cause the properties of the channel to vary differently [1–4]. Consequently, received radio signals will also be distorted differently. Here, we give a very simple example of the effect of the distortion. When the propagation takes place in an indoor environment, due to the reflection and diffraction mechanism of radio waves on the walls and other objects indoors, multiple replicas of the same radio signal transmitted from the transmitter will arrive at the receiver at different time. This phenomenon is usually characterized by the delay spread. When the delay spread is larger than the symbol duration, inter-symbol interference (ISI) would occur which makes it difficult to demodulate to get the original symbols at the receiver. Tactics such as inserting a guarding period between adjacent symbols longer than the delay spread and equalization can be used to mitigate the ISI effect. Therefore, to ensure successful transmission and restoration of the original information, it is necessary to know the properties of the channel so that radio signals can be designed accordingly. The study of the channel is called channel characterization in the literature.

Channel characterization has always been conducted actively along with the evolution of radio communication technologies, from low-frequency bands to high-frequency bands, from single-input single-output (SISO) systems to multiple-input multiple-output (MIMO) systems, from generation to generation, etc. Philosophically speaking, the channel is solely governed by the nature of the environment within which radio signals propagate. However, due to the limitation of our measurement systems, we can only observe a segment of the full view of the channel in the time, frequency, or spatial domain. Therefore, in practice people often think of different segments of the channel as different channels even for the same environment. With a huge amount of research conducted on the channel, channel models that are representative of different scenarios and usage can be formulated. A few have been selected by the standardization body as standard channel models [1–4].

Not only are the standard channel models important for designing radio signals, but also they play a vital role in device testing. Once new models of wireless devices, e.g. mobile phones, are under development or being manufactured, it is typically mandatory to test if their radio performance meets the requirement or specification. A straightforward way to test it is to put the device-under-test (DUT) in a live network for different scenarios and measure its real-world performance. This is the so-called field trials [5]. Field trials do tell the true performance of DUTs, but they often suffer from the uncertainty of the environment. The test results may not be repetitive due to, e.g., the weather change and road traffic conditions. To make the testing results representative for real-world scenarios and comparable between different products, an alternate, i.e. virtual drive testing, is often adopted in the industry, which is done in a controllable, repeatable, and reproducible laboratory environment. In virtual drive testing, test signals need to undergo the emulated channels that are generated according to the standard channel models.

Conventionally, virtual drive testing has been done in a conducted manner, where radio signals are fed to the DUT over coaxial cables. With the development of radio communication technologies, MIMO orders may increase significantly for massive MIMO systems which requires accordingly a large number of ports in the channel emulators. Moreover, the design of antenna arrays and baseband units may be highly integrated for millimeter-wave frequencies, which leads to the unavailability of antenna ports on the DUT. Due to these reasons, the whole testing community has been moving to an over-the-air (OTA) manner. However, since the desired radio signals are not guided to the DUT over cables as in the conducted testing, methods to achieve similar effects are needed for the OTA testing. How to emulate a channel over the air according to standard channel models with high fidelity in the test environment becomes the research focus of MIMO OTA testing. Many emulation techniques have been proposed in the literature and selected

in the standard [6] covering different scenarios, such as space-selective channels or isotropic channels. Though channel emulation techniques for OTA testing are more complicated than that for conducted testing, they offer some appealing features such as being non-intrusive to DUTs and providing realistic radio interaction with the DUT as if in real life.

1.1 Different Types of Channel Models with a Focus on the Geometry-Based Stochastic Channel Models

Channel models roughly can be separated into two main types, i.e. the deterministic channel models and the stochastic channel models. The deterministic channel models describe the channel as a deterministic entity once the propagation environment is fixed. A popular method to generate deterministic channels is ray tracing [7]. When the locations of the transmitter and receiver and the detailed geometric and electrical description of the propagation environment are known, rays that imitate specular propagation paths are calculated according to the geometry of the environment. Meanwhile, channel coefficients are calculated according to the propagation mechanism of each path such as reflection and diffraction along with material parameters such as conductivity and permittivity. Other propagation mechanisms that cannot be modelled as specular paths such as diffuse scattering can be added through the effective roughness model after [8]. Another method other than ray tracing is the full wave simulation using the finite-difference time-domain (FDTD) method [9]. This method meshes the whole propagation environment into small cells and calculates the electric field progressively cell-by-cell by solving Maxwell equations. One main drawback of this method is the high computational complexity when it comes to electrically large objects due to a resulting large number of cells. Moreover, when the environment is complicated, it is hard to build the model of the environment and to find proper material parameters for different objects.

The other type is the stochastic channel models. Those channel models describe the channel as a random process associated with some statistics. A very simple stochastic channel model is the independent identically distributed (i.i.d.) Rayleigh channel, where each channel coefficient is a random variable following the complex Gaussian distribution with zero mean and unity variance while being independent of each other. This model is widely used as a benchmark model in, e.g., channel capacity investigation due to its simplicity in channel generation. However, this model is oversimplified and does not represent any real-world propagation scenarios. Correlation-based stochastic channel models add an additional degree of freedom to the i.i.d. Rayleigh channel, i.e. the correlation between channel coefficients. Since channel coefficients are assigned between each transmit antenna and receive antenna, it is interpreted as the spatial correlation of the channel. More intu-

itively, the correlation describes the power angular spectrum on the transmitter and receiver side because power angular spectrum and spatial correlation are Fourier duals. Therefore, correlation-based stochastic channel models can be generated according to a desired power angular spectrum that represents a realistic propagation scenario.

The most widely used stochastic channel model by the standardization body is the geometry-based stochastic channel model (GSCM). It gives a more detailed description of the channel based on the geometry of the propagation environment compared with the correlation-based stochastic channel models. Under the GSCM, propagation paths are randomly drawn from clusters, each of which corresponds to a closely located scatterers in the environment. Those clusters typically have their associated distribution in different domains with specified statistics, e.g. Laplacian distribution in the angular domain and exponential distribution in the delay domain. We can see that the idea is somewhat similar to ray tracing that propagation paths shall be corresponding to physical scatterers in the environment, but their philosophy is different. Ray tracing takes the geometry and electrical properties of the environment and calculates the propagation paths directly, whereas the GSCM is derived based on channel measurements. The so-called multipath components (MPCs), which are essentially the same thing as the propagation paths, are estimated from the measurement. The cluster statistics are then calculated from the MPCs, which are inserted to the GSCM in the end. Therefore, strictly speaking, building a specific GSCM does not require the geometry of the environment beforehand, but it is implicitly reflected by the estimated MPCs. However, it is always beneficial to know the environment beforehand because it helps for measurement planning such as what kind of antennas and arrays shall be used for that environment.

1.1.1 Generic Signal Model of GSCM

Given a specific propagation environment, the underlying paths can be physically mapped in the environment as shown in Fig. 1, and described by parameters in terms of the length of the paths, the departure direction of the paths from the transmitter, the arrival direction of the paths at the receiver, and the rate at which the length of the paths change if anything is moving in the environment. These are represented mathematically by the spread function of the channel as

$$\begin{aligned} \boldsymbol{h}(\tau, v, \boldsymbol{\Omega}^{\mathrm{Tx}}, \boldsymbol{\Omega}^{\mathrm{Rx}}) = \sum_{m=1}^{M} \boldsymbol{A}_m \cdot \delta(\tau - \tau_m) \cdot \delta(v - v_m) \\ \cdot \delta(\boldsymbol{\Omega}^{\mathrm{Tx}} - \boldsymbol{\Omega}_m^{\mathrm{Tx}}) \cdot \delta(\boldsymbol{\Omega}^{\mathrm{Rx}} - \boldsymbol{\Omega}_m^{\mathrm{Rx}}), \end{aligned} \tag{1}$$

where m is the index of the MPCs, and M is the number of MPCs. The

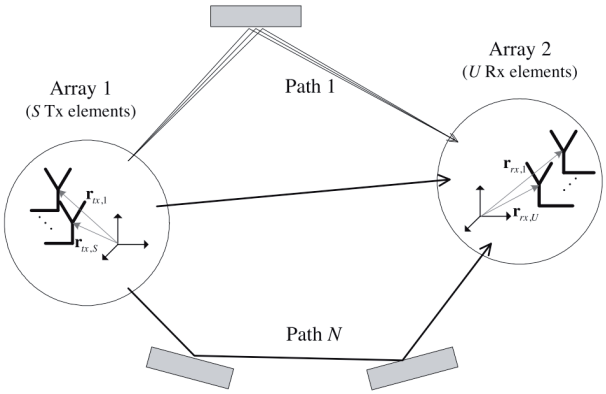

Fig. 1: A diagram showing the basic structure of the radio propagation channel. This figure is taken from "WINNER II" channel models [2, Figure 3-1].

variables τ, v, $\mathbf{\Omega}^{\mathrm{Tx}}$, $\mathbf{\Omega}^{\mathrm{Rx}}$ denote the delay, Doppler frequency, direction of departure (DoD), and direction of arrival (DoA), respectively, with the parameters of the mth MPC as τ_m, v_m, $\mathbf{\Omega}_m^{\mathrm{Tx}}$, $\mathbf{\Omega}_m^{\mathrm{Rx}}$. Note that the DoA and DoD are unit vectors defined inherently as $\mathbf{\Omega} = [\cos\theta \sin\phi, \sin\theta \sin\phi, \cos\phi]$ with θ and ϕ being the elevation and azimuth angle, respectively. Typically, when only two-dimensional channels are considered in the azimuth plane, $\theta = 90^\circ$ is assumed. The term $\delta(\cdot)$ denotes the Dirac delta function. The matrix $\boldsymbol{A}$ in (1) is the polarization matrix that describes how signals attenuate for different polarizations. It is expressed as

$$\boldsymbol{A}_m = \begin{bmatrix} \alpha_m^{\mathrm{VV}} & \alpha_m^{\mathrm{VH}} \\ \alpha_m^{\mathrm{HV}} & \alpha_m^{\mathrm{HH}} \end{bmatrix}, \tag{2}$$

where α_m is the complex amplitude of the mth MPC with its superscripts (V and H) denoting the departure and arrival relation of vertical and horizontal polarization. The full parameter set of the channel can be summarized as

$$\mathbf{\Theta} = \{\boldsymbol{A}_m, \tau_m, v_m, \mathbf{\Omega}_m^{\mathrm{Tx}}, \mathbf{\Omega}_m^{\mathrm{Rx}}\}, \tag{3}$$

for all m. When the channel is dynamic, which is typically the case in high-mobility scenarios, a time dependence can be added to all the parameters in the set as

$$\mathbf{\Theta}(t) = \{\boldsymbol{A}_m(t), \tau_m(t), v_m(t), \mathbf{\Omega}_m^{\mathrm{Tx}}(t), \mathbf{\Omega}_m^{\mathrm{Rx}}(t)\}. \tag{4}$$

In this case, the channel is referred to as a time-variant system. However, if we slice the channel into small pieces of relatively short time durations,

i.e. shorter than the coherence time, the channel observed within that time slot is often assumed quasi-static. In this case, the time-dependence of the parameters is dropped as shown in (3), and the channel is referred to as a time-invariant system. In this thesis, we limit our discussion to time-invariant channels.

The spread function describes the nature of the channel without any specific communication systems incorporated. To make it useful for a communication system, we can further define the so-called channel transfer function. Without loss of generality, given a MIMO system consisting of S Tx antennas and U Rx antennas, the channel transfer function from the sth Tx antenna to the uth Rx antenna at time t and frequency f can be expressed as [10]

$$H_{u,s}(t,f) = \iiiint \begin{bmatrix} F_u^{\mathrm{V}}(\mathbf{\Omega}^{\mathrm{Rx}}) \\ F_u^{\mathrm{H}}(\mathbf{\Omega}^{\mathrm{Rx}}) \end{bmatrix}^T \boldsymbol{h}(\tau, v, \mathbf{\Omega}^{\mathrm{Tx}}, \mathbf{\Omega}^{\mathrm{Rx}}) \begin{bmatrix} F_s^{\mathrm{V}}(\mathbf{\Omega}^{\mathrm{Tx}}) \\ F_s^{\mathrm{H}}(\mathbf{\Omega}^{\mathrm{Tx}}) \end{bmatrix} \cdot \exp(j2\pi v t) \cdot \exp(-j2\pi f \tau)\, \mathrm{d}\tau\, \mathrm{d}v\, \mathrm{d}\mathbf{\Omega}^{\mathrm{Tx}}\, \mathrm{d}\mathbf{\Omega}^{\mathrm{Rx}}, \tag{5}$$

where $F_s^{\mathrm{V}}(\mathbf{\Omega})$ and $F_s^{\mathrm{H}}(\mathbf{\Omega})$ are the antenna radiation pattern of the sth Tx antenna at direction $\mathbf{\Omega}$ for the vertical and horizontal polarization, respectively. Similarly, $F_u^{\mathrm{V}}(\mathbf{\Omega})$ and $F_u^{\mathrm{H}}(\mathbf{\Omega})$ are those for the uth Rx antenna. The antenna field pattern is defined with a common phase center for the respective Tx and Rx antenna arrays. The integration is conducted over the full span of the respective domains of the variables. Taking (1) and (2) into (5) and using the property of the Dirac delta function for integration, (5) can be simplified as

$$H_{u,s}(t,f) = \sum_{m=1}^{M} \begin{bmatrix} F_u^{\mathrm{V}}(\mathbf{\Omega}_m^{\mathrm{Rx}}) \\ F_u^{\mathrm{H}}(\mathbf{\Omega}_m^{\mathrm{Rx}}) \end{bmatrix}^T \begin{bmatrix} \alpha_m^{\mathrm{VV}} & \alpha_m^{\mathrm{VH}} \\ \alpha_m^{\mathrm{HV}} & \alpha_m^{\mathrm{HH}} \end{bmatrix} \begin{bmatrix} F_s^{\mathrm{V}}(\mathbf{\Omega}_m^{\mathrm{Tx}}) \\ F_s^{\mathrm{H}}(\mathbf{\Omega}_m^{\mathrm{Tx}}) \end{bmatrix} \cdot \exp(j2\pi v_m t) \cdot \exp(-j2\pi f \tau_m). \tag{6}$$

Equation (6) is the generic signal model of the channel transfer function defined in the time, frequency, and spatial domain. It can be confusing that the spatial domain is not present in (6), but it is inherent in the antenna radiation pattern in the general form. Given a specific antenna pattern, e.g. isotropic in a very simple case, the radiation pattern can be analytically expressed as

$$F(\mathbf{\Omega}) = \exp\left(j\frac{2\pi}{\lambda}\langle \boldsymbol{r}, \mathbf{\Omega}\rangle\right), \tag{7}$$

where λ denotes the wavelength at the frequency f, $\boldsymbol{r}$ is the location vector of the antenna in the space, $\mathbf{\Omega}$ is the unit direction vector, and $\langle \cdot, \cdot \rangle$ denotes the inner product of two vectors. It can be found in the literature that the time, frequency, and spatial domain are Fourier duals with the Doppler frequency, delay, and direction domain, respectively [10].

1.1.2 Channel Estimation

As mentioned earlier, the GSCM requires the statistics of the channel to complete itself. These statistics are derived from the MPCs existing in the propagation environment. The goal of channel estimation is to estimate the MPCs from the measurement data, and more specifically, to estimate the parameters of the MPCs shown in (3) either partially or fully depending on the specific needs. Here we briefly introduce a fundamental estimation technique that has been employed in many advanced estimation algorithms, i.e. the matched filtering.

Let us assume a very simple case where we have a uniform linear array (ULA) with isotropic elements and a wave coming at a certain angle θ_0. We want to estimate the incident angle of the wave to the ULA. Recall the antenna radiation pattern given in (7), and we can construct the array steering vector with some manipulation as

$$\boldsymbol{c}(\theta) = \left[\exp\left(j\frac{2\pi}{\lambda}d\cos\theta\right), ..., \exp\left(j\frac{2\pi}{\lambda}nd\cos\theta\right), ..., \exp\left(j\frac{2\pi}{\lambda}Nd\cos\theta\right)\right]^T, \tag{8}$$

where $n = [1, ..., N]$ is the index of element out of N total elements and d is the element spacing. Similarly, the array response under the incident wave at angle θ_0 can be easily expressed as

$$\boldsymbol{y} = \alpha_0 \cdot \boldsymbol{c}(\theta_0), \tag{9}$$

where α_0 is the complex amplitude of the wave. The pseudo power angular spectrum can be calculated as

$$p(\theta) = \left|\frac{\boldsymbol{c}(\theta)^* \cdot \boldsymbol{y}}{\|\boldsymbol{c}(\theta)\|}\right|^2, \tag{10}$$

where $(\cdot)^*$, $|\cdot|$, and $\|\cdot\|$ denote conjugate transpose, magnitude operator, and norm operator, respectively. Equation (10) is sometimes called the ambiguity function of a parameter. If a parameter can be well estimated, its ambiguity function should have a shape similar to the Dirac delta function, where the value of the function at the true parameter value is high while the values for the rest candidate parameter values are low. Fig. 2 shows an example of the ambiguity function of a ULA with 10 elements, half-wavelength element spacing, and the incident angle at 90°. When the ambiguity function has such a shape, the value of the parameter can be easily estimated as

$$\hat{\theta} = \arg\max_{\theta} p(\theta). \tag{11}$$

With the estimate $\hat{\theta}$, the estimate of the complex amplitude can be simply calculated as

$$\hat{\alpha}_0 = \frac{\boldsymbol{c}(\hat{\theta})^* \cdot \boldsymbol{y}}{\|\boldsymbol{c}(\hat{\theta})\|^2}. \tag{12}$$

This concludes the estimation problem given in the simple example since both parameters are obtained.

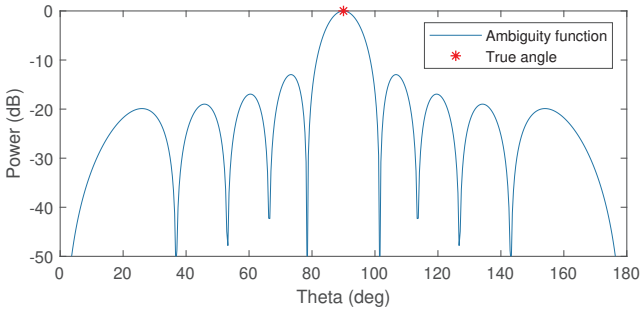

Fig. 2: An example of the ambiguity function of the incident angle for a ULA with 10 elements and half-wavelength element spacing.

In the literature, estimation algorithms include (but are not limited to) Bartlett beamforming [11], multiple signal classification algorithm (MUSIC) [12], estimation of signal parameters via rotational invariant techniques (ESPRIT) [13], space-alternating generalized expectation-maximization (SAGE) [14], and Richter's Maximum likelihood estimation (RiMAX) [15]. Among those, the SAGE algorithm may be the most popular for channel estimation because it not only offers the ability to estimate all the parameters of MPCs as mentioned previously but also runs at low computational complexity.

1.2 An Application of MPCs – Indoor Localizaiton

Navigation brings great convenience to people's daily life. An essential part of navigation is localization. A simple principle of localization is trilateration, where a minimum of three anchors and their associated time of flight is needed to localize a user in the two-dimensional space (four anchors for the three-dimensional space). In outdoor scenarios with open sky, this problem has been well solved with the global positioning system (GPS). However, the GPS service relies on the line-of-sight transmission between the user and the satellites. Due to the blocking of satellite signals in indoor scenarios, it cannot be used in this case. Probably many people have experienced the feeling of being lost in a maze-like building such as a very large museum or industrial campus. Therefore, other methods need to be developed for indoor scenarios.

One solution that has attracted much attention in the research community is the MPC-assisted localization. As discussed earlier, the geometry information of the environment is implicitly registered in the MPCs in terms of parameters such as incident angles and time of flight (delay). Each MPC should correspond to a scatterer in the propagation environment. If we consider those scatterers as virtual anchors, we can utilize them to estimate the location of the user as well. One advantage of this solution is that we do not need to distribute a large number of real anchors in the environment, which is a cost-saving point. Moreover, if each real anchor needs to be wired to a central controller, the cable routing can be cumbersome for technicians. The downside of the MPC-assisted solution is that the estimation accuracy may be lower than that of the real-anchor solution because the richness and diversity of MPCs depend a lot on the specific environment.

For the MPC-assisted localization, the parameters of MPCs can be estimated by the channel estimation algorithms we mentioned in the previous section. The remaining problem is how to translate the estimated MPCs to the location of the user. In the literature, we can find MPC-assisted localization algorithms that need the geometry information (map) of the environment [16] and that do not, i.e. the simultaneous localization and mapping (SLAM) algorithm [17–19].

1.3 Spatial Correlation and Antenna Correlation

Spatial correlation is a second-order statistic of channels. When the channel is assumed wide sense stationary (WSS), the channel can be fully characterized by its second-order statistics, such as spatial correlation and temporal correlation. Recall the Fourier duality, e.g. between spatial domain and direction domain, as mentioned at the end of Section 1.1.1. Similarly, the spatial correlation is the Fourier dual of the power angular spectrum. Therefore, once the spatial correlation of a channel is fixed, the corresponding power angular spectrum is fixed as well.

The relation between the spatial correlation between two spatial locations $(\boldsymbol{r}_1, \boldsymbol{r}_2)$ and the power angular spectrum can be mathematically express as (Note a more detailed expression can be found in Paper C.)

$$\rho(\boldsymbol{r}_1, \boldsymbol{r}_2) = \rho(\Delta\boldsymbol{r}) = \int p(\boldsymbol{\Omega}) \exp\left(j\frac{2\pi}{\lambda}\langle \Delta\boldsymbol{r}, \boldsymbol{\Omega}\rangle\right) \mathrm{d}\boldsymbol{\Omega}, \tag{13}$$

where $p(\boldsymbol{\Omega})$ is the normalized power angular spectrum, and $\Delta\boldsymbol{r} = \boldsymbol{r}_1 - \boldsymbol{r}_2$. The first equation describes the WSS property of the channel in the spatial domain that the spatial correlation is only dependent on the spatial difference but not the absolute location. The second equation indicates the Fourier dual relation. Moreover, it also implicitly assumes uncorrelated scattering (US) in

the direction domain of the channel. The WSS and US assumption often appear together because they are dual assumptions in, e.g., the spatial domain and the direction domain. Similar derivation can be extended between the other dual domains as well. Spatial correlation is not only a statistic that characterizes the channel, but it is also an important measure to quantify the accuracy of channel emulation for MIMO OTA testing that will be discussed in the following sections.

Antenna correlation is a similar concept to spatial correlation except for the phasor term in (13) is replaced by the corresponding antenna field pattern. The antenna correlation between two antennas (u_1, u_2) can be expressed as

$$\rho(u_1, u_2) = \frac{\int p(\mathbf{\Omega}) F_{u_1}(\mathbf{\Omega}) F_{u_2}(\mathbf{\Omega})^* \, \mathrm{d}\mathbf{\Omega}}{\sqrt{\int p(\mathbf{\Omega}) |F_{u_1}(\mathbf{\Omega})|^2 \, \mathrm{d}\mathbf{\Omega}} \sqrt{\int p(\mathbf{\Omega}) |F_{u_2}(\mathbf{\Omega})|^2 \, \mathrm{d}\mathbf{\Omega}}}. \tag{14}$$

With a few manipulations, we can see the spatial correlation is a special case of the antenna correlation given the antenna field pattern is isotropic. Antenna correlation is an important measure for designing MIMO antennas. It is always targeted to have a low antenna correlation between MIMO antennas so that antenna diversity and spatial multiplexing can be exploited.

1.4 MIMO Over-the-Air testing

In the literature, MIMO OTA testing is mainly performed with three setups, i.e. multiprobe anechoic chamber (MPAC) setup, wireless cable setup, and reverberation chamber setup. In the following, we briefly explain the principle of each setup.

1.4.1 Multiprobe Anechoic Chamber Setup

A diagram of the MPAC setup is shown in Fig. 3. The MPAC setup typically consists of several main components, i.e. a radio communication tester, a channel emulator, a power amplifier box, multiple probe antennas, and an anechoic chamber. The radio communication tester work as a transmitter which generates and transmits standard test signals. The test signals are fed to the channel emulator via coaxial cables. The faded test signals are further fed through the power amplifier box to the probe antennas. The probe antennas are located in the anechoic chamber. They are usually uniformly distributed on a circle pointing towards the DUT at the center.

The following is where it differs from the conducted testing. For the conducted testing, all domains of the target channel, i.e. the time domain, the spatial domain on the transmitter side, and the spatial domain on the receiver side, are completely emulated by the channel emulator. However, for the MPAC setup, the spatial domain on the receiver side is emulated by

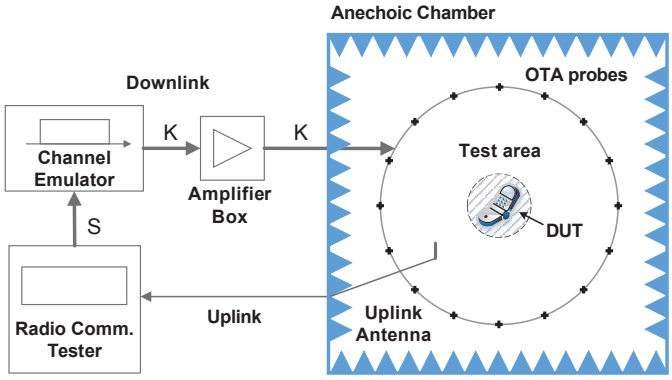

Fig. 3: A diagram of the MPAC setup. This figure is taken from [20].

the channel emulator together with the probe antennas located in different directions pointing towards the test area which encloses the DUT. A trivial example is when the target channel specifies an MPC illuminating the DUT from a certain direction, one can simply put a probe antenna in that direction, and the same can be done with other probe antennas for other MPCs. Note this example is given only for understanding the principle but rarely implemented in practice because the positions of probe antennas are usually fixed beforehand (e.g. uniformly distributed on a circle). The task of the power amplifier box is to compensate for the path loss over the air between the probe antennas and the DUT in the anechoic chamber.

Depending on how exactly the spatial domain on the receiver side of the target channel is emulated with the channel emulator and probe antennas, two methods can be found in the literature, namely the prefaded signal synthesis (PFS) and the plane wave synthesis (PWS). Below we briefly discuss their principles and detailed descriptions can be found in Paper D.

1.4.1.1 Prefaded signal synthesis In the PFS method, the target channel is decomposed into individual clusters. A cluster is a group of MPCs having similar parameters. Taking the 3GPP SCME model [6] for instance, 18 clusters are defined, each of which consists of 20 MPCs with similar angles of departure and arrival. The goal of this method is to reproduce the spatial correlation of each cluster of the target channel at the receiver side in the test area. This is done by changing the power weight assigned to each probe antenna so that the difference of the spatial correlation to the target channel is minimized.

More intuitively, changing the power weight on each probe antenna can

be considered as changing the power angular spectrum in the test area. Essentially, the number of probe antennas is limited in a practical setup, so we may not be able to generate a power angular spectrum the same as the target. However, the aperture of the test area is also limited, so the ability of the DUT to tell the difference between the emulated power angular spectrum and the target is also limited.

Finding the proper power weights for the nth cluster translates to solving an optimization problem which can be formulated as

$$\begin{aligned} &\arg\min_{\boldsymbol{g}_n} \sum_{\boldsymbol{r}_1,\boldsymbol{r}_2} \|\rho(\boldsymbol{r}_1,\boldsymbol{r}_2) - \hat{\rho}(\boldsymbol{r}_1,\boldsymbol{r}_2|\boldsymbol{g}_n)\|^2, \\ &\text{subject to } \|\boldsymbol{g}_n\| = 1, \end{aligned} \tag{15}$$

where $\rho(\boldsymbol{r}_1,\boldsymbol{r}_2)$ is the target spatial correlation (see (13)), $\hat{\rho}(\boldsymbol{r}_1,\boldsymbol{r}_2|\boldsymbol{g}_n)$ is the emulated spatial correlation with $\boldsymbol{g}_n$ as the power angular spectrum, and $(\boldsymbol{r}_1,\boldsymbol{r}_2)$ is any combination of two locations in the test area. Note that since only power weights are considered in this method, setup calibration only needs to be done for the power from different probe antennas to the center of the test area.

1.4.1.2 Plane wave synthesis In the PWS method, the target channel is decomposed to individual MPCs instead of clusters. Taking again the 3GPP SCME model in comparison to the PFS method, a total of $18 \times 20 = 360$ MPCs are emulated separately. To emulate an MPC illuminating the DUT at a certain direction, by setting not only different power but also phases (i.e. complex weights) to each probe antenna, the electromagnetic wave from all probe antennas add up in the test area coherently, and the electric field in the test area approximates that of a plane wave from that direction. The proper complex weights for different probe antennas for the mth MPC are found by minimizing the difference of the electric field to the target channel, and hence it is also an optimization problem which can be formulated as

$$\arg\min_{\boldsymbol{w}_m} \left\| \sum_k w_{m,k} \boldsymbol{F}(\boldsymbol{\Omega}_k^{\text{probe}}) - \boldsymbol{F}(\boldsymbol{\Omega}_m) \right\|^2, \tag{16}$$

where $w_{m,k}$ is the kth element of $\boldsymbol{w}_m$, $\boldsymbol{F}(\boldsymbol{\Omega}_m)$ is the target electric field. Its elements are the radiation field pattern in (7). The term $\boldsymbol{\Omega}_k^{\text{probe}}$ is the direction of the kth probe antenna. Note since both amplitude and phase weights are considered in this method, setup calibration needs to be done for both the power and phases from different probe antennas to the center of the test area, which is more difficult to achieve for a high accuracy and stability compared to the power-only calibration of the PFS method.

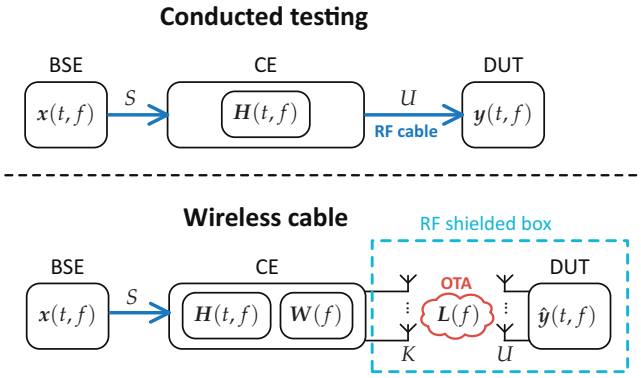

Fig. 4: The block diagrams of the conducted testing method and the wireless cable method. Acronyms: base station emulator (BSE), channel emulator (CE). This figure is taken from Paper E, and detailed description for the symbols can be found there.

1.4.2 Wireless Cable Setup

The wireless cable setup is also known as the radiated two-stage setup. Fig. 4 shows the block diagrams of the conducted testing setup and the wireless cable setup. From the testing principle perspective, the wireless cable setup is very similar to the conducted testing setup except for the conducted process on the DUT side is replaced by an over-the-air process. The end goal of the wireless cable setup is to reproduce exactly the same emulation mechanism of the conducted testing but over the air. The difference of the setup is the cable connection between the channel emulator and the DUT is replaced with radio connection by means of probe antennas connected to the output of the channel emulator and original antennas in the DUT.

The wireless cable setup consists of several main components, i.e. a radio communication tester, a channel emulator, multiple probe antennas, and an anechoic chamber or a radio-frequency (RF) shielding box. The components listed here seem to be quite the same as what is needed for the MPAC setup on paper, but the purpose of using multiple probe antennas in the wireless cable setup is to generate cable-like radio connection with DUTs instead of to emulate the spatial domain on the receiver side of the target channel as for the MPAC setup.

The testing is done in two stages. The first stage is about measuring antenna radiation patterns of DUTs. It can be measured either on-site or off-site, and it is then mathematically embedded to the emulated channel in the channel emulator. The second stage is about establishing cable-like radio connections. Suppose the DUT has 2 antennas equipped, and 4 probe antennas are connected to the output of the channel emulator. The probe antennas are grouped in two pairs with each pair responsible for creating the cable-

like radio connection to an antenna in the DUT. By setting proper complex weights to the probe antennas, the signals of each pair of probe antennas add up constructively on its own target DUT antenna and destructively on the other DUT antenna, which virtually creates a cable-like connection over-the-air to the DUT. The proper complex weights are found by maximizing the power ratio between the beam and the null (i.e. the so-called isolation level). Note that it is necessary but not sufficient to have more probe antennas than DUT antennas (or at least of the same amount) to ensure the proper weights can be found.

As mentioned earlier, the wireless cable setup is only meant to replicate the conducted setup except that cable connection is done over the air. Though the original antennas in the DUT are involved in the testing, they only work as an air interface for receiving signals. Similar to the conducted setup, the effect of their antenna radiation pattern on the target channel can be covered in the channel emulator if known. More detailed explanations of this method can be found in [21].

1.4.3 Reverberation Chamber Setup

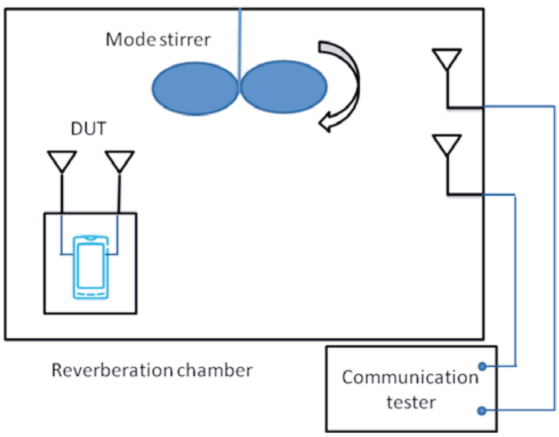

Fig. 5: A diagram of the reverberation chamber setup. This figure is taken from [22].

Fig. 5 shows the diagram of a typical reverberation chamber setup. The reverberation chamber setup consists of two main components, i.e. a radio communication tester and a reverberation chamber with mode stirrers. The radio communication tester generates test signals that are transmitted via probe antennas inside the reverberation chamber. Due to the absence of channel emulators, the channel that test signals go through is completely up to the structure and size of the reverberation chamber. For example, a larger

chamber leads to a larger upper limit of the delay spread of the channel, and the realized delay spread can be controlled by the amount of the loading of absorber in the chamber. By rotating and shifting the stirrers, radio waves are reflected towards various directions in the chamber, and the power angular spectrum on the DUT side thus approximates isotropic and certain Doppler frequency can also be realized [22, 23]. Due to those properties, the reverberation chamber setup is used for Rayleigh channel generation.

The pros and cons of the reverberation chamber setup compared to the MPAC and the wireless cable setup are obvious. The advantages are its lower build cost, simplicity, and robustness, whereas its disadvantage is right the limitation in generating arbitrary spatial channels. To broaden the types of emulated channels in the reverberation chamber setup, some implementations add a channel emulator between the radio communication tester and the probe antennas [22], e.g. to emulate the spatial domain on the transmitter side, or to generate higher doppler frequency than that from shifting stirrers. Nested or connected reverberation chamber setups are also proposed in the literature [24]. A common issue with those implementations is the resulting keyhole effect in the emulated channel that lowers the capacity of the emulated channel [24, 25].

2 Research Objectives

2.1 Channel Estimation for Ultra-Wideband Massive MIMO Systems

For the upcoming fifth-generation (5G) communication system or future generations, it has been predicted that several features, including massive MIMO systems and millimeter wave, would be essential to increase channel capacity. However, due to the large array aperture and ultra-wide bandwidth of those systems, two assumptions that are conventionally made for channel estimation may not hold anymore, i.e. the far field assumption and the narrowband assumption [26].

The far field assumption is given based on the Fraunhofer distance $2D^2/\lambda$, where D is the array aperture. When scatterers get so close to the array that the distance is far below the Fraunhofer distance, the wavefront across the array aperture cannot be approximated to be plane. Otherwise, a huge model mismatch would occur which leads to severe estimation error. Therefore, a spherical wave signal model [27] should replace the conventional plane wave signal model in this case.

The narrowband assumption is described with the condition $D/\lambda \ll f/B$, where B is the bandwidth. With a bit of manipulation on the condition, one can find it simply states the time for a wave to pass through the whole array

aperture, i.e. D/c with c being the speed of light, shall be much smaller than the delay resolution, i.e. $1/B$. However, for ultra-wideband large-scale array systems, this can be violated. In this case the array steering vector needs to be calculated for each frequency in the band instead of only at the center frequency for channel estimation.

The narrowband assumption also allows for the space-alternating mechanism of the SAGE algorithm [28] that significantly accelerates the estimation process. It allows us to break down a multi-dimensional joint estimation problem to several one-dimensional recursive estimation problems. This reduces the computational complexity considerably. The space-alternating mechanism requires that the joint likelihood function of different parameters can be factorized into the likelihood functions of individual parameters. An example of the joint likelihood function between the delay τ and angular θ domain with and without the narrowband assumption is shown in Fig. 6. The joint likelihood function $p(\theta, \tau)$ in Fig. 6(a) can be factorized as $p(\theta) \cdot p(\tau)$, whereas that in Fig. 6(b) can not.

Without the narrowband assumption, we need to find a way to decouple the joint likelihood function so that we can still lower the computational complexity. We introduced an initialization step where measurement data at a single frequency of the highest signal-to-noise ratio is selected. The estimation of the angle becomes independent of delay for that frequency. The delay is then estimated with respect to the estimated angle. With the initial estimates, we can significantly reduce the size of the search space for the joint angle-delay estimation at a later step. Note that the joint estimation is inevitable if we want to make full use of the measurement at different frequencies to reach a more accurate estimate. Therefore, the goal of the initialization step is, as mentioned, to reduce the size of the search space for the following joint estimation. This is also how the computational complexity is reduced in our work. The corresponding work is presented in Paper A.

2.2 Localization with Scatterer Location Estimated from Spherical Wavefront

Previously in Section 2.1, we mentioned that when the far field assumption is invalid, we should use the spherical wave signal model for channel estimation to mitigate model mismatch. In return, the spherical wavefront allows us to estimate an additional parameter of MPCs, i.e. the distance of the scatterer to the array aperture. Together with the angular information of the MPC, we can obtain the scatterer location associated with that MPC. The estimated scatterers can then be used as virtual anchors in the environment, and help to estimate the user location through trilateration.

In order to make this idea work, there are several requirements. According to the principle of trilateration, the links between the anchors and the

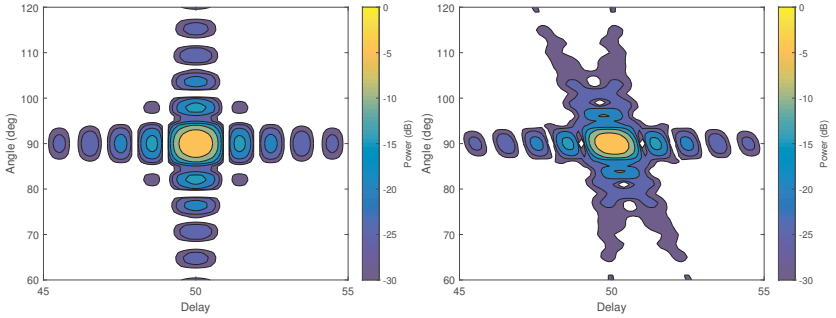

Fig. 6: An example of the joint likelihood function between the delay and angular domain (a) with and (b) without the narrowband assumption.

user need to be line-of-sight. However, this cannot be guaranteed by the estimate from the spherical wavefront. Consider a case where a point source (the user) radiates towards a wall, and the reflected wave is received by the array aperture. Due to the flatness of the wall, the spherical wavefront that departed from the point source may be preserved after the (specular) reflection. In this case, the estimate of the scatterer location would correspond to the image of the point source, which is symmetric with respect to the wall, instead of the intercept on the wall. Moreover, only MPCs of bounce order up to one, i.e. line-of-sight paths, single reflection paths, and single diffraction paths, can be used in this scheme because the estimated scatterers are those closest to the array aperture along the MPCs. For higher bounce-order MPCs, the links between the estimated scatterers and the user would not be line-of-sight. However, with those limitations in mind, we still want to see if this idea works or to which extent it works. The corresponding work is presented in Paper B.

2.3 Antenna Correlation from Power Angular Spectra and Channel Coefficients Perspective

As discussed in Section 1.3, antenna correlation (or its special case, spatial correlation) is an important measure in both antenna design and propagation channel area. Antenna correlation can be calculated with (14) given the power angular spectrum and antenna field pattern. However, it is also possible to calculate the antenna correlation with the channel coefficients given in (6). The corresponding equation can be written as

$$\rho(u_1, u_2|s) = \frac{cov\{H_{u_1,s}, H_{u_2,s}\}}{\sqrt{var\{H_{u_1,s}\}} \cdot \sqrt{var\{H_{u_2,s}\}}}, \tag{17}$$

where $cov\{\cdot\}$ and $var\{\cdot\}$ are the covariance and variance operator, respectively. We can see that (17) is dependent on the sth antenna on the other end of the link, which is different from (14). It is not very straightforward to conclude that if the two equations are equivalent or not just by comparing (14) and (17). Therefore, we started from the common ground between them, i.e. the spread function (1), from which both power angular spectra and channel coefficients can be derived, to find the difference between them. The corresponding work is presented in Paper C.

2.4 Difference Between the PFS and PWS Method

In Section 1.4.1, we have briefly discussed the emulation principles of the PFS and PWS method. In short, the PFS method emulates the second-order statistics of each cluster of the target channel, whereas the PWS method emulates the instantaneous field of each path of the target channel. The different emulation principles actually cause some differences in the properties of the emulated channel even when both methods take exactly the same target channel for emulation. Let us assume the target channel is a single cluster, or equivalently, the nth cluster of a multi-cluster channel. The signal model of the emulated channel for the PFS and the PWS method can be respectively expressed as (Paper D)

$$\begin{aligned}\hat{H}^{\mathrm{PFS}}_{u,s,n}(t,f) = &\sqrt{\frac{P_n}{M}}\sum_{k=1}^{K}\sum_{m=1}^{M} F^{\mathrm{Tx}}_{s}(\varphi_{n,m})\cdot F^{\mathrm{Rx}}_{u}(\phi^{\mathrm{OTA}}_{k})\cdot\sqrt{g_{n,k}}\\ &\cdot\exp(j2\pi\vartheta_{n,m}t + j\Phi_{n,m,k})\cdot\exp(-j2\pi f\tau_n), \qquad (18)\\ \hat{H}^{\mathrm{PWS}}_{u,s,n}(t,f) = &\sqrt{\frac{P_n}{M}}\sum_{m=1}^{M}\sum_{k=1}^{K} F^{\mathrm{Tx}}_{s}(\varphi_{n,m})\cdot F^{\mathrm{Rx}}_{u}(\phi^{\mathrm{OTA}}_{k})\cdot w_{n,m,k}\\ &\cdot\exp(j2\pi\vartheta_{n,m}t + j\Phi_{n,m})\cdot\exp(-j2\pi f\tau_n). \qquad (19)\end{aligned}$$

Comparing (18) and (19), we can find that the initial phase of the mth MPC for the PFS method $\Phi_{n,m,k}$ is independent between different probe antennas, whereas that of the PWS method $\Phi_{n,m}$ is the same for all probe antennas. This makes the spatial correlation on the receiver side being decoupled from that on the transmitter side with the PFS method. In other words, the power angular spectrum on the receiver side is independent of that on the transmitter side. The effect of that is that each cluster emulated with the PFS method has a Kronecker structure between the joint Doppler-DoD domain and the DoA domain.

Moreover, it is difficult for the PFS method to emulate clusters of small angular spread. An extreme example is that the target channel is a single MPC coming from the direction in the middle of two adjacent probe antennas. This case can be well emulated by the PWS method, but not by the PFS

method. To justify those differences in the emulated channels with the PFS and PWS method under the same MPAC setup, i.e. the same configuration of probe antennas, we have derived the joint temporal-spatial correlation for both methods from their signal models, and demonstrated with the power angular spectra. The corresponding work is presented in Paper D.

2.5 MIMO OTA Testing for Cars

With the growth of the vehicle-to-everything (V2X) service, the need for vehicular communication testing increases significantly. However, MIMO OTA testing methods have been mainly developed for DUTs of small form factors, such as mobile phones. Taking the MPAC setup for instance, a test area of 0.85λ in diameter can be achieved with 8 probe antennas [6], which translates to a diameter of about 12 cm at 2 GHz. According to the cut-off properties of spherical wave modes [29], the size of the test area is proportional to the number of probe antennas for two-dimensional (2D) channel models, and quadratic for three-dimensional (3D) channel models.

When vehicular antennas, e.g. shark-fin antennas, operate, the body of cars may scatter the radio signals as well. This behaviour can be characterized by the distribution of the induced surface current on the car body. When this happens, the part of the car body where the current is distributed needs to be considered as part of the antennas, which enlarges the effective aperture of the antennas (i.e. the size of the DUT). However, different mounting positions and antenna radiation patterns will result in different current distributions on the car body. Potentially, the effective aperture of the antennas may be as big as the whole car. However, if the current distribution is confined in a small area surrounding the antennas, we only need to generate a teat area large enough to enclose that area.

We want to investigate the required size of the test area, or equivalently, the required number of probe antennas for car testing under the MPAC setup with the PFS method. The emulation accuracy is assessed by measures including the average received power, branch power ratio, and antenna correlation on the DUT side. The synthetic MPAC setup, which is a simulation framework, is adopted in our work. With this simulation framework, we can calculate those measures for arbitrary DUTs under MPAC setups with different numbers of probe antennas given the DUT antenna pattern as the input. In our work, different DUT antenna configurations are considered, e.g. different mounting positions on the car roof, to study their effect on the emulation accuracy.

In the standard [6], the absolute throughput framework is adopted to verify the throughput measured with different test methods, where results from the conducted testing are used as a reference. In our work, we measure the throughput with the PFS method and the wireless cable method to cross-

check the validity of our results. The corresponding work is presented in Paper E.

3 Contributions

This section presents the main contributions of this thesis together with brief summaries of the motivation, work and findings of the papers included in Part II.

3.1 Paper A

Channel Characterization for Wideband Large-Scale Antenna Systems Based on a Low-Complexity Maximum Likelihood Estimator
Yilin Ji, Wei Fan, and Gert Frølund Pedersen
Published in the *IEEE Transactions on Wireless Communications*, Vol. 17, No. 9, pp. 6018–6028, 2018.

3.1.1 Motivation

Two assumptions usually adopted for channel estimation are potentially violated for wideband large-scale antenna array systems, namely the far-field assumption and the narrowband assumption. With these two assumptions violated, model mismatch occurs in the estimation which leads to severe estimation errors. Moreover, the essential requirement of doing the space-alternating process for the conventional space-alternating generalized expectation maximization (SAGE) algorithm is unfulfilled, which results in a huge degradation in algorithm efficiency. Therefore, we need to define a suitable signal model to mitigate the estimation errors, and develop a modification based on existing estimation algorithms to estimate channel parameters efficiently.

3.1.2 Paper Content

We define a wideband spherical-wavefront signal model for wideband large-scale antenna array systems. With this signal model, an additional parameter that is the locations of the last-bounce scatterers can be estimated. The signal model is inserted in the conventional maximum likelihood estimator. To constrain the computation with practical complexity, the whole estimation process is recursive, and only one multipath component is estimated at a time. A successive interference cancellation process is included to reduce the interference from previously estimated multipath components. The estimates are obtained by a coarse-to-fine search.

To further accelerate the estimation speed, an initialization step is performed to get a good initial guess of the parameters of the multipath components, and hence reducing the number of search candidates. Moreover, the reason why the space-alternating process of the SAGE algorithm cannot be done is explained. A measurement campaign is introduced, and the collected data are processed with the proposed estimation algorithm. To visualize the multipath components in the channel, a so-called measurement-based ray tracing is done and the trajectories of the multipath components are shown in the environment.

3.1.3 Main Results

It is shown that the estimation errors due to the model mismatch are greatly reduced compared to the conventional SAGE algorithm. This is also shown from different aspects in terms of reconstructed power delay-angle spectra, power extraction rate, Akaike information criterion, and meaningful MPC trajectories in the channel mapped to the environment.

3.2 Paper B

A Map-Free Indoor Localization Method Using Ultrawideband Large-Scale Array Systems
Yilin Ji, Johannes Hejselbæk, Wei Fan, and Gert Frølund Pedersen
Published in the *IEEE Antennas and Wireless Propagation Letters*, Vol. 17, No. 9, pp. 1682–1686, 2018.

3.2.1 Motivation

The global positioning system (GPS) has shown to be the most popular method for outdoor localization. However, its performance degrades significantly for indoor localization due to the blocking of signals. In the literature, many other methods have been proposed for the indoor case, but most of them require the map or floor plan of the interior to perform localization. Acquiring that information can be cumbersome due to practical issues. In this paper, we try to develop a method that does not need the map of the environment but still can estimate the location of users.

3.2.2 Paper Content

The basic idea of this method is still trilateration, which requires at least three sources and associated time-of-flight to localize a target in a two-dimensional space. However, when radio signal propagates indoors, objects such as furniture behave as scatterers due to reflection, diffraction, and scattering. Those scatterers can be thought of as secondary transmitters besides the real one.

With the help of the channel estimation algorithm proposed in Paper A, we can estimate the location of those secondary transmitters. Therefore, even when we only have one real transmitter in the indoor environment, the conventional trilateration can still be used to localize the target, given the transmitter is a wideband large-scale array system. A measurement campaign is introduced, and the collected data are processed with the estimation algorithm proposed in Paper A. The location of the target is estimated further by trilateration with the location of the real and secondary transmitters.

3.2.3 Main Results

During the measurements, the target is moving step-by-step from line-of-sight positions to none-line-of-sight positions with respect to the transmitter. The estimated locations of the target are compared to its true locations recored beforehand for all steps. The results show that the estimation error increases as the target moves to the none-line-of-sight region, but the majority of the estimation error are well below 30 cm (given the distance resolution of the measurement is 7.5 cm). Moreover, the locations of the estimated secondary transmitters (scatterers) are visualized on the map to illustrate the localization process.

3.3 Paper C

Antenna Correlation under Geometry-Based Stochastic Channel Models
Yilin Ji, Wei Fan, Pekka Kyösti, Jinxing Li, and Gert Frølund Pedersen
Published in the *IEEE Antennas and Wireless Propagation Letters*, Vol. 18, No. 12, pp. 2567–2571, 2019.

3.3.1 Motivation

The measure, antenna correlation, is often used in both the antenna design and propagation channel area. Each area has its conventional way of calculating it, i.e. from angular power spectrum and channel transfer function. The equivalence of the two ways is not obvious by directly looking at their expressions. In this paper, we try to further derive both expressions to arrive on a common ground, and bridge the gap between its definitions in the two areas.

3.3.2 Paper Content

The expressions for antenna correlation from both angular power spectrum and channel transfer function are presented. The connection between the two is established with the spread function, which is the kernel of channel. With a few steps of derivation, both expressions are instead represented in

terms of the spread function. It shows the difference between the two original expressions is only caused by how the antenna embedding assumption is set.

3.3.3 Main Results

The two original expressions for antenna correlation from angular power spectrum and channel transfer function are both represented in terms of the spread function. In channel transfer function, the antenna radiation pattern at both ends of the link, i.e. the transmitter and the receiver, is taken into account, whereas angular power spectrum typically just describes the nature of channel, and antenna radiation pattern is not included. This is where the discrepancy arises between the two ways of calculating. With this explained, the standard 3GPP spatial channel model extended (SCME) and two specific antenna pattern are taken into the calculation to show the difference in the results numerically.

3.4 Paper D

On Channel Emulation Methods in Multiprobe Anechoic Chamber Setups for Over-the-Air Testing
Yilin Ji, Wei Fan, Gert Frølund Pedersen, and Xingfeng Wu
Published in the *IEEE Transactions on Vehicular Technology*, Vol. 67, No. 8, pp. 6740–6751, 2018.

3.4.1 Motivation

In the current standard, two main MIMO over-the-air (OTA) testing methods are adopted under the category multiprobe anechoic chamber (MPAC) setup, namely the prefaded signal synthesis (PFS) and the plane wave synthesis (PWS). Both methods are designed to emulate spatial channel models. Though the testing setups of the two methods are quite similar, the detailed implementation are slightly different. In this paper, we try to study the effect of the difference in the emulated channel.

3.4.2 Paper Content

The signal models for the PFS and the PWS method are both presented. Besides, the emulation principles of the two methods are also revisited. According to the testing standard, the goal of channel emulation is to reproduce the second-order statistics of the target channel. Therefore, we derive the joint spatial-temporal correlation function (STCF) of the emulated channel, and compare them with the STCF of the target channel. The pros and cons of each method are also discussed and illustrated. The emulation accuracy measured by the spatial correlation function between the two methods

is shown numerically for the same target channel. The effect of the different emulation mechanism of the two methods is also demonstrated in terms of power angular spectra.

3.4.3 Main Results

The emulation of the PFS method is cluster-based, whereas that of the PWS method is ray-based. The calibration for the PFS method is less requiring compared to the PWS method, since the PFS method only requires power calibration for each OTA probe in the test area whereas the PWS method requires both power and phase calibration. In return, the PWS method potentially provides higher emulation accuracy especially for small cluster angular spread cases with the same testing setup, e.g. with the same number of OTA probes. From the STCF perspective, we also show that due to the difference in emulation mechanism, the emulated channel of the PWS method follows the target channel precisely, whereas the emulated channel of the PFS method has a Kronecker structure which leads to the joint power angle of departure (AoD) and Doppler frequency spectrum being independent on the power angle of arrival (AoA) spectrum within a cluster. This independence is shown with numerical examples between the AoA and the AoD domain.

3.5 Paper E

Virtual Drive Testing Over-the-Air for Vehicular Communications
Yilin Ji, Wei Fan, Mikael Nilsson, Lassi Hentilä, Kristian Karlsson, Fredrik Tufvesson, and Gert Frølund Pedersen
Published in the *IEEE Transactions on Vehicular Technology*, Vol. 69, No. 2, pp. 1203–1213, 2020.

3.5.1 Motivation

With the growing interest in vehicle-to-everything (V2X) communication, testing of wireless communication technology equipped on cars begins to draw attention in the industry. The OTA testing methods currently available in the literature and standard are mainly verified for small-scale objects such as mobile phones and laptops. Therefore, there is a strong need to verify if those methods are valid for large-scale objects like cars as well. To do that, an investigation on two standardized OTA testing methods, i.e. the PFS method and the wireless cable method, for cars is performed.

3.5.2 Paper Content

The emulation principles of the two methods are revisited. The sufficient number of OTA probes for the PFS method is investigated in terms of emu-

lation accuracy for different sizes of the device-under-test (DUT). The emulation accuracy is measured as the deviation to the target averaged received power (channel gain), branch power ratio, and spatial correlation. A measurement campaign is introduced which includes both the PFS method and the wireless cable method. For the wireless cable method, isolation levels achieved in the measurements are shown. Throughput results from both methods are shown for comparison.

3.5.3 Main Results

DUTs with three different sizes are chosen, i.e. one shark-fin antenna on a metal plate, one shark-fin antenna on a car, and two shark-fin antennas distantly mounted on a car. The standard SCME channel model is used as the target channel. According to the theory of the PFS method, the larger the test area is, the more OTA probes are needed to keep the fidelity of the emulated channel in the whole test area. This is justified with the simulation showing 8 OTA probes is sufficient for the first DUT size (smallest), and 16 and 32 OTA probes are needed for the second (medium) and third (largest) DUT size, respectively. For the throughput measurements with the PFS method, 8 OTA probes are used for all three differently-sized DUTs. However, no obvious difference in the results is seen compared with those with the wireless cable method.

4 Conclusion

The main scope of this thesis is two-fold including radio propagation channel and MIMO OTA testing. In total five papers are covered in this thesis including channel estimation for ultra-wideband large-scale array systems (Paper A), MPC-assisted localization (Paper B), a review on antenna correlation (Paper C), a comparison between the PFS and PWS method for MIMO OTA testing (Paper D), and MIMO OTA testing for cars (Paper E).

In Paper A, the results show that the use of the spherical wave model reduced the estimation error significantly compared to the plane wave model. The proposed estimation algorithm also keeps the computation complexity at a relatively low level. In Paper B, the scatterer locations are estimated with the estimation algorithm proposed in Paper A. The results from an experiment show that the idea of using scatterers as virtual anchors works with the localization error up to four times the distance resolution of the measurement setup. Paper C provides some mathematic derivation for the metric antenna correlation, which connects the power angular spectrum and channel transfer function through the spread function of the channel. The principles of the PFS and the PWS method for the MPAC setup are introduced in Paper D, and a Kronecker structure of the emulated clusters is found for the PFS method.

It is also shown that the PWS method outperforms the PFS method in terms of emulation accuracy. Lastly, the PFS method and the wireless cable method are investigated for vehicular testing scenarios in Paper E. Simulation shows 16 probe antennas are needed to achieve high emulation accuracy with the PFS method due to the large size of the car. However, the throughput results measured with the PFS method with fewer probe antennas, i.e. 8 probe antennas, are in line with those measured with the wireless cable method.

References

[1] 3GPP, "Spatial channel model for Multiple Input Multiple Output (MIMO) simulations," Tech. Rep. 3GPP TR 25.996 V12.0.0, 2014.

[2] WINNER, "WINNER II Channel Models: Part I Channel Models," Tech. Rep. D1.1.2 V1.2, 2007. [Online]. Available: http://projects.celtic-initiative.org/WINNER+/WINNER2-Deliverables/D4.6.1.pdf

[3] D. S. Baum, J. Hansen, G. D. Galdo, and M. Milojevic, "An Interim Channel Model for Beyond-3G Systems," *Vehicular Technology Conference, 2005. VTC 2005-Spring. 2005 IEEE 61st*, vol. 5, pp. 3132–3136, 2005.

[4] 3GPP, "Study on channel model for frequencies from 0.5 to 100 GHz," Tech. Rep. 3GPP TR 38.901 V14.0.0, 2017. [Online]. Available: http://www.etsi.org/standards-search

[5] W. Fan, L. Hentila, F. Zhang, P. Kyosti, and G. F. Pedersen, "Virtual Drive Testing of Adaptive Antenna Systems in Dynamic Propagation Scenarios for Vehicle Communications," *IEEE Access*, vol. 6, pp. 7829–7838, 2018.

[6] 3GPP, "Verification of radiated multi-antenna reception performance of User Equipment (UE)," Tech. Rep. 3GPP TR 37.977 V15.0.0, 2018.

[7] G. E. Corazza, V. Degli-Esposti, M. Frullone, and G. Riva, "A characterization of indoor space and frequency diversity by ray-tracing modeling," *IEEE Journal on Selected Areas in Communications*, vol. 14, no. 3, pp. 411–419, 1996.

[8] V. Degli-Esposti, "A diffuse scattering model for urban propagation prediction," *IEEE Transactions on Antennas and Propagation*, vol. 49, no. 7, pp. 1111–1113, 2001.

[9] S. S. Zhekov, O. Franek, and G. F. Pedersen, "Numerical modeling of indoor propagation using fdtd method with spatial averaging," *IEEE Transactions on Vehicular Technology*, vol. 67, no. 9, pp. 7984–7993, 2018.

[10] B. H. Fleury, "First- and second-order characterization of direction dispersion and space selectivity in the radio channel," *IEEE Transactions on Information Theory*, vol. 46, no. 6, pp. 2027–2044, 2000.

[11] M. S. Bartlett, "Smoothing Periodograms from Time-Series with Continuous Spectra," *Nature*, vol. 161, pp. 686–687, 1948.

[12] R. Schmidt, "Multiple emitter location and signal parameter estimation," *IEEE Transactions on Antennas and Propagation*, vol. 34, no. 3, pp. 276–280, 1986.

[13] R. Roy and T. Kailath, "ESPRIT-Estimation of Signal Parameters Via Rotational Invariance Techniques," *IEEE Transactions on Acoustics, Speech, and Signal Processing*, vol. 37, no. 7, pp. 984–995, 1989.

[14] B. H. Fleury, M. Tschudin, R. Heddergott, D. Dahlhaus, and K. I. Pedersen, "Channel parameter estimation in mobile radio environments using the SAGE algorithm," *IEEE Journal on Selected Areas in Communications*, vol. 17, no. 3, pp. 434–450, 1999.

[15] A. Richter, "Estimation of Radio Channel Parameters : Models and Algorithms," Ph.D. dissertation, 2005.

[16] P. Meissner, D. Arnitz, T. Gigl, and K. Witrisal, "Analysis of an indoor UWB channel for multipath-aided localization," *Proceedings - IEEE International Conference on Ultra-Wideband*, pp. 565–569, 2011.

[17] T. Bailey and H. Durrant-Whyte, "Simultaneous localization and mapping (SLAM): Part I," *IEEE Robotics and Automation Magazine*, vol. 13, no. 2, pp. 99–110, 2006.

[18] C. Gentner and T. Jost, "Indoor positioning using time difference of arrival between multipath components," *International Conference on Indoor Positioning and Indoor Navigation*, no. October, pp. 1–10, 2013.

[19] K. Witrisal, P. Meissner, E. Leitinger, Y. Shen, C. Gustafson, F. Tufvesson, K. Haneda, D. Dardari, A. F. Molisch, A. Conti, and M. Z. Win, "High-accuracy localization for assisted living: 5G systems will turn multipath channels from foe to friend," *IEEE Signal Processing Magazine*, vol. 33, no. 2, pp. 59–70, 2016.

[20] W. Fan, P. Kyösti, J.-P. Nuutinen, À. O. Martínez, J. Ø. Nielsen, and G. F. Pedersen, "Generating spatial channel models in multi-probe anechoic chamber setups," in *Vehicular Technology Conference (VTC Spring), 2016 IEEE 83rd*, 2016, pp. 1–5.

[21] W. Fan, P. Kyösti, L. Hentilä, and G. F. Pedersen, "MIMO Terminal Performance Evaluation With a Novel Wireless Cable Method," *IEEE Transactions on Antennas and Propagation*, vol. 65, no. 9, pp. 4803–4814, 2017. [Online]. Available: http://ieeexplore.ieee.org/document/7967858/

[22] X. Chen, J. Tang, T. Li, S. Zhu, Y. Ren, Z. Zhang, and A. Zhang, "Reverberation Chambers for Over-the-Air Tests: An Overview of Two Decades of Research," *IEEE Access*, vol. 6, pp. 49 129–49 143, 2018. [Online]. Available: https://ieeexplore.ieee.org/document/8447191/

[23] D. Micheli, M. Barazzetta, R. Diamanti, P. Obino, R. Lattanzi, L. Bastianelli, V. M. Primiani, and F. Moglie, "Over-The-air tests of high-speed moving LTE users in a reverberation chamber," *IEEE Transactions on Vehicular Technology*, vol. 67, no. 5, pp. 4340–4349, 2018.

[24] C. Orlenius and M. Andersson, "Repeatable performance measurements of MIMO systems in connected reverberation chambers with controlled keyhole effect," *Radioengineering*, vol. 18, no. 4, pp. 454–459, 2009.

[25] BLUETEST, "Testing Communication System Performance in Reverberation Chamber," Tech. Rep.

[26] H. Krim and M. Viberg, "Two decades of array signal processing research: The parametric approach," *IEEE Signal Processing Magazine*, vol. 13, no. 4, pp. 67–94, 1996.

[27] Y. Ji, W. Fan, and G. F. Pedersen, "Near-Field Signal Model for Large-Scale Uniform Circular Array and Its Experimental Validation," *IEEE Antennas and Wireless Propagation Letters*, vol. 16, pp. 1237–1240, 2017.

[28] B. H. Fleury, P. Jourdan, and A. Stucki, "High-resolution channel parameter estimation for MIMO applications using the SAGE algorithm," in *2002 International Zurich Seminar on Broadband Communications Access - Transmission - Networking (Cat. No.02TH8599)*, 2002, pp. 30.1–30.9.

[29] A. Khatun, T. Laitinen, V. M. Kolmonen, and P. Vainikainen, "Dependence of error level on the number of probes in over-the-air multiprobe test systems," *International Journal of Antennas and Propagation*, vol. 2012, 2012.

Part II

Papers

Paper A

Channel Characterization for Wideband Large-Scale Antenna Systems Based on a Low-Complexity Maximum Likelihood Estimator

Yilin Ji, Wei Fan, and Gert Frølund Pedersen

The paper has been published in the
IEEE Transactions on Wireless Communications Vol. 17, No. 9, pp. 6018–6028, 2018.

The layout has been revised.

Abstract

Wideband large-scale array systems operating at millimeter-wave bands are expected to play a key role in future communication systems. It is recommended by standardization groups to use spherical-wave models (SWMs) to characterize the channel in near-field cases because of the large array apertures and the small cell size. However, this feature is not widely reflected in channel models yet, mainly due to the high computational complexity of SWMs compared to that of the conventional plane-wave model (PWM), especially when ultrawideband signals are considered. In this paper, a maximum likelihood estimator (MLE) of low computational complexity is implemented with a SWM for ultrawideband signals. The measurement data obtained from an ultrawideband large-scale antenna array system at 28 *to* 30 GHz *are processed with the proposed algorithm. The power azimuth-delay profiles (PADP) estimated from the SWM and the PWM are compared to those obtained from rotational horn antenna measurement, respectively. It shows that the multipath components (MPCs) are well-estimated with the proposed algorithm, and significant improvement in estimation performance is achieved with the SWM compared to the PWM. Moreover, the physical interpretation of the estimated MPCs is also given along with the estimated scatterers.*

1 Introduction

For the upcoming fifth generation (5G) communication systems or future generations, it has been predicted that key features, including massive multiple-input multiple-output (MIMO) systems and high frequency bands (above 6 GHz), will be crucial to increase the system capacity. With a large-scale antenna array system (e.g. array with tens to hundreds of elements) [1], the beamwidth of the beamforming technique can be ultra-narrow, which increases the spatial degrees of freedom of the system [2]. In addition, the high array gain is also beneficial to compensate the high propagation loss at high frequency bands. For multi-user scenarios, the system ability to serve a number of users over the same frequency and time resources through spatial multiplexing at the base station will be improved, and a higher spectral efficiency can be achieved. On the other hand, the rich spectrum resource at high frequency bands is also a key to deliver high capacity.

In order to exploit wideband large-scale antenna array systems, it is necessary to measure and characterize the underlying propagation channels. Channel measurement techniques can be generally separated into two categories, namely the time-domain sounding techniques [3–9], and the frequency-domain sounding techniques [6, 10, 11]. The time-domain sounding techniques have the advantage of fast measurement speed, which makes them suitable for measuring time-variant channels [12, 13]. However, time-domain

channel sounders are usually designed for specific measurement requirements such as measurement frequency and bandwidth. Once the sounder is implemented, it typically would need much effort to modify it for different measurement requirements. On the contrary, the frequency-domain channel sounders, which are usually vector network analyzer (VNA) based, are more flexible in this regard. Measurement frequency and bandwidth can be set to any desired value supported by the VNA systems, which makes the VNA-based sounders versatile for different frequencies. Therefore, the VNA-based sounders are quite popular among research groups for ultrawideband measurement at high frequency bands [6, 14–16]. The relatively slow measurement speed for frequency sweeping is a drawback of the VNA-based sounder, which makes it inappropriate to measure time-variant channels.

There are some new challenges for channel estimation algorithms. Two assumptions usually adopted for channel estimation are probably violated for wideband large-scale antenna array systems, namely the far-field assumption and the narrowband assumption. The far-field assumption holds when the distance between the scattering source and the antenna array is larger than the so-called near-field outer boundary, which is also known as the Fraunhofer distance. In the literature [17–20], there are several definitions for the near-field outer boundary, among which $2D^2/\lambda$ is most frequently used, where D is the array aperture in meters, and λ is the wavelength in meters [17]. Under this definition, a uniform linear array of 100 elements with half-wavelength inter-element spacing operating at 30 GHz has a near-field outer boundary of nearly 50 m, which covers the scope of many short-range application scenarios [21]. Basically, the significance of the spherical wavefront observed at the array increases as the scattering sources getting closer to the array. In order to reduce the model mismatch from the plane-wave model (PWM) for channel estimation, the spherical-wave model (SWM) can be used instead. In many standardization organizations and research groups, it is recommended to use SWMs to characterize channels for near-field cases [22–25]. Moreover, some measurement results also showed the necessity of utilizing SWM, e.g. see in [26–28].

The narrowband assumption holds when the condition $D/\lambda \ll f/B$ is satisfied, where f is the frequency and B is the bandwidth [29]. When the bandwidth becomes so wide (e.g. several GHz) that the narrowband assumption does not hold anymore for a given array aperture and frequency, the propagation delay of a single multipath component (MPC) can be resolved at different delay bins between array elements. Therefore, the array steering vector should be calculated with respect to each frequency point instead of the center frequency for channel estimation. In the literature [30], the term “ultrawideband" is usually defined as either the relative bandwidth is larger than 20 % or the absolute bandwidth is larger than 500 MHz. However, it is not directly related to the array aperture by its definition. Therefore, in this

paper, we use the term "wideband" to refer to the case where the narrowband assumption does not hold.

For the SWM, signals are assumed to be radiated from point sources. The phase difference between array elements is usually calculated based on the law of cosines according to the distance from the point sources to the array elements [26]. In the literature, the SWM has been applied to many source localization applications [18, 28, 31–34] with different estimation algorithms. Subspace based algorithms, such as the multiple signal classification algorithm (MUSIC) [35] and the estimation of signal parameters via rotational invariant techniques (ESPRIT) [36], have been adapted to estimate the locations of scatterers for narrowband scenarios in [18, 32, 37]. However, multi-dimensional estimation (e.g. joint delay-angle estimation) is hard to implement, since the computational complexity grows significantly as the size of the covariance matrix increases drastically with the number of estimation dimensions. Moreover, their estimation performance degrades severely when channel snapshots are not sufficient or coherent sources exist [29]. Maximum-likehood based algorithms, e.g. the space-alternating generalized expectation-maximization (SAGE) [38] and Richter's Maximum likelihood estimation (RiMAX) [39], have been proposed for the wideband signal with the SWM in [26, 28, 40]. Although these algorithms were not restricted by snapshot number or source correlation, the supported bandwidth is still bounded by the narrowband assumption. If the narrowband assumption does not hold due to large measurement bandwidth, the prerequisite for deploying the space-alternating mechanism would not be fulfilled [39, 41]. In [26], in order to enable the space-alternating mechanism, the wideband signal was divided into several subbands. In [28], the SAGE algorithm was implemented based on the SWM with the narrowband assumption fulfilled.

In our previous work [16], a measurement campaign was conducted with a virtual uniform circular array (UCA) with 2 GHz bandwidth at different frequencies. Using a virtual antenna array helps to reduce the mutual coupling effect between antenna elements for channel estimation [42]. The measurement data were processed with a classic (Bartlett) beamforming under the plane-wave assumption. It was shown that severe joint sidelobes exist in the power azimuth-delay profile (PADP) due to the frequency-variant array factor for huge bandwidths. To cope with the high joint sidelobes, a frequency-invariant beamformer was proposed for the UCA in [43]. However, the resulting PADP still suffers from high sidelobes for the detected dominant paths. In [27], a relaxed near-field outer boundary compared to $2D^2/\lambda$ was proposed, above which the PWM can still be used for estimating solely the angle information. In [44], a preliminary study on channel estimation based on the SWM was conducted. In order to eventually achieve a geometry-based stochastic channel model (GSCM) in connection to the 3rd generation partnership project (3GPP) [23], it is essential to obtain the multi-

dimensional MPC parameters.

The main contributions of this paper are summarized as follows:

- A low-complexity maximum likelihood estimator (MLE) is proposed for wideband large-scale array systems. The proposed estimator works for the case where the far-field and the narrowband assumption are both violated.
- MPC parameters are estimated for indoor large-scale array measurements at 28 to 30 GHz.
- Comparison is made between the SWM and the PWM with the proposed MLE algorithm in terms of the estimation performance for the measurement data.
- Physical interpretation of the estimated MPCs is given along with the locations of the estimated scatterers in the environment.

The rest of the paper is organized as follows: Section 2 gives the generic signal model for wideband large-scale antenna array systems. Section 3 discusses the limitations of the widely deployed SAGE algorithm for wideband large-scale antenna array systems. Section 4 describes the details of the proposed low-complexity MLE algorithm. Section 5 shows the estimation results for an indoor wideband large-scale array measurement, and Section 6 concludes the paper.

The notation used in this paper is as follows: Scalars are shown in regular font, and vectors and matrices are in bold font. $(\cdot)^{\mathrm{T}}$ represents the transpose operator, $(\cdot)^{\mathrm{H}}$ the complex conjugate operator, $\|\cdot\|$ the Euclidean norm, $|\cdot|$ the absolute value operator, $\langle\cdot,\cdot\rangle$ denotes the inner product, $\otimes$ denotes the Kronecker product, and $\mathrm{vec}\{\cdot\}$ denotes the vectorization operator which transforms a matrix into a column vector.

2 Signal Model for the Wideband SWM

When the SWM is considered, signals are assumed to be radiated from point sources [26]. Either a single antenna or a single scatterer can be regarded as a point source. Without loss of generality, here we assume that the transmitter (Tx) is equipped with a single antenna, and the receiver (Rx) is equipped with an M-element antenna array of an arbitrary structure (e.g. linear, circular, or rectangular). It follows that both the Tx antenna and the scatterers can be considered as the point sources in the environment, as illustrated in Fig. A.1 along with the local coordinate system at the Rx side.

For a propagation channel consisting of L paths, the channel transfer function $\mathbf{H}(\boldsymbol{f};\boldsymbol{\Theta}_l) \in \mathbb{C}^{M\times K}$ of the l-th path over K frequency points $\boldsymbol{f} =$

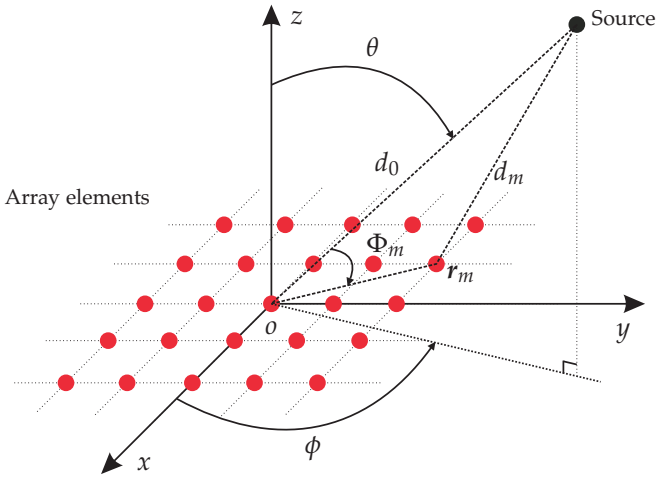

Fig. A.1: Illustration of the SWM and the local coordinate system at the Rx side.

$[f_1, f_2, \ldots, f_K]$ can be expressed as [26]

$$\mathbf{H}(\boldsymbol{f}; \boldsymbol{\Theta}_l) = \alpha_l \boldsymbol{s}(\boldsymbol{f}; \phi_l, \theta_l, d_{0,l}, \tau_l), \tag{A.1}$$

where $\boldsymbol{\Theta}_l = \{\alpha_l, \phi_l, \theta_l, d_{0,l}, \tau_l\}$ is the parameter set of the l-th path, including the complex amplitude α_l, the azimuth angle of direction of arrival ϕ_l, the elevation angle of direction of arrival θ_l, the distance $d_{0,l}$ from the source to the array center, and the delay τ_l from the Tx antenna to the Rx array center. The (m,k)-th component of $\boldsymbol{s}(\boldsymbol{f}; \phi_l, \theta_l, d_{0,l}, \tau_l) \in \mathbb{C}^{M \times K}$ can be written as

$$\begin{aligned} s_m(f_k; \phi_l, \theta_l, d_{0,l}, \tau_l) = \frac{g_m(f_k; \phi_l, \theta_l)}{4\pi f_k d_{m,l}/c} \cdot \exp\{-j2\pi f_k \tau_l\} \\ \cdot \exp\{-j2\pi f_k (d_{m,l} - d_{0,l})/c\}, \end{aligned} \tag{A.2}$$

where $g_m(\cdot)$ is the antenna field pattern, c is the speed of light, and $d_{m,l}$ denotes the distance from the source to the m-th array element for the l-th path. Note when the source corresponds to the Tx instead of a scatterer, it leads to $\tau_l = d_{0,l}/c$. Given the coordinates $\boldsymbol{r}_m$ of the m-th array element with respect to the array center, the distance $d_{m,l}$ can be determined by applying the law of cosines as

$$d_{m,l} = \sqrt{d_{0,l}^2 + \|\boldsymbol{r}_m\|^2 - 2 d_{0,l} \|\boldsymbol{r}_m\| \cos \Phi_{m,l}}, \tag{A.3}$$

where $\Phi_{m,l}$ denotes the angle between vector $\boldsymbol{r}_m$ and the direction of arrival of the l-th wave. For notation simplicity, we use $\boldsymbol{\Theta}_l^{\bar{\alpha}} = \{\phi_l, \theta_l, d_{0,l}, \tau_l\}$ to denote the parameter set without α_l, and $\boldsymbol{s}(\boldsymbol{f}; \boldsymbol{\Theta}_l^{\bar{\alpha}})$ to represent $\boldsymbol{s}(\boldsymbol{f}; \phi_l, \theta_l, d_{0,l}, \tau_l)$ hereafter.

The measured channel frequency response $\mathbf{Y}(f) \in \mathbb{C}^{M\times K}$ at the output of the Rx array can then be expressed as

$$\mathbf{Y}(f) = \sum_{l=1}^{L} \mathbf{H}(f;\boldsymbol{\Theta}_l) + \boldsymbol{n}(f), \tag{A.4}$$

where $\boldsymbol{n}(f) \in \mathbb{C}^{M\times K}$ is the noise of the measurement system, and its entries are assumed to follow the independent and identically distributed (i.i.d.) complex white Gaussian distribution with zero mean and variance σ_n^2 [26]. To keep a compact notation, we further define

$$\mathbf{H}(f;\boldsymbol{\Theta}) = \sum_{l=1}^{L} \mathbf{H}(f;\boldsymbol{\Theta}_l), \tag{A.5}$$

with $\boldsymbol{\Theta} = \{\boldsymbol{\Theta}_1, \boldsymbol{\Theta}_2, \ldots, \boldsymbol{\Theta}_L\}$.

3 Limitations of the SAGE Algorithm for Wideband Large-scale Antenna Array Systems

For channels measured with conventional narrowband small-scale array systems, under the narrowband and the far-field assumptions, the channel transfer function $\mathbf{H}(f;\boldsymbol{\Theta}_l)$ in (A.1) can be simplified as [38]

$$\mathbf{H}(f;\tilde{\boldsymbol{\Theta}}_l) = \alpha_l \boldsymbol{v}(\phi_l,\theta_l) \otimes \boldsymbol{\zeta}(f;\tau_l) \tag{A.6}$$

where $\tilde{\boldsymbol{\Theta}}_l = \{\alpha_l, \phi_l, \theta_l, \tau_l\}$ denotes the parameter set with $d_{0,l}$ left out. $\boldsymbol{v}(\phi_l,\theta_l) \in \mathbb{C}^{M\times 1}$ is the array steering vector with the m-th entry written as

$$v_m(\phi_l,\theta_l) = g_m(f_c;\phi_l,\theta_l) \cdot \exp\{j2\pi f_c \langle \boldsymbol{e}(\phi_l,\theta_l), \boldsymbol{r}_m\rangle\}, \tag{A.7}$$

where f_c is the center frequency, $\boldsymbol{e}(\cdot)$ is the unit direction vector. $\boldsymbol{\zeta}(f;\tau_l) \in \mathbb{C}^{1\times K}$ is the frequency response corresponding to the delay τ_l, with its k-th entry written as $\zeta(f_k;\tau_l) = \exp\{-j2\pi f_k \tau_l\}$.

The SAGE algorithm [38] is often used to estimate the parameters of MPCs. Its main advantage over conventional expectation-maximization (EM) algorithms is that a multi-dimensional search is replaced with several one-dimensional searches. Therefore, the computational complexity is significantly decreased, while the estimator still converges to the global maximum of its likelihood function with a sufficient number of iterations. A prerequisite to utilize the space-alternating mechanism is that the likelihood function needs to be independent between different parameter spaces [41]. This likelihood independency between direction $\boldsymbol{e}(\phi_l,\theta_l)$ and delay τ_l is guaranteed

from the Kronecker structure of $\mathbf{H}(f;\tilde{\boldsymbol{\Theta}}_l)$ [39], as shown in (A.6). As a result, a sequentially parameter updating procedure, i.e. the space-alternating mechanism, can be deployed as in [38].

However, as discussed in the introduction, with the narrowband assumption violated, the Kronecker structure in (A.6) cannot be maintained due to the frequency dependency of $\boldsymbol{v}(\phi_l,\theta_l)$. Thus, the likelihood independency between $\boldsymbol{e}(\phi_l,\theta_l)$ and τ_l does not hold. Moreover, with the far-field assumption violated, an additional parameter, i.e. source distance $d_{0,l}$, is introduced in the signal model. Consequently, the sequentially parameter updating procedure cannot be applied between $\boldsymbol{e}(\phi_l,\theta_l)$, $d_{0,l}$ and τ_l for channels measured with wideband large-scale array systems. In other words, estimation needs to be done jointly among parameters in order to prevent the estimator from converging to a local maxima of the likelihood function. Fig. A.2 gives the sketch of the feasibility region of the SAGE algorithm and the proposed algorithm with respect to array aperture and signal bandwidth.

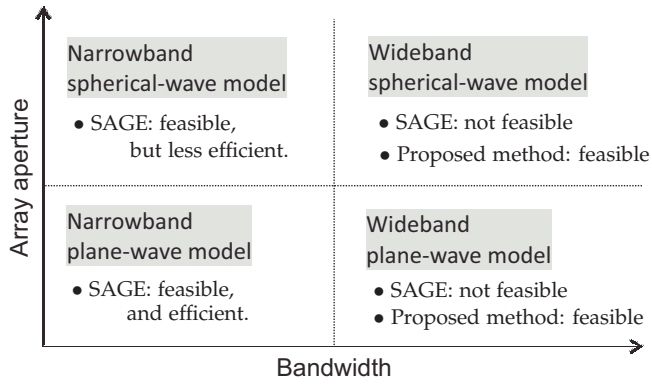

Fig. A.2: Feasibility region of the SAGE and the proposed MLE algorithm.

4 A Low-complexity Maximum Likelihood Estimator

Given the observation $\mathbf{Y}(f)$ at the output of the Rx array, the expectation of the log-likelihood function of the parameters $\boldsymbol{\Theta}$ can be written as [29]

$$\mathbb{E}\{\Lambda(\boldsymbol{\Theta};\mathbf{Y}(f))\} = -\ln(\pi\sigma_n^2) - \frac{1}{\sigma_n^2 MK}\left\|\mathrm{vec}\{\mathbf{Y}(f)\} - \mathrm{vec}\{\mathbf{H}(f;\boldsymbol{\Theta})\}\right\|^2, \tag{A.8}$$

where $\mathbb{E}\{\cdot\}$ denotes expectation, and is calculated as the sample mean. The estimate of $\boldsymbol{\Theta}$ is obtained by maximizing (A.8) over the span of parameters,

$$\hat{\boldsymbol{\Theta}} = \arg\max_{\boldsymbol{\Theta}} \left\{ \mathbb{E}\{\Lambda(\boldsymbol{\Theta}; \mathbf{Y}(f))\} \right\}. \tag{A.9}$$

A brute-force search for (A.9) is computationally prohibitive due to the high dimension of $\boldsymbol{\Theta}$ [38]. Given two paths, l and l', if any of the differences $|\phi_l - \phi_{l'}|$, $|\theta_l - \theta_{l'}|$, $|d_{0,l} - d_{0,l'}|$, and $|\tau_l - \tau_{l'}|$ is larger than the resolution in its respective domain, the inner product of $\mathrm{vec}\{\boldsymbol{s}(f; \boldsymbol{\Theta}_l^{\bar{\alpha}})\}$ and $\mathrm{vec}\{\boldsymbol{s}(f; \boldsymbol{\Theta}_{l'}^{\bar{\alpha}})\}$ approaches zero due to the orthogonality of their vector spaces [27, 38]. Therefore, $\hat{\boldsymbol{\Theta}}$ in (A.9) can be approximated alternatively through matched filtering [2, 38]. However, due to the large power difference between the strong MPCs and the weak MPCs, the mainlobes of the estimated power spectra of the weak MPCs may be buried under the sidelobes of the estimated power spectra of the strong MPCs, which causes interference to the estimation of the weak MPCs. To cope with that, the estimate $\hat{\boldsymbol{\Theta}}_l$ for individual paths can be obtained sequentially in a successive interference cancellation (SIC) manner as described below.

4.1 Procedure of an MLE Algorithm with SIC

The estimate $\hat{\boldsymbol{\Theta}}_l$ for individual paths can be obtained sequentially through the matched filtering with SIC as

$$\hat{\boldsymbol{\Theta}}_l^{\bar{\alpha}} = \arg\max_{\boldsymbol{\Theta}_l^{\bar{\alpha}}} \|z(\boldsymbol{\Theta}_l^{\bar{\alpha}})\|, \tag{A.10}$$

$$\hat{\alpha}_l = \frac{z(\hat{\boldsymbol{\Theta}}_l^{\bar{\alpha}})}{\|\mathrm{vec}\{\boldsymbol{s}(f; \hat{\boldsymbol{\Theta}}_l^{\bar{\alpha}})\}\|}, \tag{A.11}$$

where

$$z(\boldsymbol{\Theta}_l^{\bar{\alpha}}) = \frac{\mathrm{vec}\left\{\boldsymbol{s}(f; \boldsymbol{\Theta}_l^{\bar{\alpha}})\right\}^{\mathrm{H}} \mathrm{vec}\{\mathbf{Y}^{(l)}(f)\}}{\|\mathrm{vec}\{\boldsymbol{s}(f; \boldsymbol{\Theta}_l^{\bar{\alpha}})\}\|}, \tag{A.12}$$

and

$$\mathbf{Y}^{(l)}(f) = \begin{cases} \mathbf{Y}(f) & \text{if } l = 1. \\ \mathbf{Y}(f) - \sum_{l'=1}^{l-1} \mathbf{H}(f; \hat{\boldsymbol{\Theta}}_{l'}) & \text{if } l > 1. \end{cases} \tag{A.13}$$

When the first path (i.e. $l = 1$) is estimated, the parameters are obtained with the original observation $\mathbf{Y}(f)$. The transfer function given in (A.1) is then reconstructed with respect to $\hat{\boldsymbol{\Theta}}_1$, and subtracted from the original observation $\mathbf{Y}(f)$. The remaining observation is then used for estimating the next path. This procedure is repeated until we have extracted a preset number of paths L, which is usually determined empirically.

4.2 A Coarse-to-Fine Search

The MLE is well-known for its high computational complexity due to its joint estimation mechanism, especially when the parameter dimension is large. The computational complexity comes from both the high-dimensional joint estimation and the large matrix size (i.e. $\mathbf{Y}(\boldsymbol{f}) \in \mathbb{C}^{M\times K}$) as well. In order to reduce the complexity, we separate the estimation for $\hat{\boldsymbol{\Theta}}_l$ into two stages, namely the initialization stage and the refinement stage.

4.2.1 The Initialization Stage

The frequency point with the highest signal power over M elements is selected as [32]

$$f_k^{max} = \arg\max_{f_k} \left\| \mathbf{Y}^{(l)}(f_k) \right\|^2, \tag{A.14}$$

where $\mathbf{Y}^{(l)}(f_k) \in \mathbb{C}^{M\times 1}$ is the k-th column vector of $\mathbf{Y}^{(l)}(\boldsymbol{f})$. The initial estimates of $\boldsymbol{\Theta}_l^{\bar{\alpha},\bar{\tau}} = \{\phi_l, \theta_l, d_{0,l}\}$ are obtained through the matched filtering as

$$(\hat{\boldsymbol{\Theta}}_l^{\bar{\alpha},\bar{\tau}})^{init} = \arg\max_{\boldsymbol{\Theta}_l^{\bar{\alpha},\bar{\tau}}} \left\| \underline{z}(f_k^{max}; \boldsymbol{\Theta}_l^{\bar{\alpha},\bar{\tau}}) \right\|, \tag{A.15}$$

where

$$\underline{z}(f_k; \boldsymbol{\Theta}_l^{\bar{\alpha},\bar{\tau}}) = \frac{\underline{\boldsymbol{s}}(f_k; \boldsymbol{\Theta}_l^{\bar{\alpha},\bar{\tau}})^{\mathrm{H}} \mathbf{Y}^{(l)}(f_k)}{\|\underline{\boldsymbol{s}}(f_k; \boldsymbol{\Theta}_l^{\bar{\alpha},\bar{\tau}})\|}, \tag{A.16}$$

and the m-th entry of $\underline{\boldsymbol{s}}(f_k; \boldsymbol{\Theta}_l^{\bar{\alpha},\bar{\tau}}) \in \mathbb{C}^{M\times 1}$ is

$$\underline{s}_m(f_k; \boldsymbol{\Theta}_l^{\bar{\alpha},\bar{\tau}}) = \frac{g_m(f_k; \phi_l, \theta_l)}{4\pi f_k d_{m,l}/c} \cdot \exp\{-j2\pi f_k (d_{m,l} - d_{0,l})/c\}. \tag{A.17}$$

The initial estimate of τ_l is then estimated following the same principle as

$$\hat{\tau}_l^{init} = \arg\max_{\tau_l} \frac{1}{\sqrt{K}} \left\| \sum_{k=1}^{K} \underline{z}\left(f_k; (\hat{\boldsymbol{\Theta}}_l^{\bar{\alpha},\bar{\tau}})^{init}\right) \exp\{j2\pi f_k \tau_l\} \right\|. \tag{A.18}$$

The initial estimates of $\boldsymbol{\Theta}_l^{\bar{\alpha}}$ are obtained as $(\hat{\boldsymbol{\Theta}}_l^{\bar{\alpha}})^{init} = \{\hat{\phi}_l^{init}, \hat{\theta}_l^{init}, \hat{d}_{0,l}^{init}, \hat{\tau}_l^{init}\}$.

4.2.2 The Refinement Stage

The search candidates are refined in the vicinity of the initial estimates $(\hat{\boldsymbol{\Theta}}_l^{\bar{\alpha}})^{init}$ obtained from the initialization stage. The MLE algorithm described in (A.10) to (A.13) is then conducted with the full observation matrix $\mathbf{Y}^{(l)}(\boldsymbol{f})$ over the confined region of the channel parameters to obtain the final estimates $\hat{\boldsymbol{\Theta}}_l$.

In the initialization stage, the matrix size decreases from $M \times K$ to $M \times 1$ and $1 \times K$ in (A.15) and (A.18), respectively. In the refinement stage, the

number of search candidates is further decreased due to the confined region around the initial estimates. Therefore, the overall computational complexity decreases significantly.

4.3 Decision of Number of Paths $\hat{L}$

The number of paths $\hat{L}$ varies a lot with respect to different estimation algorithms. Usually, the maximum-likelihood based algorithms return more paths than the subspace-based algorithms. One of the reasons for this is that the MLE-based algorithms often assume specular propagation, so the diffuse scattering part of the channel would also be treated as specular paths, which could increase the number of paths drastically. Another reason is that when the deployed signal model does not match the measurement data, either due to a poor system calibration before measurement, or an invalid assumption (e.g. the narrowband or the far-field assumption) for a specific scenario, artificial paths would also be created during estimation. To alleviate over-estimation, the Akaike information criterion (AIC) [45–47] is used to determine the appropriate number of paths, and it can be expressed as

$$\mathrm{AIC}(L) = -2\Lambda(\hat{\Theta}) + \gamma L. \tag{A.19}$$

The first term stands for the likelihood as in (A.8), and the second term represents the penalty for overfitting. The factor γ can be adjusted to define different significance levels of the penalty [48]. By substituting (A.8) in (A.19), we obtain the AIC expression as

$$\mathrm{AIC}(L) = 2\ln\left(\pi\sigma_n^2\right) + \gamma L + \frac{2}{\sigma_n^2 MK}\left\|\mathrm{vec}\{\mathbf{Y}(\boldsymbol{f})\} - \mathrm{vec}\left\{\sum_{l=1}^{L}\mathbf{H}(\boldsymbol{f};\hat{\boldsymbol{\Theta}}_l)\right\}\right\|^2. \tag{A.20}$$

The appropriate number of paths is determined by $\hat{L} = \arg\min_L \mathrm{AIC}(L)$. Note the indices of the estimated paths need to be permuted according to the likelihood of each path calculated in (A.12) in descending order.

To have a more intuitive understanding for the decision $\hat{L}$ from (A.20), we calculate the first-order difference of $\mathrm{AIC}(L)$ as

$$\Delta\mathrm{AIC}(L) = \mathrm{AIC}(L) - \mathrm{AIC}(L-1), \tag{A.21}$$

where Δ denotes the difference operator. Inserting (A.20) into (A.21) yields

$$\begin{aligned}\Delta\mathrm{AIC}(L) = {} & \frac{2}{\sigma_n^2 MK}\left\|\mathrm{vec}\{\mathbf{Y}(\boldsymbol{f})\} - \mathrm{vec}\left\{\sum_{l=1}^{L}\mathbf{H}(\boldsymbol{f};\hat{\boldsymbol{\Theta}}_l)\right\}\right\|^2 \\ & - \frac{2}{\sigma_n^2 MK}\left\|\mathrm{vec}\{\mathbf{Y}(\boldsymbol{f})\} - \mathrm{vec}\left\{\sum_{l'=1}^{L-1}\mathbf{H}(\boldsymbol{f};\hat{\boldsymbol{\Theta}}_{l'})\right\}\right\|^2 + \gamma.\end{aligned} \tag{A.22}$$

When the MPCs are well-separated in the parameter domain, $\text{vec}\left\{\mathbf{H}(f;\hat{\boldsymbol{\Theta}}_l)\right\}$ is roughly orthogonal to $\text{vec}\left\{\mathbf{H}(f;\hat{\boldsymbol{\Theta}}_{l'})\right\}$ given $l \neq l'$. By applying the Pythagorean theorem, (A.22) can be approximated as

$$\Delta\text{AIC}(L) = -\frac{2}{\sigma_n^2 MK}\left\|\text{vec}\left\{\mathbf{H}(f;\hat{\boldsymbol{\Theta}}_L)\right\}\right\|^2 + \gamma. \tag{A.23}$$

Since the indices of the estimated paths are permuted in descending order of the likelihood, the term $\left\|\text{vec}\left\{\mathbf{H}(f;\hat{\boldsymbol{\Theta}}_L)\right\}\right\|^2$, which can be interpreted as the power of the L-th path, decreases monotonically with L. In other words, the first-order difference of $\text{AIC}(L)$ increases monotonically with L, and hence the second-order difference of $\text{AIC}(L)$ is non-negative. Therefore, $\text{AIC}(L)$ is convex, and its minimum can be achieved when $\Delta\text{AIC}(L) = 0$ [49]. Setting (A.23) to zero leads to

$$\frac{1}{\sigma_n^2 MK}\left\|\text{vec}\left\{\mathbf{H}(f;\hat{\boldsymbol{\Theta}}_L)\right\}\right\|^2 = \frac{\gamma}{2}, \tag{A.24}$$

which indicates this criterion can be interpreted as a threshold in power-to-noise ratio averaged by MK. The estimated paths with power-to-noise ratio above $\gamma/2$ will be considered as dominant and kept. $\gamma = 2$ was assumed to be sufficient in significance in [45]. When $\gamma = 2$ is used, it corresponds to a power-to-noise ratio of 0 dB. In the following sections, $\gamma = 2$ was also used for data processing. The whole procedure of the proposed MLE algorithm is summarized in Algorithm 1.

Algorithm 1 Procedure of the proposed MLE algorithm with SIC.

Input: $\mathbf{Y}(f), L$
  for $l = 1$ **to** L **do**
    Initialization:
    • $(\hat{\boldsymbol{\Theta}}_l^{\bar{\alpha}})^{init} = \{\hat{\phi}_l^{init}, \hat{\theta}_l^{init}, \hat{d}_{0,l}^{init}, \hat{\tau}_l^{init}\}$.
    • Define search candidates with respect to $(\hat{\boldsymbol{\Theta}}_l^{\bar{\alpha}})^{init}$.
    Refinement:
    • $\hat{\boldsymbol{\Theta}}_l = \{\hat{\alpha}_l, \hat{\phi}_l, \hat{\theta}_l, \hat{d}_{0,l}, \hat{\tau}_l\}$.
    SIC:
    • $\mathbf{Y}^{(l)}(f)$.
  end for
  • Rearrange path indices with respect to likelihood in descending order.
  • Determine $\hat{L}$ with AIC.
Output: $\hat{\boldsymbol{\Theta}} = \{\hat{\boldsymbol{\Theta}}_1, \hat{\boldsymbol{\Theta}}_2, \ldots, \hat{\boldsymbol{\Theta}}_{\hat{L}}\}$.

5 Channel Measurement and Estimation

5.1 Indoor LoS and OLoS Scenarios

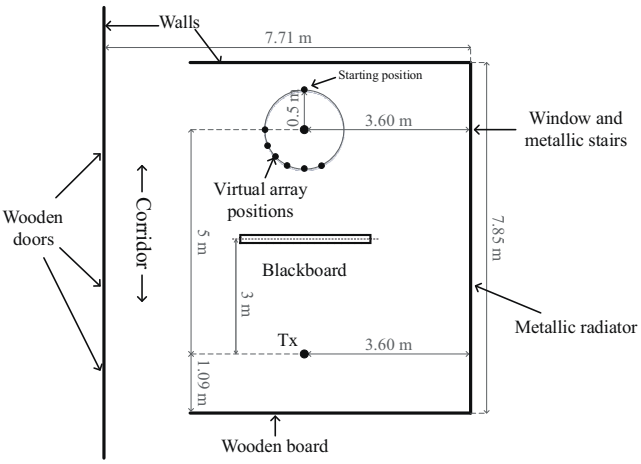

(a)

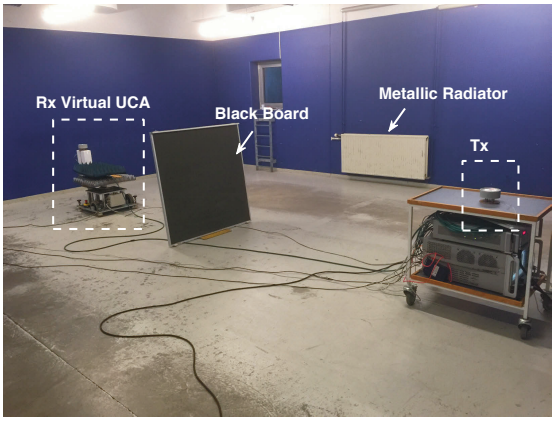

(b)

Fig. A.3: (a) Dimensions and (b) photo of the measurement environment.

The measurements were conducted in a basement. A sketch of the measurement area is shown in Fig. A.3(a). Two sets of antenna configurations were used in the measurements, namely "Config. 1" and "Config. 2". For "Config. 1", both the Tx and the Rx were equipped with biconical antennas. For "Config. 2", the Rx antenna was replaced with a horn antenna. The antenna specifications are summarized in Table A.1.

Table A.1: Antenna Specifications and Measurement Settings.

Antenna specifications		
	Horn	Biconical
Operating frequency	26.4 to 40.1 GHz	2 to 30 GHz
Half-power beamwidth[a]	20°	Omnidirectional
Gain[b]	19 dB	6 dB
Polarization	Vertical	Vertical
Measurement settings		
	Config. 1	Config. 2
Tx antenna	Biconical	Biconical
Rx antenna	Biconical	Horn
Rx rotation radius	0.5 m	0 m
Azimuth rotation span	0° to 360° with 720 steps	
Frequency sweep range	28 to 30 GHz with 750 points	

[a]Evaluated in the azimuth plane at 28 to 30 GHz.
[b]Evaluated at 28 to 30 GHz.

During the measurement, both the Tx and the Rx antenna were placed 0.84 m above the floor. The Rx antenna was mounted on a turntable. A virtual UCA of 720 elements, i.e. $M = 720$, with radius 0.5 m was formed on the Rx side. The frequency response was measured with a VNA from 28 to 30 GHz with 750 frequency points, i.e. $K = 750$, at each element position. The corresponding delay range is $[0, 374.5]$ ns. The inter-element spacing of the UCA is 4.4 mm, which is smaller than half the wavelength at 30 GHz (i.e. 5 mm). Therefore, spatial aliasing is avoided [50]. The Fraunhofer distance at 30 GHz is 200 m, whereas the distance between the Tx and the center of the Rx array is only 5 m (see Fig. A.3(a)). Thus, the far-field assumption is not met in our measurement. The narrowband assumption does not hold either since the array aperture (i.e. 1 m) is much larger than the delay resolution multiplied by the speed of light (i.e. 0.15 m). The measurement settings are summarized in Table A.1.

Note that in "Config. 2", when the horn antenna was deployed at the Rx, the feed of the horn was positioned at the rotation center of the turntable. Therefore, the rotation radius is denoted as 0 m in Table A.1. Also note that to cope with the influence of the cable effect in the measurement setup, the RF cable was fixed to a wooden board to minimize the cable movement.

For each set of antenna configurations, two scenarios were considered, i.e. the line-of-sight (LoS) and the obstructed line-of-sight (OLoS) scenario. The OLoS scenario was created by placing an additional blackboard with a metallic substrate of dimensions 1.19 m $\times$ 1.19 m between the Tx and the Rx

to block the LoS path. When measuring the LoS scenario, the blackboard was removed from the environment. A photo of the measurement environment is shown in Fig. A.3(b). Readers are referred to [16] for a full description of the measurement campaign.

The rotational horn antenna measurement was conducted to obtain a reference PADP of the channel. The estimated PADP from the UCA measurement are compared to the reference PADP to assess the performance of the proposed algorithm in the next subsection.

5.2 MPC Parameter Estimation and Comparison between the SWM and the PWM

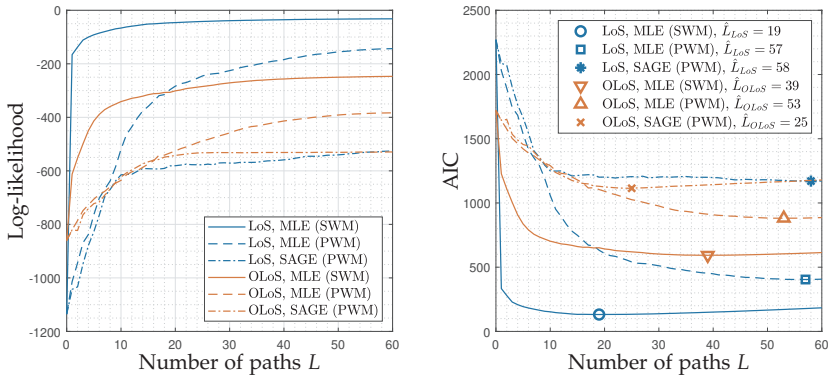

Fig. A.4: The log-likelihood (left) and the AIC (right) with respect to the number of paths for the LoS and the OLoS scenario. Results from the SAGE algorithm based on the PWM with 10 EM iterations are also presented for comparison.

According to the data sheet of the biconical antenna [51], the variation of the antenna gain in the measurement frequency range is up to 1.5 dB, so we assume frequency independent antenna response for the estimation. The measurement data were processed with the proposed algorithm based on the SWM and the PWM, respectively. Initially, 60 paths were assigned to the estimator for both the LoS and the OLoS scenario. Fig. A.4 shows the likelihood function and the AIC with respect to the number of paths for both scenarios. It can be clearly seen that the likelihood obtained with the SWM is always higher than that obtained with the PWM for both scenarios. Also, the AIC of the SWM is always lower than that of the PWM. Therefore, it can be concluded that the SWM is superior to the PWM for the large-scale antenna array systems in the estimation.

Moreover, the likelihood for the SWM increases significantly with the number of paths at first. After a certain point, it tends to converge for both scenarios, which means the additional benefits of using a larger number of

paths are insignificant. The number of paths is selected at the minimum AIC, which corresponds to $\hat{L}_{\mathrm{LoS}} = 19$ and $\hat{L}_{\mathrm{OLoS}} = 39$ for the LoS and the OLoS scenario, respectively. The number of paths for the PWM is $\hat{L}_{\mathrm{LoS}} = 57$ and $\hat{L}_{\mathrm{OLoS}} = 53$. By comparison, both a higher likelihood and a less number of paths are obtained with the SWM, which shows the advantages of the SWM for large-scale array systems. The results obtained from the SAGE algorithm based on the PWM with 10 EM iterations are also given in Fig. A.4, which shows it does not work well for wideband signals. Estimation with the SAGE algorithm assuming the SWM were not carried out due to its high computation time caused by the joint estimation together with multiple iterations of calculation.

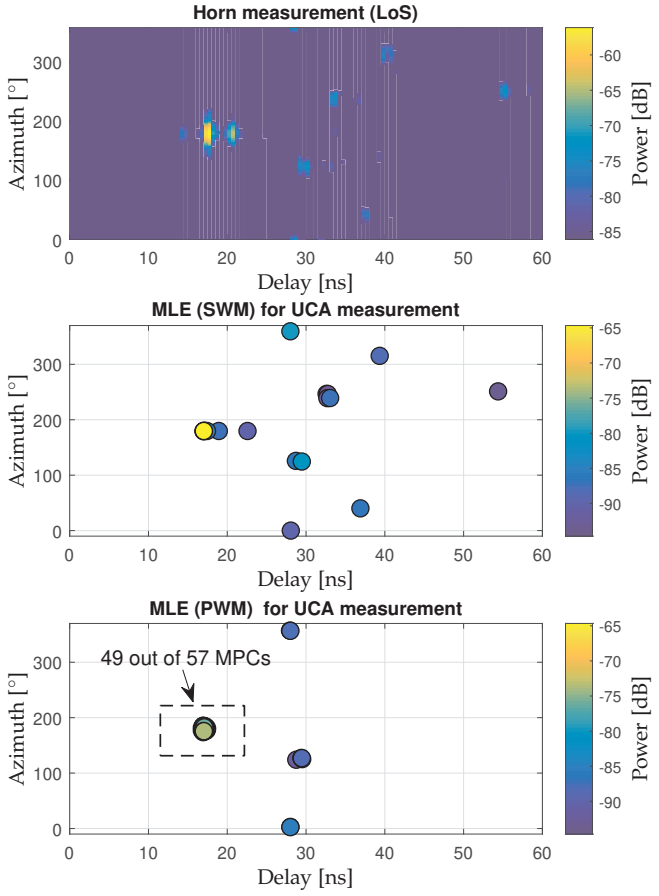

Fig. A.5: The reference PADP obtained from the horn measurement (top) and the estimated MPCs for the LoS scenario. 19 paths are shown for the SWM (middle), and 57 paths for the PWM (bottom) according to the number of paths set by the AIC criterion as shown in Fig. A.4.

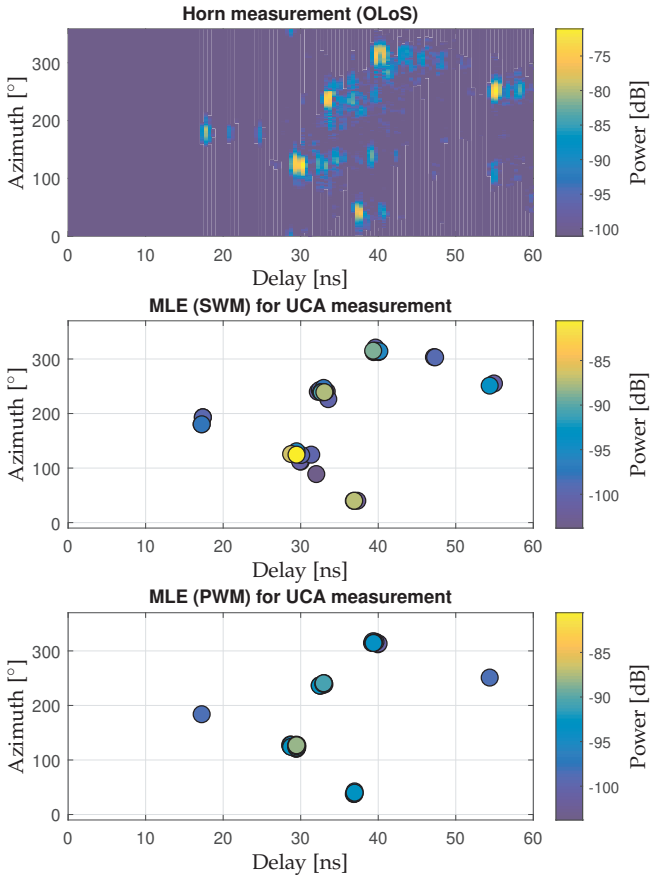

Fig. A.6: The reference PADP obtained from the horn measurement (top) and the estimated MPCs for the OLoS scenario. 39 paths are shown for the SWM (middle), and 53 paths for the PWM (bottom) according to the number of paths set by the AIC criterion as shown in Fig. A.4.

Fig. A.5 and Fig. A.6 show the estimated PADP in comparison to that measured with the horn antenna for the LoS and the OLoS scenario, respectively. For the LoS scenario in Fig. A.5, it can be observed that the resulting PADP from the SWM matches that from the horn measurement very well, whereas using the PWM leads to poor extraction of the weak paths even with a larger number of paths. Moreover, most of the MPCs (i.e. 49 out of 57) estimated with the PWM concentrate in the region around the LoS component, which shows a severe model mismatch between the PWM and the measurement. This is due to the fact that the power of the LoS component is dominant, and it would be estimated first by the estimator. However, if the transfer function reconstructed form the signal model is not accurate enough to cancel its contribution in the observation $\mathbf{Y}(f)$, artificial paths would be

recursively created and estimated around the LoS component due to the incomplete cancellation. In addition, there is an obvious difference in power between the dominant MPCs estimated from the SWM and the PWM. For example, the power of the LoS component for the SWM case is around 10 dB higher than that for the PWM case. The power loss from the PWM was also reported in [26, 27], which is considered as a result of the model mismatch in near-field estimation problems.

For the OLoS scenario in Fig. A.6, the PADP from the PWM is more similar to that from the SWM compared to the LoS scenario. This is due to the fact that the power of the MPCs is more evenly distributed for the OLoS scenario. However, model mismatch can still be observed from the difference in power between the MPCs estimated with the PWM and those with the SWM. According to the observations from Figs. A.4 to A.6, it can be concluded that the SWM outperforms the PWM for near-field estimation problems. It is worth mentioning that a clustering procedure [52] can be applied to the estimated MPCs for cluster based channel models [23].

5.3 Power Delay Profile and Power Extraction Rate

The power delay profile (PDP) for each element of the array is calculated as the inverse discrete Fourier transform (IDFT) of the reconstructed channel frequency response using the SWM for the LoS and the OLoS scenario, as shown in Fig. A.7 and Fig. A.8, respectively. A good match between them can be clearly seen. The power extraction rate $\hat{P}$ is further calculated as

$$\hat{P} = 1 - \frac{\left\| \mathrm{vec}\left\{ \mathbf{H}(f; \hat{\boldsymbol{\Theta}}) - \mathbf{Y}(f) \right\} \right\|^2}{\left\| \mathrm{vec}\left\{ \mathbf{Y}(f) \right\} \right\|^2}. \tag{A.25}$$

$\hat{P}_{\mathrm{LoS}} = 95\%$ and $\hat{P}_{\mathrm{OLoS}} = 69\%$ are obtained for the SWM case for the LoS and the OLoS scenario, respectively. In comparison, a lower power extraction rate of $\hat{P}_{\mathrm{LoS}} = 86\%$ and $\hat{P}_{\mathrm{OLoS}} = 54\%$ are obtained for the PWM case. For the LoS scenario, the LoS component is the main contribution of the total power, hence the high extraction rate. For the OLoS scenario, the proportion of the power in the diffuse scattering components becomes more significant as seen in the background in Fig. A.8, and a lower extraction rate is expected.

5.4 Channel Characteristics Obtained from Estimated MPCs

Channel characteristics including azimuth spread of arrival (ASA), elevation spread of arrival (ESA), and delay spread (DS), are calculated the same way as in [23], and are listed in Table A.2. Huge differences can be seen between the parameter spreads obtained from the proposed MLE algorithm with the PWM and the SWM. For example, the DS and the ASA from the

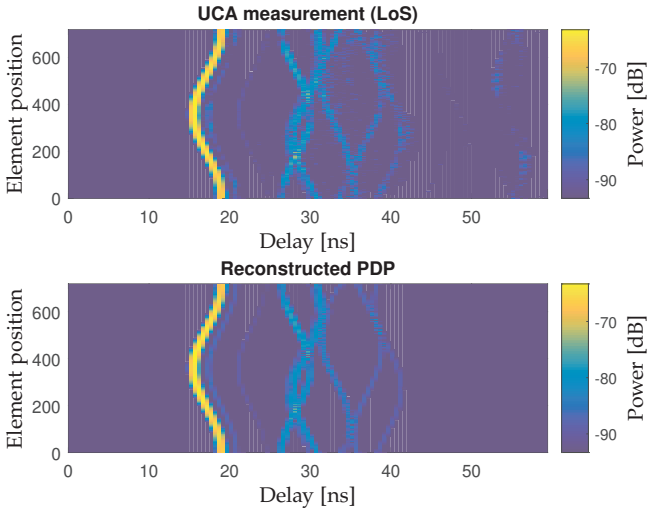

Fig. A.7: The PDP of all elements from measurement (top), and the reconstructed channel (bottom) with the SWM for the LoS scenario with 30 dB power range.

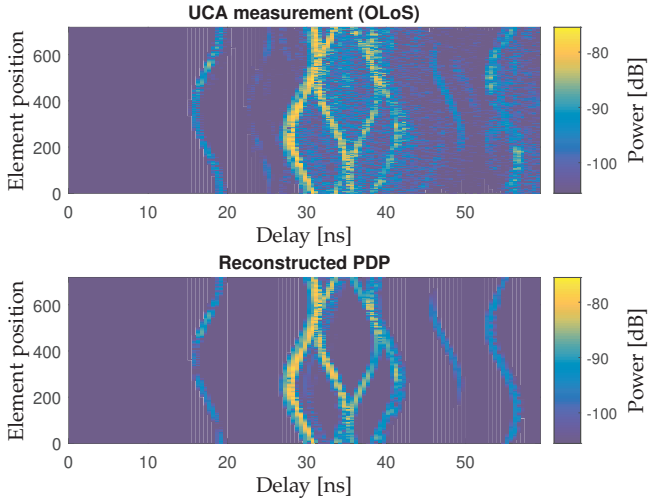

Fig. A.8: The PDP of all elements from measurement (top), and the reconstructed channel (bottom) with the SWM for the OLoS scenario with 30 dB power range.

SWM results are much larger than those from the PWM results, whereas the ESA for the LoS scenario from the SWM results is only around one-fourth of that from the PWM results. This is because the estimator implemented with the SWM captured more weak MPCs, which are widely spread in the azimuth and delay domain. In contrast, the estimator implemented with the PWM returned many artificial paths around the dominant paths due to the

model mismatch, which causes spread in the elevation domain. The comparison shows the model mismatch can severely affect the estimated channel characteristics. The corresponding values given in 3GPP TR 38.901 for the indoor-office scenario are also presented. Basically, the values from TR 38.901 are several times larger than those from the SWM, except the ASA for the non-line-of-sight (NLoS) scenarios. Since the parameter values from our measurement are obtained in a specific environment, they are not necessarily very representative. However, it has been extensively discussed in recent meetings, e.g. IRACON [53], that the parameter values in the current release of 3GPP model for high frequency bands may also be changed in future due to the lack of input from measurement data.

Table A.2: Channel characteristics obtained from MLE (PWM), MLE (SWM), and 3GPP for indoor scenarios at 28 to 30 GHz.

Characteristics	MLE (PWM)		MLE (SWM)		3GPP[a]	
	LoS	OLoS	LoS	OLoS	LoS	NLoS
DS [ns]	2.14	4.24	3.82	5.55	19.64	25.90
ASA [°]	18.58	74.01	24.96	81.15	31.65	50.18
ESA [°]	4.64	3.76	0.92	2.20	11.37	14.64

[a]The values are evaluated at 29 GHz with respect to the indoor-office scenarios in 3GPP TR 38.901 [23]. NLoS denotes non-LoS scenarios.

5.5 Physical Interpretation of the Estimated MPCs

In order to have a physical interpretation of the propagation mechanism, the estimated propagation paths are usually traced back in the physical environment [54–56]. A simple ray tracer is used here [44]. For a LoS path or a one-bounce path, a unique path can be drawn in physical environment through simple geometry with the delay and the direction of arrival information. For multi-bounce paths, since we only have the path parameters estimated from the Rx side, it is unknown if they are induced from either reflection or diffraction, or a combination of both. Here we assume only specular reflection for high-order bounces (i.e. second-order and above). The estimated paths are traced in the environment for both the LoS and the OLoS scenario as shown in Fig. A.9. Moreover, it is interesting to see if the estimated locations of the scatterers can match any physical object in the environment. Thus, the locations of scatterers are also plotted as solid circles in Fig. A.9. The location of the scatterer associated with the l-th path is calculated as the point from where the distance to the Rx array center along the path trajectory is equal to $\hat{d}_{0,l}$. The color shows the power of each path.

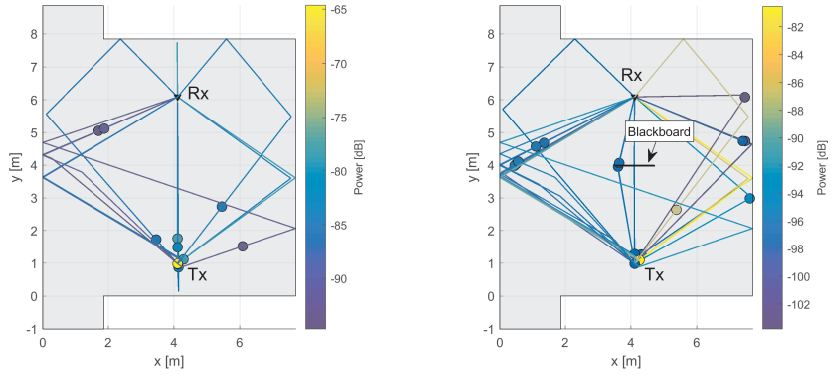

(a) LoS scenario (b) OLoS scenario

Fig. A.9: The propagation paths trajectories in the physical environment for the LoS and the OLoS scenario. Scattering sources are plotted along the path trajectories in solid circles. The color shows the power in dB.

Fig. A.9(a) shows the path trajectories for the LoS scenario. Due to the metallic radiator (heater) on the right wall, it can be seen the power reflected from the right wall is higher than that from the left wall. From the estimated scatterer locations, it can be observed that some of them are traced back to the the Tx location, whereas the others are a bit off the physical objects, which can be induced from the insufficient modelling of the environment. In addition, since the estimation for the distance d_0 relies on the curvature of the spherical wavefront impinging upon the array, the estimation for a farther scattering source would be less accurate.

Fig. A.9(b) shows the path trajectories for the OLoS scenario. It can be observed that the power of the LoS component is significantly attenuated by the blackboard. Besides the reflection from the walls, the diffraction from the edges of the blackboard can be seen as well. Most of the estimated scatterer locations are either close to the walls, the edges of the blackboard, or the Tx. The good match between the estimated scatterer locations and the physical objects helps to reveal the propagation mechanisms like reflection and diffraction. Nonetheless, it is worth noting that when the surfaces of the interacting objects are large and flat, e.g. walls, the shape of the spherical wavefront is preserved after reflection, so the scattering sources would be traced back to the Tx location, as shown with some two-bounce paths in Fig. A.9.

6 Conclusion

In this paper, an MLE algorithm with SIC is proposed for channel estimation when both the far-field and the narrowband assumptions are violated. The wideband SWM is used as the generic signal model for estimation. To reduce the computational complexity of traditional MLE algorithms, a two-stage procedure is introduced, which consists of an initialization stage and an estimation refinement stage. To alleviate over-estimation of the channel, the AIC is used to determine the appropriate number of paths in the channel.

The proposed algorithm is applied to estimate parameters of the channel measured with a large-scale antenna array system in a basement at 28 to 30 GHz, including a LoS and an OLoS scenario. It is shown that for near-field estimation problems, the SWM outperforms the PWM significantly in terms of likelihood, number of paths estimated, and power extraction rate. By comparing the estimated PADP from the UCA measurement to that from a rotational horn antenna measurement, it is shown that the majority of channel components are successfully captured.

Moreover, the physical interpretation of the propagation channel is given along with the environment. The estimated scatterer locations are observed to coincide with the physical objects in the environment, such as the walls, the edges of the blackboard, and the Tx. It is observed that reflection does not always create new scattering sources on the interacting objects. This is due to the fact that the original spherical wavefront is preserved after reflection given that the surface of the interacting objects is sufficiently large and flat, e.g. walls. As a result, the scattering sources are traced back to the Tx location for multi-bounce links.

Last but not least, the proposed low-complexity MLE algorithm could be useful for extracting channel parameters for standard channel models (e.g. 3GPP channel model) with the SWM taken into account. Extension on the algorithm for dual-polarization estimation will be conducted in future work. The findings on the propagation mechanisms and the obtained channel characteristics at 28 to 30 GHz would be helpful for channel characterization at high frequency bands.

References

[1] F. Rusek, D. Persson, B. K. Lau, E. G. Larsson, T. L. Marzetta, O. Edfors, and F. Tufvesson, "Scaling Up MIMO: Opportunities and Challenges with Very Large Arrays," *IEEE Signal Processing Magazine*, vol. 30, no. 1, pp. 40–60, 2013.

[2] D. Tse and P. Viswanath, *Fundamentals of wireless communication*. Cambridge university press, 2005.

[3] J. Kivinen, "60-GHz Wideband Radio Channel Sounder," *IEEE Transactions on Instrumentation and Measurement*, vol. 56, no. 5, pp. 1831–1838, 2007.

[4] W. Zhu and H. Kong, "mmWave MIMO channel sounding for 5G," in *1st International Conference on 5G for Ubiquitous Connectivity*, 2014, pp. 192–197.

[5] R. Müller, R. Herrmann, D. A. Dupleich, C. Schneider, and R. S. Thomä, "Ultrawideband Multichannel Sounding for mm-Wave," in *The 8th European Conference on Antennas and Propagation (EuCAP 2014)*, 2014, pp. 817–821.

[6] X. Gao, O. Edfors, F. Rusek, and F. Tufvesson, "Massive MIMO Performance Evaluation Based on Measured Propagation Data," *IEEE Transactions on Wireless Communications*, vol. 14, no. 7, pp. 3899–3911, 2015.

[7] V. Kristem, S. Sangodoyin, C. U. Bas, M. Käske, J. Lee, C. Schneider, G. Sommerkorn, J. Zhang, R. S. Thomä, and A. F. Molisch, "3D MIMO Outdoor-to-Indoor Propagation Channel Measurement," *IEEE Transactions on Wireless Communications*, vol. 16, no. 7, pp. 4600–4613, 2017.

[8] À. O. Martínez, E. De Carvalho, and J. Ø. Nielsen, "Massive MIMO properties based on measured channels: Channel hardening, user decorrelation and channel sparsity," in *2016 50th Asilomar Conference on Signals, Systems and Computers*, 2016, pp. 1804–1808.

[9] B. Ai, K. Guan, R. He, J. Li, G. Li, D. He, Z. Zhong, and K. M. S. Huq, "On Indoor Millimeter Wave Massive MIMO Channels: Measurement and Simulation," *IEEE Journal on Selected Areas in Communications*, vol. 35, no. 7, pp. 1678–1690, 2017.

[10] J. Hejselbaek, W. Fan, and G. F. Pedersen, "Ultrawideband VNA based channel sounding system for centimetre and millimetre wave bands," in *IEEE International Symposium on Personal, Indoor and Mobile Radio Communications, PIMRC*, 2016, pp. 1–6.

[11] S. Salous, S. M. Feeney, X. Raimundo, and A. A. Cheema, "Wideband MIMO Channel Sounder for Radio Measurements in the 60 GHz Band," *IEEE Transactions on Wireless Communications*, vol. 15, no. 4, pp. 2825–2832, 2016.

[12] B. Ai, X. Cheng, T. Kurner, Z. D. Zhong, K. Guan, R. S. He, L. Xiong, D. W. Matolak, D. G. Michelson, and C. Briso-Rodriguez, "Challenges toward wireless communications for high-speed railway," *IEEE Transactions on Intelligent Transportation Systems*, vol. 15, no. 5, pp. 2143–2158, 2014.

[13] R. He, O. Renaudin, V. M. Kolmonen, K. Haneda, Z. Zhong, B. Ai, S. Hubert, and C. Oestges, "Vehicle-to-Vehicle Radio Channel Characterization in Crossroad Scenarios," *IEEE Transactions on Vehicular Technology*, vol. 65, no. 8, pp. 5850–5861, 2016.

[14] K. Haneda, J. Järveläinen, A. Karttunen, M. Kyrö, and J. Putkonen, "A statistical spatio-temporal radio channel model for large indoor environments at 60 and 70 GHz," *IEEE Transactions on Antennas and Propagation*, vol. 63, no. 6, pp. 2694–2704, 2015.

[15] J. Chen, X. Yin, X. Cai, and S. Wang, "Measurement-Based Massive MIMO Channel Modeling for Outdoor LoS and NLoS Environments," *IEEE Access*, vol. 5, pp. 2126–2140, 2017.

[16] W. Fan, I. Carton, J. Nielsen, K. Olesen, and G. F. Pedersen, "Measured wideband characteristics of indoor channels at centimetric and millimetric bands," *Eurasip Journal on Wireless Communications and Networking*, vol. 2016, no. 1, pp. 1–13, 2016.

[17] C. A. Balanis, *Antenna Theory: Analysis and Design*. John Wiley & Sons, 2005.

[18] A. J. Weiss and B. Friedlander, "Range and Bearing Estimation Using Polynomial Rooting," *IEEE Journal of Oceanic Engineering*, vol. 18, no. 2, pp. 130–137, 1993.

[19] C. Capps, "Near field or far field?" *EDN Magazine*, vol. 46, no. 18, pp. 95–102, 2001.

[20] L. Liu, D. W. Matolak, C. Tao, Y. Lu, and H. Chen, "Far region boundary definition of linear massive MIMO antenna arrays," in *2015 IEEE 82nd Vehicular Technology Conference (VTC2015-Fall)*, 2015, pp. 1–6.

[21] T. mmMAGIC project, "Use case characterization KPIs and preferred suitable frequency ranges for future 5G systems between 6 GHz and 100 GHz," Document Number: ICT-671650-mmMAGIC/D1.1, Tech. Rep., 2015. [Online]. Available: https://bscw.5g-mmmagic.eu/pub/bscw.cgi/d54427/mmMAGIC{_}D1.1.pdf

[22] The MiWEBA project, "Channel Modeling and Characterization," Deliverable FP7-ICT 368721/D5.1, MiWEBA, Tech. Rep., 2014.

[23] 3GPP, "Study on channel model for frequencies from 0.5 to 100 GHz," Tech. Rep. 3GPP TR 38.901 V14.0.0, 2017. [Online]. Available: http://www.etsi.org/standards-search

[24] K. Haneda, J. Zhang, L. Tan, G. Liu, Y. Zheng, H. Asplund, J. Li, Y. Wang, D. Steer, C. Li, T. Balercia, S. Lee, Y. Kim, A. Ghosh, T. Thomas, T. Nakamura, Y. Kakishima, T. Imai, H. Papadopoulos, T. S. Rappaport, G. R. Maccartney, M. K. Samimi, S. Sun, O. Koymen, S. Hur, J. Park, C. Zhang, E. Mellios, A. F. Molisch, S. S. Ghassamzadeh, and A. Ghosh, "5G 3GPP-like channel models for outdoor urban microcellular and macrocellular environments," in *2016 IEEE 83rd Vehicular Technology Conference (VTC Spring)*, 2016, pp. 1–7.

[25] C. F. Lopez, C. X. Wang, and R. Feng, "A novel 2D non-stationary wideband massive MIMO channel model," in *2016 IEEE 21st International Workshop on Computer Aided Modelling and Design of Communication Links and Networks (CAMAD)*, 2016, pp. 207–212.

[26] K. Haneda, J. I. Takada, and T. Kobayashi, "A parametric UWB propagation channel estimation and its performance validation in an anechoic chamber," *IEEE Transactions on Microwave Theory and Techniques*, vol. 54, no. 4, pp. 1802–1811, 2006.

[27] Y. Ji, W. Fan, and G. F. Pedersen, "Near-Field Signal Model for Large-Scale Uniform Circular Array and Its Experimental Validation," *IEEE Antennas and Wireless Propagation Letters*, vol. 16, pp. 1237–1240, 2017.

[28] X. Yin, S. Wang, N. Zhang, L. Tian, and B. Ai, "Scatterer Localization using Large-scale Antenna Arrays based on A Spherical Wavefront Parametric Model," *IEEE Transactions on Wireless Communications*, vol. 16, no. 10, pp. 6543–6556, 2017.

[29] H. Krim and M. Viberg, "Two decades of array signal processing research: The parametric approach," *IEEE Signal Processing Magazine*, vol. 13, no. 4, pp. 67–94, 1996.

[30] A. F. Molisch, "Ultrawideband propagation channels-theory, measurement, and modeling," *IEEE Transactions on Vehicular Technology*, vol. 54, no. 5, pp. 1528–1545, 2005.

[31] A. B. Baggeroer, W. A. Kuperman, and H. Schmidt, "Matched field processing: Source localization in correlated noise as an optimum parameter estimation problem," *The Journal of the Acoustical Society of America*, vol. 83, no. 2, pp. 571–587, 1988.

[32] J. A. Cadzow, "Multiple source location: The signal subspace approach," in *Twenty-Third Asilomar Conference on Signals Systems and Computers 1989*, vol. 2, no. 7, 1989, pp. 1110–1125.

[33] T. Tung, K. Yao, D. Chen, R. Hudson, and C. Reed, "Source localization and spatial filtering using wideband MUSIC and maximum power beamforming for multimedia applications," in *1999 IEEE Workshop on Signal Processing Systems. SiPS 99. Design and Implementation (Cat. No.99TH8461)*, 1999, pp. 625–634.

[34] Y. Wang, J. Li, P. Stoica, M. Sheplak, and T. Nishida, "Wideband RELAX and wideband CLEAN for aeroacoustic imaging," *The Journal of the Acoustical Society of America*, vol. 115, no. 2, pp. 757–767, 2004.

[35] R. Schmidt, "Multiple emitter location and signal parameter estimation," *IEEE Transactions on Antennas and Propagation*, vol. 34, no. 3, pp. 276–280, 1986.

[36] R. Roy and T. Kailath, "ESPRIT-Estimation of Signal Parameters Via Rotational Invariance Techniques," *IEEE Transactions on Acoustics, Speech, and Signal Processing*, vol. 37, no. 7, pp. 984–995, 1989.

[37] T. Hirano and N. Kikuma, "Location Estimation of Multiple Near-Field Broadband Sources by Combined Use of DOA-Matrix Method and SAGE Algorithm in Array Antenna Processing," in *2012 International Symposium on Antennas and Propagation (ISAP)*, 2012, pp. 363–366.

[38] B. H. Fleury, M. Tschudin, R. Heddergott, D. Dahlhaus, and K. I. Pedersen, "Channel parameter estimation in mobile radio environments using the SAGE algorithm," *IEEE Journal on Selected Areas in Communications*, vol. 17, no. 3, pp. 434–450, 1999.

[39] A. Richter, "Estimation of Radio Channel Parameters : Models and Algorithms," Ph.D. dissertation, 2005.

[40] J. Chen, S. Wang, and X. Yin, "A Spherical-Wavefront-Based Scatterer Localization Algorithm Using Large-Scale Antenna Arrays," *IEEE Communications Letters*, vol. 20, no. 9, pp. 1796–1799, 2016.

[41] J. A. Fessler and A. O. Hero, "Space-Alternating Generalized Expectation-Maximization Algorithm," *IEEE Transactions on Signal Processing*, vol. 42, no. 10, pp. 2664–2677, 1994.

[42] Y. Yu, H. S. Lui, C. H. Niow, and H. T. Hui, "Improved DOA estimations using the receiving mutual impedances for mutual coupling compensation: An experimental study," *IEEE Transactions on Wireless Communications*, vol. 10, no. 7, pp. 2228–2233, 2011.

[43] F. Zhang, W. Fan, and G. F. Pedersen, "Frequency-Invariant Uniform Circular Array for Wideband mm-Wave Channel Characterization," *IEEE Antennas and Wireless Propagation Letters*, vol. 16, pp. 641–644, 2017.

[44] Y. Ji, W. Fan, and G. F. Pedersen, "Channel estimation using spherical-wave model for indoor LoS and obstructed LoS scenarios," in *2017 11th European Conference on Antennas and Propagation, EUCAP 2017*, 2017, pp. 2459–2462.

[45] H. Akaike, "A New Look at the Statistical Model Identification," *IEEE Transactions on Automatic Control*, vol. 19, no. 6, pp. 716–723, 1974.

[46] K. P. Burnham and D. R. Anderson, *Model Selection and Multimodel Inference: A Practical Information-Theoretic Approach*. Springer New York, 2003.

[47] R. He, Z. Zhong, B. Ai, J. Ding, Y. Yang, and A. F. Molisch, "Short-term fading behavior in high-speed railway cutting scenario: Measurements, analysis, and statistical models," *IEEE Transactions on Antennas and Propagation*, vol. 61, no. 4, pp. 2209–2222, 2013.

[48] D. B. Williams, "Counting the Degrees of Freedom When Using AIC and MDL to Detect Signals," *IEEE Transactions on Signal Processing*, vol. 42, no. 11, pp. 3282–3284, 1994.

[49] S. Boyd and L. Vandenberghe, *Convex Optimization*. Cambridge University Press, 2004.

[50] D. H. Johnson and D. E. Dudgeon, *Array signal processing: concepts and techniques*. Simon & Schuster, 1992.

[51] A-INFO, "Data sheet for biconical antenna SZ-2003000/P," Tech. Rep. [Online]. Available: http://www.ainfoinc.com/en/pro{_}pdf/new{_}products/antenna/Bi-ConicalAntenna/tr{_}SZ-2003000-P.pdf

[52] S. Mota, M. O. Garcia, A. Rocha, and F. Pérez-Fontán, "Clustering of the multipath radio channel parameters," in *Proceedings of the 5th European Conference on Antennas and Propagation (EUCAP)*, 2011, pp. 3232–3236.

[53] IRACON, "COST Action CA15104 First Scientific Annual Report," Tech. Rep., 2017.

[54] B. H. Fleury, P. Jourdan, and A. Stucki, "High-resolution channel parameter estimation for MIMO applications using the SAGE algorithm," in *2002 International Zurich Seminar on Broadband Communications Access - Transmission - Networking (Cat. No.02TH8599)*, 2002, pp. 30.1–30.9.

[55] G. Del Galdo, V. Algeier, N. Czink, and M. Haardt, "Spatial Localization of Scattering Objects from High-Resolution Parameter Estimates," in *NEWCOM-ACORN Workshop*, no. 1, 2006, pp. 1–21.

[56] J. Poutanen, K. Haneda, J. Salmi, V.-m. Kolmonen, A. Richter, P. Almers, and P. Vainikainen, "Development of measurement-based ray tracer for multi-link double directional propagation parameters," in *2009 3rd European Conference on Antennas and Propagation*, 2009, pp. 2622–2626.

Paper B

A Map-Free Indoor Localization Method Using Ultrawideband Large-Scale Array Systems

Yilin Ji, Johannes Hejselbæk, Wei Fan,
and Gert Frølund Pedersen

The paper has been published in the
IEEE Antennas and Wireless Propagation Letters Vol. 17, No. 9, pp. 1682–1686,
2018.

The layout has been revised.

Abstract

In this paper, we propose a novel map-free indoor localization method using ultrawideband large-scale array systems in high frequency bands. The proposed localization method comprises two stages, namely a channel-estimation stage and a target-localization stage. Due to the large array aperture, the locations of the scatterers associated to the multipath components (MPCs) can be estimated with the spherical wavefront model. The estimated scatterers are further used as virtual anchors to estimate the location of the target through trilateration. Since the scatterer locations are obtained from channel measurements, the map of the environment is not needed for localization. The proposed method is also assessed with measurements conducted in a cluttered indoor environment with line-of-sight (LoS) and non-line-of-sight (NLoS) scenarios. Results show the proposed algorithm attains good localization accuracy in both scenarios.

1 Introduction

Indoor localization has always been attracting huge attention in both industry and academia due to its various applications. In the context of radio-based localization, many algorithms have been developed and can be categorized with respect to different criteria [1]. One of such criteria is whether the underlying algorithm makes use of channel multipath components (MPCs). For algorithms only utilizing line-of-sight (LoS) components, the main drawback is that they do not work well in non-line-of-sight (NLoS) scenarios, which limits their application in general use cases. On the contrary, MPC-assisted algorithms exploit information from all MPCs for localization not only in LoS scenarios but also in NLoS scenarios [2–4].

Another important criterion is whether it requires the map of the environment to perform localization. Since the map of an environment is not always easily available, and can be dynamic due to people walking or interior changes, a map-free algorithm becomes very helpful in this case. In the literature [2, 3, 5], a map-free algorithm called simultaneous localization and mapping (SLAM) was proposed. The SLAM algorithm is basically a recursive Bayesian filter which updates the state model and the observation model sequentially and recursively. However, a control vector consisting of motion information is needed to formulate the state model, so additional devices, e.g. accelerometers or gyroscopes, are required to provide relevant information.

In this paper, we propose a novel map-free indoor localization method using ultrawideband large-scale array systems at high frequency bands. The proposed method comprises two stages, namely a channel-estimation stage and a target-localization stage. In the channel-estimation stage, parameters of the MPCs are estimated from measurements with the spherical wavefront

model [6, 7]. In the target-localization stage, the locations of the scatterers in the environment are estimated with respect to the array location. The estimated scatterers are then used as virtual anchors to locate the target through trilateration.

The key differentiator of our method is the virtual anchors are not derived from the image source method with respect to the map but from the estimation of the physical scatterers in the environment instead. Therefore, the array location is the only geographical information needed to perform target localization. Moreover, the influence of people walking or interior changes is inherently conveyed in the changes of the virtual anchor locations, so the proposed method is also adaptive to dynamic environments. In addition, the proposed algorithm is assessed with measurements conducted in a cluttered room with both LoS and NLoS scenarios.

2 Proposed Localization Algorithm

2.1 Channel Representation and Parameter Estimation

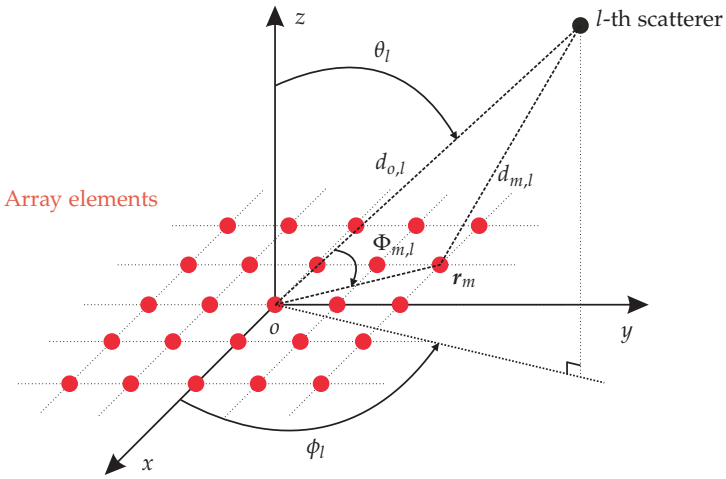

Fig. B.1: The local coordinate system at the array side. Note that a uniform rectangular array is shown for illustration, and it can be replaced with arbitrary array structures in practice.

A propagation channel can be assumed to be represented as the superposition of a number of MPCs. For a single-input multiple-output (SIMO) system consisting of an M-element receive array, the time-invariant channel transfer function between the transmit antenna at the m-th receive array ele-

ment with $m \in [1, M]$ can be expressed as [8, 9]

$$H_m(f;\boldsymbol{\Theta}) = \sum_{l=1}^{L} H_m(f;\boldsymbol{\Theta}_l), \tag{B.1}$$

where f is the frequency, L is the number of MPCs, and $\boldsymbol{\Theta} = \{\boldsymbol{\Theta}_1, ..., \boldsymbol{\Theta}_L\}$ is the set of the parameters of all L MPCs. An illustration of the local coordinate system at the receive side is shown in Fig. B.1. Considering the case where the aperture of the receive array is large enough that spherical wavefront is observed at the array, the contribution of the l-th MPC at the m-th receive array element can be written as

$$\begin{aligned} H_m(f;\boldsymbol{\Theta}_l) = \alpha_l \cdot \frac{g_m(f;\phi_l,\theta_l)}{4\pi f d_{m,l}/c} \cdot \exp\{-j2\pi f \tau_l\} \\ \cdot \exp\{-j2\pi f (d_{m,l} - d_{o,l})/c\}, \end{aligned} \tag{B.2}$$

where $\boldsymbol{\Theta}_l = \{\alpha_l, \phi_l, \theta_l, d_{o,l}, \tau_l\}$ is the set of parameters of the l-th MPC, including the complex amplitude, the azimuth angle of arrival, the elevation angle of arrival, the distance from the scatterer to the array center, and the delay, respectively. Further, c is the speed of light, g_m is the antenna field pattern of the m-th array element, and $d_{m,l}$ is the distance from the scatterer to the m-th array element. The distance $d_{m,l}$ is calculated with the law of cosines as

$$d_{m,l} = \sqrt{d_{o,l}^2 + \|\boldsymbol{r}_m\|^2 - 2 d_{o,l} \|\boldsymbol{r}_m\| \cos\Phi_{m,l}}, \tag{B.3}$$

where $\|\cdot\|$ denotes the Euclidean norm operator, $\boldsymbol{r}_m$ is the coordinate vector of the m-th array element, and $\Phi_{m,l}$ is the angle between the vector $\boldsymbol{r}_m$ and the direction of arrival with respect to the array center. $\cos\Phi_{m,l}$ can be explicitly expressed with $\boldsymbol{r}_m$ and a unit direction vector $\boldsymbol{e}(\phi_l, \theta_l) = [\cos\phi_l \sin\theta_l, \sin\phi_l \sin\theta_l, \cos\theta_l]$ as

$$\cos\Phi_{m,l} = \frac{\langle \boldsymbol{r}_m, \boldsymbol{e}(\phi_l,\theta_l)\rangle}{\|\boldsymbol{r}_m\|}, \tag{B.4}$$

where $\langle\cdot,\cdot\rangle$ denotes the inner product operator. Note that $d_{o,l} = \tau_l \cdot c$ if the l-th MPC corresponds to a LoS component.

By applying high-resolution channel estimation algorithms [7–9] to the channel measurements, it is possible to estimate the parameter set $\boldsymbol{\Theta}$ for all MPCs. Note that an array of a larger aperture size results in finer resolutions of the parameters $\{\phi_l, \theta_l, d_{o,l}\}$ for estimation, and hence a smaller error in channel estimation and target localization.

2.2 Localization Principle

Two important assumptions are made for cluttered indoor high-frequency-band channels. We assume:

(i) The estimated MPCs mainly consist of one-bounce links with or without LoS components depending on the scenarios.

(ii) Most of the estimated MPCs are induced by scattering from physical obstacles.

The first assumption can be made due to the high path loss at high frequency bands and the limited dynamic range of measurement systems. The second assumption can be made due to the small wavelength at high frequency bands, which becomes comparable to the size of physical obstacles in a typical cluttered indoor environment.

2.2.1 Physical obstacles identification

The transmit antenna and the physical obstacles are considered as the scattering sources in the environment. Essentially, the scatterers associated to the MPCs correspond to those scattering sources, or equivalently, to the transmit antenna and the physical obstacles in the environment. Once the parameters of MPCs are estimated, we can further estimate the locations of the scatterers in the environment. A diagram of the principle is shown in Fig. B.2. With the knowledge of the receiver location, we can draw a line segment of length $d_{o,l}$ from the receive array center in the direction of $\boldsymbol{e}(\phi_l, \theta_l)$ for the l-th MPC (shown as red lines). The l-th scatterer is assumed to be located on the end of the line segment (shown as blue pentagrams). The location of the l-th scatterer is then estimated as

$$\hat{\boldsymbol{r}}_{s,l} = \boldsymbol{r}_o + d_{o,l} \cdot \boldsymbol{e}(\phi_l, \theta_l), \tag{B.5}$$

where $\boldsymbol{r}_o$ is the coordinate vector of the receive array center.

Note that the true location of the l-th scatterer in practice does not always coincide with the estimate calculated from (B.5). For example, if the surface of the physical obstacle is sufficiently large and flat compared to the wavelength, specular reflection occurs. In this case, the estimated scatterer location corresponds to the mirror image of its true location with respect to the reflection surface. On the other hand, objects such as metal frames or heating radiators, which can be usually found in indoor environments, induce scattering points on them. With the second assumption, the majority of the estimated scatterer locations coincide with their true locations in typical cluttered indoor environments, such as shopping malls, supermarkets, or warehouses.

2.2.2 Target localization

The estimated scatterers are used as virtual anchors in the environment. With the first assumption, the majority of the estimated MPCs consist of

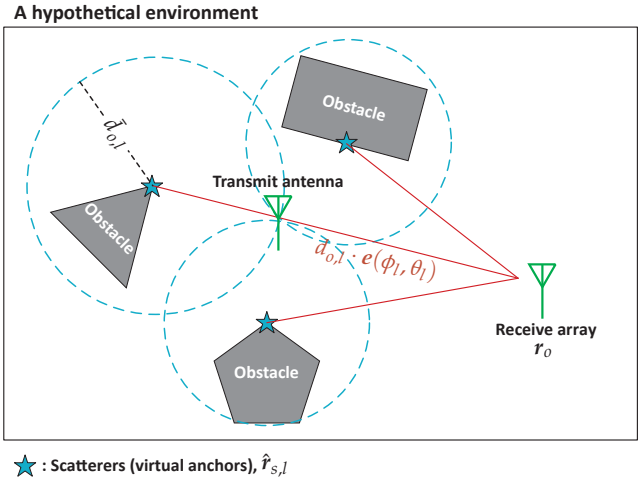

Fig. B.2: Diagram of the proposed localization method. Physical obstacles are estimated as scatterers from measurements, and are further used as virtual anchors to locate the transmitter.

one-bounce links with or without a LoS component depending on the underlying scenario. The target location can be estimated through the optimization problem

$$\hat{\boldsymbol{r}}_t = \arg\min_{\boldsymbol{r}} \sum_{l=1}^{L} \left| \|\boldsymbol{r} - \hat{\boldsymbol{r}}_{s,l}\| - \bar{d}_{o,l} \right| \cdot P_l, \tag{B.6}$$

where

$$\bar{d}_{o,l} = \tau_l \cdot c - d_{o,l}, \tag{B.7}$$

is the residual propagation distance of the l-th MPC between the l-th scatterer and the transmit antenna (the radius of the dashed blue circumferences in Fig. B.2), $\boldsymbol{r}$ is the coordinate vector of an arbitrary point in the space, $P_l = \|\alpha_l \cdot \frac{c}{4\pi f d_{o,l}}\|^2$ is the power of the l-th MPC, and $|\cdot|$ denotes the absolute value operator. Equation (B.6) can be solved efficiently through coarse-to-fine search techniques.

A high localization accuracy is expected when the scatterers are well-separated in space around the target as in Fig. B.2. However, when the scatterers are located closely, the accuracy of trilateration deteriorates. It is also worth mentioning that the validity of the localization principle is based on the validity of the two important assumptions made for high-frequency-band channels in cluttered indoor environments. Therefore, the performance of the proposed localization method is expected to deteriorate in the cases where the two assumptions do not hold well, e.g. at low frequency bands or in empty rooms where specular reflections are dominant.

3 Experimental Evaluation

3.1 Measurement Campaign

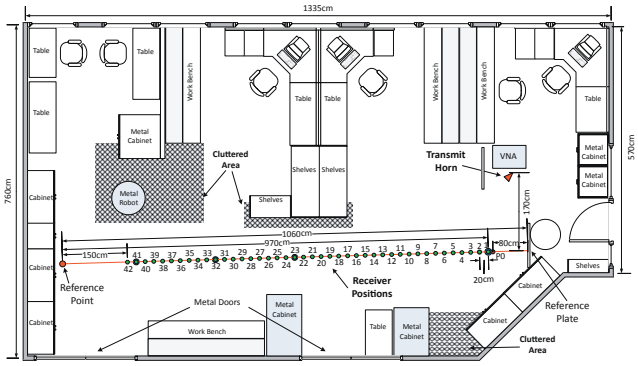

Fig. B.3: The floor plan of the measurement environment and the 42 receiver positions. The centers of the receive arrays are depicted as green dots.

The measurements were conducted in an indoor environment with a vector-network-analyzer-based (VNA) channel sounder [6]. The SIMO channels were measured with a horn antenna on the transmit side and a virtual uniform circular array (UCA) on the receive side. The virtual UCA was formed by mounting a biconical antenna on a turntable with a radius of 25 cm stepping every 1° in the azimuth plane. The horn antenna has a half-power beamwidth of 54° in the azimuth plane, and an antenna gain of 10 dBi. Both the transmit antenna and the receive antenna were placed 1 m above the floor. The channel frequency responses were measured with 1500 frequency points evenly over 26 GHz to 30 GHz, which corresponds to a range (i.e. delay times speed of light) resolution of 7.5 cm. The floor plan of the environment is shown in Fig. B.3. In total, 42 receiver positions were measured along a reference line (red) with 20 cm spacing. The centers of the receive arrays for these positions are depicted as green dots. Single channel snapshots were measured at most of those positions, and multiple channel snapshots were measured in the 1 cm vicinity of position 1, 23, 32, and 41, which are denoted as green dots surrounded by blue rings in Fig. B.3. With respect to the transmit antenna position, the receiver moves from the LoS region to the NLoS region as the position index increases. Detailed descriptions of the measurement campaign can be found in [6].

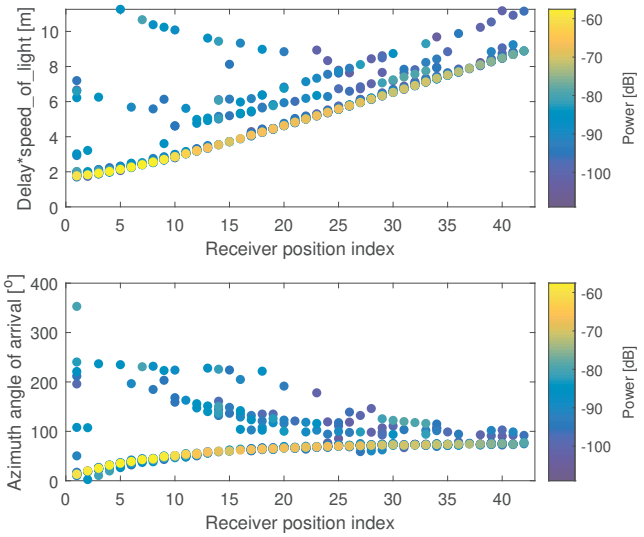

Fig. B.4: The estimated MPCs against receiver positions in the propagation distance and the azimuth angle of arrival domain, respectively.

3.2 Results Analysis

The channel measurement data are processed with a maximum likelihood estimator [7] to extract the MPCs, and the estimation results for all receiver positions are presented in Fig. B.4. It shows as the receiver position index increases, the power of the LoS component becomes weaker, which indicates the underlying channel is turning from the LoS to the NLoS. In addition, the azimuth angles of arrival of the MPCs converge to a confined region around 90°. Since the proposed localization algorithm utilizes the spatial richness of the channel, it may probably lead to a deterioration in the localization accuracy.

The localization results at receiver position 23 and 39 are shown in Fig. B.5 as the examples for the LoS and the NLoS scenarios, respectively. For position 23 (Fig. B.5(a)), we can see the scatterer corresponding to the LoS component is estimated at the transmitter location. In addition, the circumferences of the other MPCs also intersect around the true transmitter location, which leads to high estimation accuracy. For position 39 (Fig. B.5(b)), the circumferences of most MPCs still intersect around the true transmitter location. However, due to the decreased spatial richness at position 39 as shown in Fig. B.4, the localization is less accurate than that at position 23.

The results for all 42 positions are shown in Fig. B.6. We can see the majority of the estimated transmitter locations are close to the true location. The estimated scatterer locations for all receiver positions are also superimposed

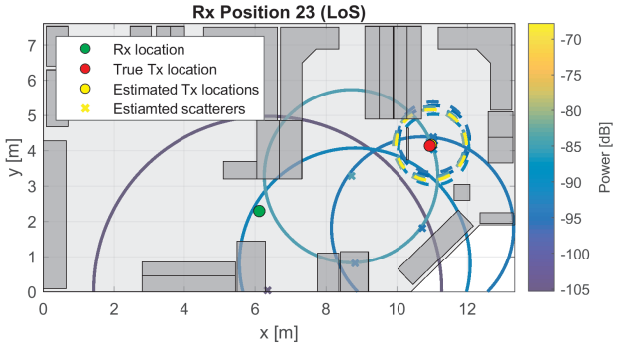

(a)

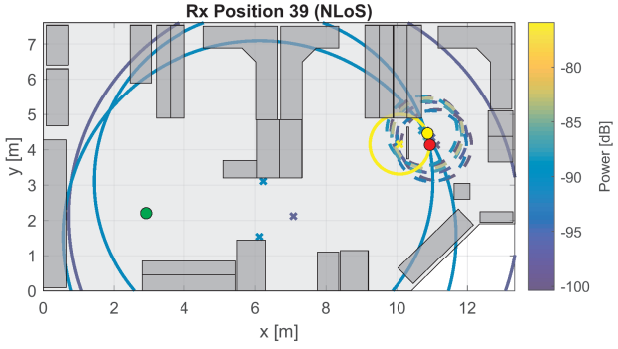

(b)

Fig. B.5: The localization results at receiver (Rx) position 23 and 39, respectively. The range of the transmitter (Tx) with respect to the l-th scatterer is shown as a solid circumference with its radius equal to $\tilde{d}_{o,l}$. Note when $\tilde{d}_{o,l} = 0$, dashed circumferences with 1 m radius are shown for visualization. The color of the circumferences and crosses represents the power of the MPCs.

in Fig. B.6. We can see that some of the estimated scatterers are surrounding the true transmitter location. This is because the scatterers associated to the LoS components correspond to the transmitter itself. The rest of the estimated scatterer locations are either close to the physical obstacles or corresponding to the ground reflection along the propagation paths.

Further, the error distance between the true location of the transmit antenna $\boldsymbol{r}_t$ and the estimated location $\hat{\boldsymbol{r}}_t$ is calculated as $\varepsilon = \|\boldsymbol{r}_t - \hat{\boldsymbol{r}}_t\|$. The resulting error distance for the 42 receiver positions are shown in Fig. B.7. It shows a trend that the error distance increases with the position index, which is in agreement with the discussion for Fig. B.4. Nevertheless, the location of the transmit antenna is still well estimated, and the majority of the error distances are below 30 cm, which is around 4 times the underlying range resolution.

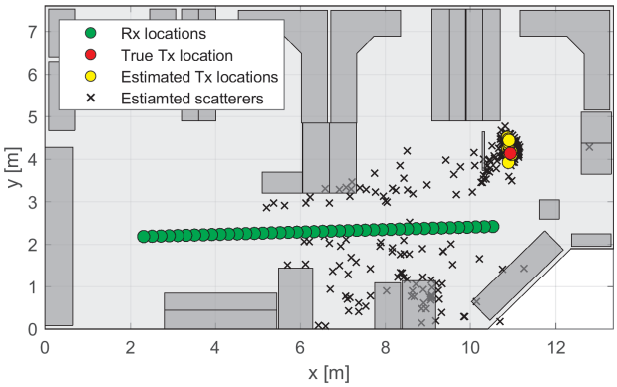

Fig. B.6: The estimated transmitter locations $\hat{\boldsymbol{r}}_t$ and the estimated scatterer locations $\hat{\boldsymbol{r}}_{s,l}$ for all 42 receiver positions superimposed.

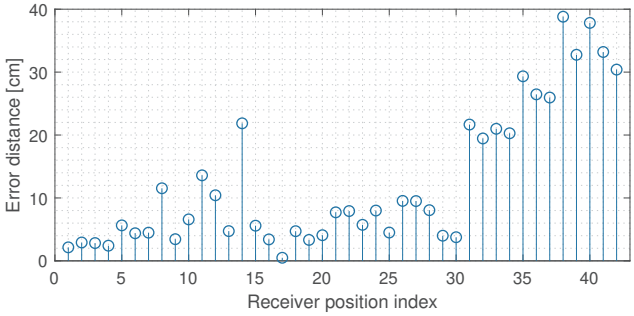

Fig. B.7: The error distance ε obtained over the 42 receiver positions. The results shown here are obtained with single channel snapshots.

Note that the error distances shown in Fig. B.7 are obtained from single channel snapshots. One potential reason for the large error distances at these singular positions can be due to the lack of channel snapshots. Therefore, the error distance is further calculated at the positions where multiple channel snapshots were measured in their 1 cm vicinity. The corresponding error distances at those positions are given in Table B.1. It shows a slight move of the receiver position may introduce larger variation in localization results for the NLoS scenario than for the LoS scenario. The composite error distance is further calculated with respect to the mean location of $\hat{\boldsymbol{r}}_t$ over multiple snapshots. It also shows averaging results from multiple snapshots helps to improve the localization accuracy for the NLoS scenario, e.g. at position 41.

Table B.1: Error Distances (unit: [cm]) in the Vicinity of Positions with Multiple Channel Snapshots

Position Index	#1	#23	#32	#41
Snapshot 1	2.15	5.73	20.56	33.20
Snapshot 2	6.31	4.42	19.46	70.94
Snapshot 3	2.39	4.42	–	72.89
Composite	3.11	4.57	19.99	12.41

4 Conclusions

In this paper, we propose a map-free indoor localization method utilizing ultrawideband large-scale array systems in high frequency bands. Given that massive multiple-input multiple-output (MIMO) systems and high frequency bands are assumed to be deployed in the fifth-generation (5G) communication systems, the proposed indoor localization method can be implemented directly with the setups of the upcoming communication systems. In the proposed method, scatterers in the environment are utilized as virtual anchors to estimate target locations. The advantage of this method is that it does not rely on the map of the environment to perform target localization. The performance of the proposed method is also assessed with measurements conducted in a cluttered room including both LoS and NLoS scenarios. The results show that the error of the estimated target location increases with the distance between the transmitter and the receiver, but the majority of the estimation error are below 30 cm.

References

[1] P. Meissner, "Multipath-Assisted Indoor Positioning," Ph.D. dissertation, Graz University of Technology, 2014.

[2] K. Witrisal, P. Meissner, E. Leitinger, Y. Shen, C. Gustafson, F. Tufvesson, K. Haneda, D. Dardari, A. F. Molisch, A. Conti, and M. Z. Win, "High-accuracy localization for assisted living: 5G systems will turn multipath channels from foe to friend," *IEEE Signal Processing Magazine*, vol. 33, no. 2, pp. 59–70, 2016.

[3] C. Gentner, T. Jost, W. Wang, S. Zhang, A. Dammann, and U. C. Fiebig, "Multipath Assisted Positioning with Simultaneous Localization and Mapping," *IEEE Transactions on Wireless Communications*, vol. 15, no. 9, pp. 6104–6117, 2016.

[4] B. Hanssens, D. Plets, E. Tanghe, C. Oestges, D. P. Gaillot, M. Liénard, T. Li, H. Steendam, L. Martens, and W. Joseph, "An Indoor Variance-Based Localization Technique Utilizing the UWB Estimation of Geometrical Propagation Parameters," *IEEE Transactions on Antennas and Propagation*, vol. 66, no. 5, pp. 2522–2533, 2018.

[5] T. Bailey and H. Durrant-Whyte, "Simultaneous localization and mapping (SLAM): Part I," *IEEE Robotics and Automation Magazine*, vol. 13, no. 2, pp. 99–110, 2006.

[6] J. Hejselbaek, Y. Ji, W. Fan, and G. F. Pedersen, "Channel Sounding System for MM-Wave Bands and Characterization of Indoor Propagation at 28 GHz," *International Journal of Wireless Information Networks*, vol. 24, no. 3, pp. 204–216, 2017. [Online]. Available: http://link.springer.com/10.1007/s10776-017-0365-0

[7] Y. Ji, W. Fan, and G. F. Pedersen, "Channel estimation using spherical-wave model for indoor LoS and obstructed LoS scenarios," in *2017 11th European Conference on Antennas and Propagation, EUCAP 2017*, 2017, pp. 2459–2462.

[8] Y. Wang, J. Li, P. Stoica, M. Sheplak, and T. Nishida, "Wideband RELAX and wideband CLEAN for aeroacoustic imaging," *The Journal of the Acoustical Society of America*, vol. 115, no. 2, pp. 757–767, 2004.

[9] K. Haneda, J. I. Takada, and T. Kobayashi, "A parametric UWB propagation channel estimation and its performance validation in an anechoic chamber," *IEEE Transactions on Microwave Theory and Techniques*, vol. 54, no. 4, pp. 1802–1811, 2006.

Paper C

Antenna Correlation Under Geometry-Based Stochastic Channel Models

Yilin Ji, Wei Fan, Pekka Kyösti, Jinxing Li,
and Gert Frølund Pedersen

The paper has been published in the
IEEE Antennas and Wireless Propagation Letters Vol. 18, No. 12, pp. 2567–2571,
2019.

The layout has been revised.

Abstract

Antenna correlation is an important measure for designing multiple-input multiple-output (MIMO) antenna systems. A lower antenna correlation indicates a better MIMO performance that can be achieved with the underlying antenna systems. In the antenna design community, it is very common to evaluate the antenna correlation with isotropic or non-isotropic (e.g. Gaussian-distributed) angular power spectrum (APS) as baselines. On the other hand, antenna correlation can also be evaluated via channel transfer function (CTF) under the a given propagation channel, e.g. drawn from the bi-directional geometry-based stochastic channel model. In this paper, the analytic forms for the antenna correlation based on the APS and the CTF are derived, respectively, with their similarities and differences explained. Moreover, a numerical example is also given with a standard channel model to support our findings.

1 Introduction

Antenna correlation (also known as envelope correlation if absolute-squared) is widely used as a measure in both the antenna field and the propagation field for multiple-input multiple-output (MIMO) communications. It shows how much the received signals at different antenna ports correlate with each other. A lower antenna correlation indicates that a better performance can be expected for MIMO communications.

Without loss of generality, if we take the antenna correlation on the receive (Rx) side for example, the Rx antenna correlation can be analytically calculated with arbitrary incident angular power spectrum (APS) and Rx antenna field pattern [1–3]. It is very common in the antenna design community to evaluate the antenna correlation with some simplified channel models such as APS following the isotropic or non-isotropic (e.g. Gaussian or Laplacian) distributions as baselines [4].

On the other hand, Rx antenna correlation can also be calculated with another fundamental approach, i.e. through the cross correlation of the received signals at Rx antennas [5, 6]. This approach requires the knowledge of the channel transfer function (CTF) which describes the input-output relation between the transmit (Tx) and the Rx antenna ports of a communication system under a given propagation channel. However, not only the Rx antenna radiation pattern but also the Tx antenna radiation pattern are inherently embedded in the CTF, whereas the APS only describes the pure channel spatial characteristics with the Tx and Rx antenna radiation pattern de-embedded. Therefore, there might be some discrepancy between the two approaches introduced by the additional Tx antenna spatial selectivity in the second approach. Straightforwardly, stronger Tx antenna spatial selectivity, e.g. the fifth-generation (5G) base stations operating in beam forming modes,

potentially alters the effective APS observed on the Rx side more severely, and hence leads to a more pronounced inconsistency between the two Rx antenna correlation approaches.

In this paper, we go through the derivation of the two antenna correlation approaches from APS and CTF, respectively. Both the two approaches are evaluated under the geometry-based stochastic channel model (GSCM), which has been developed in the propagation field and adopted in the standard [5, 7, 8], and the analytic form of the antenna correlation under the GSCM model is given explicitly. The connection between the two approaches is built through the spread function [9]. The difference between the end results of the antenna correlation from the two approaches are clarified, which shows the effect of the Tx antenna spatial selectivity on the resulting Rx correlation with the CTF approach. Finally, a numerical example is given with a standard channel model [5]. The main contribution of this paper is to bridge the gap between the two approaches via both theoretical analysis and numerical simulation, which has not been reported in the literature to our best knowledge.

The notations used in the paper are summarized as follow: $(\cdot)^{\mathrm{T}}$, $(\cdot)^*$, $|\cdot|$, and $\odot$ are the transpose, the complex conjugate, the absolute value, and the Hadamard product operator, respectively. Moreover, $cov\{\cdot,\cdot\}$, $var\{\cdot\}$, and $\mathbb{E}\{\cdot\}$ are the covariance, variance, and expectation operator, respectively.

2 Propagation Channel Model

2.1 Channel Transfer Function

The propagation channel is usually modelled as the superposition of a number of paths. For a MIMO system consisting of S Tx antennas and U Rx antennas, the CTF from the sth Tx antenna to the uth Rx antenna at time t and frequency f can be expressed as [9]

$$H_{u,s}(t,f) = \iiiint \begin{bmatrix} F_s^{\mathrm{V}}(\mathbf{\Omega}^{\mathrm{Tx}}) \\ F_s^{\mathrm{H}}(\mathbf{\Omega}^{\mathrm{Tx}}) \end{bmatrix}^{\mathrm{T}} \boldsymbol{h}(\tau, v, \mathbf{\Omega}^{\mathrm{Tx}}, \mathbf{\Omega}^{\mathrm{Rx}}) \begin{bmatrix} F_u^{\mathrm{V}}(\mathbf{\Omega}^{\mathrm{Rx}}) \\ F_u^{\mathrm{H}}(\mathbf{\Omega}^{\mathrm{Rx}}) \end{bmatrix} \cdot \exp(j2\pi v t) \cdot \exp(-j2\pi f \tau)\, \mathrm{d}\tau\, \mathrm{d}v\, \mathrm{d}\mathbf{\Omega}^{\mathrm{Tx}}\, \mathrm{d}\mathbf{\Omega}^{\mathrm{Rx}}, \tag{C.1}$$

where $\tau, v, \mathbf{\Omega}^{\mathrm{Tx}}, \mathbf{\Omega}^{\mathrm{Rx}}$ are the domains of delay, Doppler frequency, direction of departure (DoD), direction of arrival (DoA), respectively. $F_s^{\mathrm{V}}(\mathbf{\Omega})$ and $F_s^{\mathrm{H}}(\mathbf{\Omega})$ are the antenna field patterns of the sth Tx antenna at direction $\mathbf{\Omega}$ for vertical polarization (V-pol) and horizontal polarization (H-pol), respectively. Similarly, $F_u^{\mathrm{V}}(\mathbf{\Omega})$ and $F_u^{\mathrm{H}}(\mathbf{\Omega})$ are those for the uth Rx antenna. The antenna field pattern is defined with a common phase center for the respective Tx and Rx antenna arrays. The integration is conducted over the full span of the respective domains.

In (C.1), the matrix $\boldsymbol{h}$ is the so-called spread function [9], and within the context of the GSCM models it can be written as

$$\begin{aligned}\boldsymbol{h}(\tau, v, \boldsymbol{\Omega}^{\mathrm{Tx}}, \boldsymbol{\Omega}^{\mathrm{Rx}}) = \sum_{m=1}^{M} \sqrt{P_m} \cdot \boldsymbol{A} \cdot \delta(\tau - \tau_m) \cdot \delta(v - v_m) \\ \cdot \delta(\boldsymbol{\Omega}^{\mathrm{Tx}} - \boldsymbol{\Omega}_m^{\mathrm{Tx}}) \cdot \delta(\boldsymbol{\Omega}^{\mathrm{Rx}} - \boldsymbol{\Omega}_m^{\mathrm{Rx}}),\end{aligned} \tag{C.2}$$

where M is the number of paths, P_m is the power of the mth path, τ_m, v_m, $\boldsymbol{\Omega}_m^{\mathrm{Tx}}$, $\boldsymbol{\Omega}_m^{\mathrm{Rx}}$ are the parameters of the mth path in their respective domains, and $\delta(\cdot)$ is the Dirac delta function. The matrix $\boldsymbol{A}$ is the polarization matrix

$$\boldsymbol{A} = \begin{bmatrix} \exp(j\Phi_m^{\mathrm{VV}}) & \sqrt{\kappa_{1,m}^{-1}} \exp(j\Phi_m^{\mathrm{VH}}) \\ \sqrt{\kappa_{2,m}^{-1}\chi_m^{-1}} \exp(j\Phi_m^{\mathrm{HV}}) & \sqrt{\chi_m^{-1}} \exp(j\Phi_m^{\mathrm{HH}}) \end{bmatrix}, \tag{C.3}$$

where

- Φ_m^{VV}, Φ_m^{VH}, Φ_m^{HV}, and Φ_m^{HH} are the initial phases of the mth path of vertical-to-vertical (VV-pol), vertical-to-horizontal (VH-pol), horizontal-to-vertical (HV-pol), and horizontal-to-horizontal (HH-pol) polarizations, respectively. They are assumed independent and identically distributed (i.i.d.) random variables following the uniform distribution over $[0, 2\pi]$.
- $\kappa_{1,m}$ and $\kappa_{2,m}$ are the cross-polarization ratios (XPR) of the mth path, where $\kappa_{1,m}$ is the power ratio of VV-pol over VH-pol, and $\kappa_{2,m}$ HH-pol over HV-pol. It is usually assumed $\kappa_{1,m} = \kappa_{2,m} = \kappa_m$.
- χ_m is the co-polarization ratio (CPR) of the mth path defined as the power ratio of VV-pol over HH-pol.

Inserting (C.2) and (C.3) into (C.1) yields

$$\begin{aligned}H_{u,s}(t, f) = \sum_{m=1}^{M} \sqrt{P_m} \begin{bmatrix} F_s^{\mathrm{V}}(\boldsymbol{\Omega}_m^{\mathrm{Tx}}) \\ F_s^{\mathrm{H}}(\boldsymbol{\Omega}_m^{\mathrm{Tx}}) \end{bmatrix}^{\mathrm{T}} \mathbf{A} \begin{bmatrix} F_u^{\mathrm{V}}(\boldsymbol{\Omega}_m^{\mathrm{Rx}}) \\ F_u^{\mathrm{H}}(\boldsymbol{\Omega}_m^{\mathrm{Rx}}) \end{bmatrix} \\ \cdot \exp(j2\pi v_m t) \cdot \exp(-j2\pi f \tau_m).\end{aligned} \tag{C.4}$$

For brevity, in the following we abbreviate some of the notation as:
• $F_s^{\mathrm{V}}(\boldsymbol{\Omega}_m^{\mathrm{Tx}}) = F_{s,m}^{\mathrm{V}}$; • $F_s^{\mathrm{H}}(\boldsymbol{\Omega}_m^{\mathrm{Tx}}) = F_{s,m}^{\mathrm{H}}$; • $H_{u,s}(t, f) = H_{u,s}$;
• $F_u^{\mathrm{V}}(\boldsymbol{\Omega}_m^{\mathrm{Rx}}) = F_{u,m}^{\mathrm{V}}$; • $F_u^{\mathrm{H}}(\boldsymbol{\Omega}_m^{\mathrm{Rx}}) = F_{u,m,}^{\mathrm{H}}$.

2.2 Angular Power Spectrum Derived from Spread Function

The joint delay-Doppler-DoD-DoA power spectrum can be derived from the spread function as [9]

$$\boldsymbol{P}(\tau, v, \boldsymbol{\Omega}^{\mathrm{Tx}}, \boldsymbol{\Omega}^{\mathrm{Rx}}) = \mathbb{E}\left\{ \boldsymbol{h}(\tau, v, \boldsymbol{\Omega}^{\mathrm{Tx}}, \boldsymbol{\Omega}^{\mathrm{Rx}}) \odot \boldsymbol{h}(\tau, v, \boldsymbol{\Omega}^{\mathrm{Tx}}, \boldsymbol{\Omega}^{\mathrm{Rx}})^* \right\}. \tag{C.5}$$

Inserting (C.2) into (C.5), and defining $|\delta(x)|^2 \doteq \delta(x)$ with x being the dummy variable, we can obtain

$$\begin{aligned}\boldsymbol{P}(\tau, \upsilon, \boldsymbol{\Omega}^{\mathrm{Tx}}, \boldsymbol{\Omega}^{\mathrm{Rx}}) = \sum_{m=1}^{M} P_m \cdot \overline{\boldsymbol{A}^2} \cdot \delta(\tau - \tau_m) \cdot \delta(\upsilon - \upsilon_m) \\ \cdot \delta(\boldsymbol{\Omega}^{\mathrm{Tx}} - \boldsymbol{\Omega}_m^{\mathrm{Tx}}) \cdot \delta(\boldsymbol{\Omega}^{\mathrm{Rx}} - \boldsymbol{\Omega}_m^{\mathrm{Rx}}),\end{aligned} \tag{C.6}$$

where

$$\overline{\boldsymbol{A}^2} = \mathbb{E}\left\{\boldsymbol{A} \odot \boldsymbol{A}^*\right\} = \begin{bmatrix} 1 & \kappa_m^{-1} \\ \kappa_m^{-1}\chi_m^{-1} & \chi_m^{-1} \end{bmatrix}, \tag{C.7}$$

using the i.i.d. property of the initial phases of the paths [10].

Conventionally, power spectrum is considered as a property of propagation channels, and it is independent on the antennas used on both the Tx and the Rx. In other words, the antenna pattern is de-embedded from the channel. It follows that the power spectrum in one (either marginal or joint) domain can be obtained by integrating the joint power spectrum of higher dimensions over the remaining domains [9]. Therefore, the joint DoD-DoA power spectrum can be derived as

$$\begin{aligned}\boldsymbol{P}(\boldsymbol{\Omega}^{\mathrm{Tx}}, \boldsymbol{\Omega}^{\mathrm{Rx}}) &= \iint \boldsymbol{P}(\tau, \upsilon, \boldsymbol{\Omega}^{\mathrm{Tx}}, \boldsymbol{\Omega}^{\mathrm{Rx}})\, \mathrm{d}\tau\, \mathrm{d}\upsilon \\ &= \sum_{m=1}^{M} P_m \cdot \overline{\boldsymbol{A}^2} \cdot \delta(\boldsymbol{\Omega}^{\mathrm{Tx}} - \boldsymbol{\Omega}_m^{\mathrm{Tx}}) \cdot \delta(\boldsymbol{\Omega}^{\mathrm{Rx}} - \boldsymbol{\Omega}_m^{\mathrm{Rx}}),\end{aligned} \tag{C.8}$$

which is a 2×2 matrix with the polarization relation between the Tx and the Rx described in $\overline{\boldsymbol{A}^2}$.

The power spectrum in the DoA domain can be further derived in a similar way as

$$\boldsymbol{P}(\boldsymbol{\Omega}^{\mathrm{Rx}}) = \int \begin{bmatrix} 1 \\ 1 \end{bmatrix}^{\mathrm{T}} \boldsymbol{P}(\boldsymbol{\Omega}^{\mathrm{Tx}}, \boldsymbol{\Omega}^{\mathrm{Rx}})\, \mathrm{d}\boldsymbol{\Omega}^{\mathrm{Tx}}, \tag{C.9}$$

where the vector of ones describes the antenna de-embedding assumption, and merges the V-pol and H-pol contribution from the Tx side. Inserting (C.8) into (C.9), $\boldsymbol{P}(\boldsymbol{\Omega}^{\mathrm{Rx}})$ can be explicitly expressed in both polarizations as

$$\boldsymbol{P}(\boldsymbol{\Omega}^{\mathrm{Rx}}) = \begin{bmatrix} P^{\mathrm{V}}(\boldsymbol{\Omega}^{\mathrm{Rx}}) \\ P^{\mathrm{H}}(\boldsymbol{\Omega}^{\mathrm{Rx}}) \end{bmatrix}^{\mathrm{T}}, \tag{C.10}$$

where

$$P^{\mathrm{V}}(\mathbf{\Omega}^{\mathrm{Rx}}) = \sum_{m=1}^{M} P_m \cdot (1 + \kappa_m^{-1}\chi_m^{-1}) \cdot \delta(\mathbf{\Omega}^{\mathrm{Rx}} - \mathbf{\Omega}_m^{\mathrm{Rx}}), \tag{C.11a}$$

$$P^{\mathrm{H}}(\mathbf{\Omega}^{\mathrm{Rx}}) = \sum_{m=1}^{M} P_m \cdot (\kappa_m^{-1} + \chi_m^{-1}) \cdot \delta(\mathbf{\Omega}^{\mathrm{Rx}} - \mathbf{\Omega}_m^{\mathrm{Rx}}). \tag{C.11b}$$

In many GSCM models [5, 7, 8], it is often assumed the CPR $\chi_m = 1$, which leads to $P^{\mathrm{V}}(\mathbf{\Omega}^{\mathrm{Rx}}) = P^{\mathrm{H}}(\mathbf{\Omega}^{\mathrm{Rx}})$.

3 Antenna Correlation

3.1 Antenna Correlation from Channel Transfer Function

The antenna correlation between two Rx antenna u_1 and u_2 can be calculated as [5, 6]

$$\rho_{u_1,u_2}^{\mathrm{CTF}} = \frac{cov\{H_{u_1,s}, H_{u_2,s}\}}{\sqrt{var\{H_{u_1,s}\}} \cdot \sqrt{var\{H_{u_2,s}\}}}. \tag{C.12}$$

Inserting (C.3) and (C.4) into (C.12), and using the i.i.d. property of the initial phases of the paths [10], it yields

$$\rho_{u_1,u_2}^{\mathrm{CTF}} = \frac{\beta_{u_1,u_2}}{\sqrt{\beta_{u_1}} \cdot \sqrt{\beta_{u_2}}}, \tag{C.13}$$

where

$$\begin{aligned}\beta_{u_1,u_2} = \sum_{m=1}^{M} \Big\{ & P_m(|F_{s,m}^{\mathrm{V}}|^2 + \kappa_m^{-1}\chi_m^{-1}|F_{s,m}^{\mathrm{H}}|^2) \cdot F_{u_1,m}^{\mathrm{V}} \cdot F_{u_2,m}^{\mathrm{V}*} \\ & + P_m(\kappa_m^{-1}|F_{s,m}^{\mathrm{V}}|^2 + \chi_m^{-1}|F_{s,m}^{\mathrm{H}}|^2) \cdot F_{u_1,m}^{\mathrm{H}} \cdot F_{u_2,m}^{\mathrm{H}*} \Big\},\end{aligned} \tag{C.14a}$$

$$\begin{aligned}\beta_{u} = \sum_{m=1}^{M} \Big\{ & P_m(|F_{s,m}^{\mathrm{V}}|^2 + \kappa_m^{-1}\chi_m^{-1}|F_{s,m}^{\mathrm{H}}|^2) \cdot |F_{u,m}^{\mathrm{V}}|^2 \\ & + P_m(\kappa_m^{-1}|F_{s,m}^{\mathrm{V}}|^2 + \chi_m^{-1}|F_{s,m}^{\mathrm{H}}|^2) \cdot |F_{u,m}^{\mathrm{H}}|^2 \Big\}.\end{aligned} \tag{C.14b}$$

3.2 Antenna Correlation from Angular Power Spectrum

The antenna correlation between two Rx antennas, u_1 and u_2, can also be calculated as [1] (c.f. (C.13))

$$\rho_{u_1,u_2}^{\mathrm{APS}} = \frac{\gamma_{u_1,u_2}}{\sqrt{\gamma_{u_1}} \cdot \sqrt{\gamma_{u_2}}}, \tag{C.15}$$

where

$$\gamma_{u_1,u_2} = \int \Big\{ \eta \cdot p^{\mathrm{V}}(\mathbf{\Omega}^{\mathrm{Rx}}) \cdot F^{\mathrm{V}}_{u_1}(\mathbf{\Omega}^{\mathrm{Rx}}) \cdot F^{\mathrm{V}}_{u_2}(\mathbf{\Omega}^{\mathrm{Rx}})^* + p^{\mathrm{H}}(\mathbf{\Omega}^{\mathrm{Rx}}) \cdot F^{\mathrm{H}}_{u_1}(\mathbf{\Omega}^{\mathrm{Rx}}) \cdot F^{\mathrm{H}}_{u_2}(\mathbf{\Omega}^{\mathrm{Rx}})^* \Big\} \, \mathrm{d}\mathbf{\Omega}^{\mathrm{Rx}}, \tag{C.16a}$$

$$\gamma_{u} = \int \Big\{ \eta \cdot p^{\mathrm{V}}(\mathbf{\Omega}^{\mathrm{Rx}}) \cdot |F^{\mathrm{V}}_{u}(\mathbf{\Omega}^{\mathrm{Rx}})|^2 + p^{\mathrm{H}}(\mathbf{\Omega}^{\mathrm{Rx}}) \cdot |F^{\mathrm{H}}_{u}(\mathbf{\Omega}^{\mathrm{Rx}})|^2 \Big\} \, \mathrm{d}\mathbf{\Omega}^{\mathrm{Rx}}, \tag{C.16b}$$

with $p^{\mathrm{V}}(\mathbf{\Omega}^{\mathrm{Rx}})$ and $p^{\mathrm{H}}(\mathbf{\Omega}^{\mathrm{Rx}})$ being the normalized APS, i.e. $\int p^{\mathrm{V}}(\mathbf{\Omega}^{\mathrm{Rx}}) \, \mathrm{d}\mathbf{\Omega}^{\mathrm{Rx}} = \int p^{\mathrm{H}}(\mathbf{\Omega}^{\mathrm{Rx}}) \, \mathrm{d}\mathbf{\Omega}^{\mathrm{Rx}} = 1$, in the DoA domain for V-pol and H-pol, respectively. The term η is the so-called V/H ratio [5], and is defined as the ratio of the total power of the incident signal of the V-pol over that of the H-pol.

It must be noted that in the literature the V/H ratio is often termed also as XPR depending on the background, which is sometimes confusing to that defined in the GSCM model as described in Subsection2.1. Therefore, additional care shall be taken for those values in practice for calculation.

The normalized APS for both polarizations can be obtained with (C.11) as

$$p^{\mathrm{V}}(\mathbf{\Omega}^{\mathrm{Rx}}) = \frac{P^{\mathrm{V}}(\mathbf{\Omega}^{\mathrm{Rx}})}{P^{\mathrm{V}}_{\mathrm{tot}}}, \tag{C.17a}$$

$$p^{\mathrm{H}}(\mathbf{\Omega}^{\mathrm{Rx}}) = \frac{P^{\mathrm{H}}(\mathbf{\Omega}^{\mathrm{Rx}})}{P^{\mathrm{H}}_{\mathrm{tot}}}, \tag{C.17b}$$

with

$$P^{\mathrm{V}}_{\mathrm{tot}} = \sum_{m=1}^{M} P_m (1 + \kappa_m^{-1} \chi_m^{-1}), \tag{C.18a}$$

$$P^{\mathrm{H}}_{\mathrm{tot}} = \sum_{m=1}^{M} P_m (\kappa_m^{-1} + \chi_m^{-1}), \tag{C.18b}$$

being the total incident power for both polarizations. In addition, the V/H ratio η can be obtained as

$$\eta = \frac{P^{\mathrm{V}}_{\mathrm{tot}}}{P^{\mathrm{H}}_{\mathrm{tot}}}. \tag{C.19}$$

Equation (C.19) also indicates the V/H ratio η can be uniquely determined from the XPR κ_m and CPR χ_m but not vice versa.

Inserting (C.17), (C.18), and (C.19) into (C.16) and with some equation manipulation, we can obtain the antenna correlation $\rho^{\mathrm{APS}}_{u_1,u_2}$ under the same

channel model as for $\rho^{\mathrm{CTF}}_{u_1,u_2}$ as

$$\gamma_{u_1,u_2} = \sum_{m=1}^{M} \Big\{ P_m(1+\kappa_m^{-1}\chi_m^{-1}) \cdot F^{\mathrm{V}}_{u_1,m} \cdot F^{\mathrm{V}*}_{u_2,m} + P_m(\kappa_m^{-1}+\chi_m^{-1}) \cdot F^{\mathrm{H}}_{u_1,m} \cdot F^{\mathrm{H}*}_{u_2,m} \Big\}, \tag{C.20a}$$

$$\gamma_{u} = \sum_{m=1}^{M} \Big\{ P_m(1+\kappa_m^{-1}\chi_m^{-1}) \cdot |F^{\mathrm{V}}_{u,m}|^2 + P_m(\kappa_m^{-1}+\chi_m^{-1}) \cdot |F^{\mathrm{H}}_{u,m}|^2 \Big\}. \tag{C.20b}$$

3.3 Relation Between the Two Antenna Correlation Approaches

By comparing (C.14) and (C.20), we can find that the difference between $\rho^{\mathrm{APS}}_{u_1,u_2}$ and $\rho^{\mathrm{CTF}}_{u_1,u_2}$ is solely caused by the discrepancy of the antenna de-embedding assumption between the two approaches. Since the CTF describes the input-output relation between the Tx antenna ports and the Rx antenna ports, antenna pattern is not de-embedded from the CTF (C.1). Therefore, the effective power spectrum in the DoA domain for the CTF case accounting for the Tx antenna pattern can be alternatively formulated as (c.f. (C.9))

$$\widetilde{\boldsymbol{P}}(\boldsymbol{\Omega}^{\mathrm{Rx}}) = \int \begin{bmatrix} |F^{\mathrm{V}}_s(\boldsymbol{\Omega}^{\mathrm{Tx}})|^2 \\ |F^{\mathrm{H}}_s(\boldsymbol{\Omega}^{\mathrm{Tx}})|^2 \end{bmatrix}^{\mathrm{T}} \boldsymbol{P}(\boldsymbol{\Omega}^{\mathrm{Tx}}, \boldsymbol{\Omega}^{\mathrm{Rx}})\, \mathrm{d}\boldsymbol{\Omega}^{\mathrm{Tx}}. \tag{C.21}$$

If we derive the antenna correlation $\rho^{\mathrm{APS}}_{u_1,u_2}$ with respect to $\widetilde{\boldsymbol{P}}(\boldsymbol{\Omega}^{\mathrm{Rx}})$ following the same way in Subsection 3.2, and denote that as $\widetilde{\rho}^{\mathrm{APS}}_{u_1,u_2}$, it is very straightforward to find

$$\widetilde{\rho}^{\mathrm{APS}}_{u_1,u_2} = \rho^{\mathrm{CTF}}_{u_1,u_2}. \tag{C.22}$$

Alternatively, we can also consider $\rho^{\mathrm{APS}}_{u_1,u_2}$ as a special case of $\rho^{\mathrm{CTF}}_{u_1,u_2}$ with $|F^{\mathrm{V}}_s(\boldsymbol{\Omega}^{\mathrm{Tx}})|^2 = |F^{\mathrm{H}}_s(\boldsymbol{\Omega}^{\mathrm{Tx}})|^2 = 1$. Given clarification on the antenna de-embedding assumption for both approaches, the discrepancy can be resolved resulting in the same antenna correlation results.

Another interesting effect of the discrepancy is that since the effective APS $\widetilde{\boldsymbol{P}}(\boldsymbol{\Omega}^{\mathrm{Rx}})$ is ruled by both the joint $\boldsymbol{P}(\boldsymbol{\Omega}^{\mathrm{Tx}}, \boldsymbol{\Omega}^{\mathrm{Rx}})$ and the Tx antenna pattern as shown in (C.21), the resulting $\rho^{\mathrm{CTF}}_{u_1,u_2}$ becomes dependent on the joint $\boldsymbol{P}(\boldsymbol{\Omega}^{\mathrm{Tx}}, \boldsymbol{\Omega}^{\mathrm{Rx}})$ instead of just the marginal $\boldsymbol{P}(\boldsymbol{\Omega}^{\mathrm{Rx}})$ as for $\rho^{\mathrm{APS}}_{u_1,u_2}$. An intuitive example of this effect can be made by changing the pairing order between the DoD $\boldsymbol{\Omega}^{\mathrm{Tx}}_m$ and the DoA $\boldsymbol{\Omega}^{\mathrm{Rx}}_{m'}$ with $m, m' \in [1, M]$ in the channel according to [7]. Different pairing orders result in different joint $\boldsymbol{P}(\boldsymbol{\Omega}^{\mathrm{Tx}}, \boldsymbol{\Omega}^{\mathrm{Rx}})$, while the corresponding marginal $\boldsymbol{P}(\boldsymbol{\Omega}^{\mathrm{Rx}})$ always remains the same. As a result, $\rho^{\mathrm{APS}}_{u_1,u_2}$ remains unchanged, whereas $\rho^{\mathrm{CTF}}_{u_1,u_2}$ changes with different joint $\boldsymbol{P}(\boldsymbol{\Omega}^{\mathrm{Tx}}, \boldsymbol{\Omega}^{\mathrm{Rx}})$

filtered by the Tx the spatial selectivity. Those findings show the effect of the Tx spatial selectivity on the resulting Rx antenna correlation with the CTF approach.

4 Numerical Examples

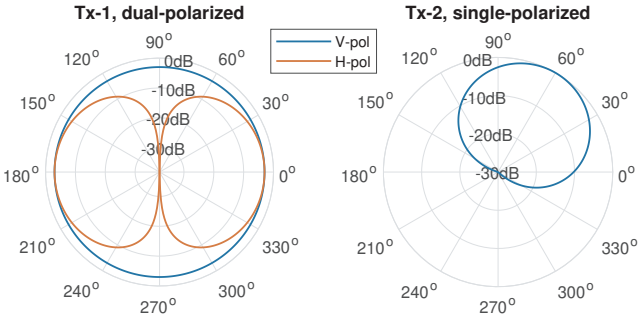

Fig. C.1: The azimuth antenna pattern of (Tx-1) the 45° slanted ideal dipole [5], and (Tx-2) the V-pol dipole with 65° HPBW and boresight at 60° [7].

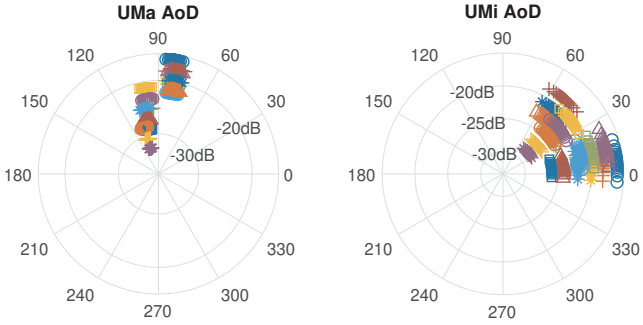

Fig. C.2: The APS in the azimuth angle of departure (AoD) domain for (left) the SCME UMa scenario and (right) the SCME UMi scenario [5]. Colors and markers differ the 18 clusters and each cluster are modelled with 20 subpaths (denoted as scatterers).

In this section, we take the SCME Urban Macro-cell (UMa) and Urban Micro-cell (UMi) channel model [5] as the reference channels, and three configurations for the Tx antennas, to demonstrate the difference of the two antenna correlation approaches. Tx config-0 (Tx-0) is the case where the Tx antennas are de-embedded; Tx config-1 (Tx-1) is a 45° slanted ideal dipole with isotropic gain [5]; and Tx config-2 (Tx-2) is a V-pol dipole with 65° half-power beam width and boresight at 60° [7]. The corresponding Tx antenna pattern and APS in the azimuth plane are shown in Fig. C.1 and Fig. C.2, respectively.

Table C.1: The Effect of Tx Antenna Pattern on the Resulting V/H Ratio.

	SCME UMa			SCME UMi		
Tx Configs	κ_m	χ_m	η	κ_m	χ_m	η
Tx-0	9 dB	0 dB	0 dB	9 dB	0 dB	0 dB
Tx-1	9 dB	0 dB	8.14 dB	9 dB	0 dB	0.74 dB
Tx-2	9 dB	0 dB	9 dB	9 dB	0 dB	9 dB

The V/H ratio η is calculated from $\widetilde{\boldsymbol{P}}(\boldsymbol{\Omega}^{\mathrm{Rx}})$ with the three Tx configurations. The resulting values are shown in Table C.1 for both the UMa and UMi scenarios with the input parameters XPR $\kappa_m = 9$ dB and CPR $\chi_m = 0$ dB taken from the SCME model. The difference between the values of η from different Tx configurations is significant. More specifically, the large V/H ratio for Tx-1 under the UMa scenario is caused by the polarization discrimination around 90° between the V-pol and H-pol Tx antenna pattern, where the AoDs of the paths happen to be located. When the Tx antenna is only V-pol as for Tx-2, the V/H ratio equals the XPR.

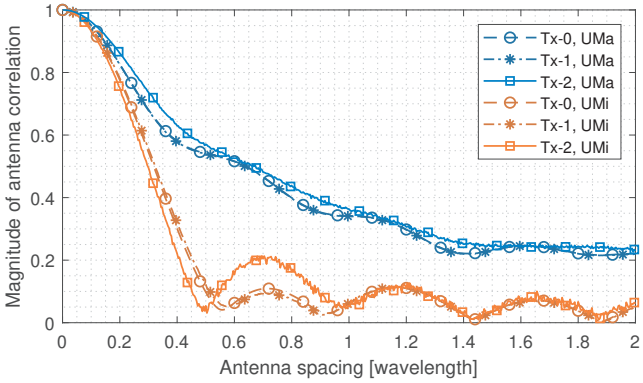

Fig. C.3: The magnitude of the antenna correlation $\rho^{\mathrm{CTF}}_{u_1,u_2}$ against antenna spacing with the three Tx configurations under the UMa and the UMi channel. Note that $\rho^{\mathrm{CTF}}_{u_1,u_2}$ with Tx-0 is equivalent to $\rho^{\mathrm{APS}}_{u_1,u_2}$.

Further, the antenna correlation is calculated with isotropic antennas on the Rx side and shown in Fig. C.3. The antenna spacing between the Rx antennas is swept from 0 to 2λ (wavelength), and the broadside of the two Rx antennas is aligned to 0° in the azimuth plane. The AoDs and the AoAs of the 20 subpaths of each cluster are first paired up randomly, and then the resulting pairing order is fixed throughout the simulation to have a fixed joint AoD-AoA power spectrum for a fair comparison of $\rho^{\mathrm{CTF}}_{u_1,u_2}$ with different Tx configurations. Note that $\rho^{\mathrm{CTF}}_{u_1,u_2}$ with Tx-0 is equivalent to $\rho^{\mathrm{APS}}_{u_1,u_2}$ as discussed

in Subsection 3.3.

We can see that difference between $\rho^{\mathrm{CTF}}_{u_1,u_2}$ and $\rho^{\mathrm{APS}}_{u_1,u_2}$ is more significant with Tx-2 than with Tx-1 for both scenarios. The reason is that the directional antenna pattern of Tx-2 alters $\widetilde{\boldsymbol{P}}(\boldsymbol{\Omega}^{\mathrm{Rx}})$ more severely than Tx-1 does. Moreover, the difference is more significant under the UMi scenario than under the UMa scenario for the same Tx configuration. This is because the larger AoD spread under the UMi scenario introduces more variation from the Tx antenna pattern to $\widetilde{\boldsymbol{P}}(\boldsymbol{\Omega}^{\mathrm{Rx}})$ compared to the UMa scenario. Therefore, we can expect that a more noticeable difference between $\rho^{\mathrm{CTF}}_{u_1,u_2}$ and $\rho^{\mathrm{APS}}_{u_1,u_2}$ may occur if either the AoD spread of a given channel is larger or the Tx antenna pattern is more directional.

5 Conclusion

In this paper, we derived the analytic forms for the antenna correlation based on the CTF and the APS, respectively. The relation between the antenna correlation from the two approaches is described with the spread function. It is shown explicitly in the derivation that the difference between them is caused by the antenna de-embedding assumption made for the APS, which is not generally assumed for the CTF. It is also pointed out that the two antenna correlation approaches can be equivalent if the same assumption is made for the CTF.

Antenna correlation under the two approaches and V/H ratio are evaluated with the SCME UMa and UMi channel model as an example, which numerically shows the effect of the spatial selectivity of the Tx antennas on the results. The APS approach is generally adopted in the antenna community to calculate antenna correlation, which is a key measure to design MIMO antennas, and our theoretical analysis and numerical simulation show that ignoring Tx antenna pattern might lead to inaccurate Rx antenna correlation calculation with this approach.

References

[1] C. A. Balanis, *Antenna Theory: Analysis and Design*. John Wiley & Sons, 2005.

[2] R. Vaughan and J. B. Andersen, *Channels , Propagation and Antennas for Mobile Communications*. The Institution of Electrical Engineers, 2003.

[3] L. Schumacher, K. I. Pedersen, and P. E. Mogensen, "From antenna spacings to theoretical capacities - Guidelines for simulating MIMO systems," *IEEE International Symposium on Personal, Indoor and Mobile Radio Communications, PIMRC*, vol. 2, pp. 587–592, 2002.

[4] I. Szini, B. Yanakiev, and G. F. Pedersen, "MIMO reference antennas performance in anisotropic channel environments," *IEEE Transactions on Antennas and Propagation*, vol. 62, no. 6, pp. 3270–3280, 2014.

[5] 3GPP, "Verification of radiated multi-antenna reception performance of User Equipment (UE)," Tech. Rep. 3GPP TR 37.977 V15.0.0, 2018.

[6] CTIA, "Test Plan for 2x2 Downlink MIMO and Transmit Diversity Over-the-Air Performance," Tech. Rep. Version 1.1.1, 2017.

[7] 3GPP, "Study on channel model for frequencies from 0.5 to 100 GHz," Tech. Rep. 3GPP TR 38.901 V14.0.0, 2017. [Online]. Available: http://www.etsi.org/standards-search

[8] WINNER, "WINNER II Channel Models: Part I Channel Models," Tech. Rep. D1.1.2 V1.2, 2007. [Online]. Available: http://projects.celtic-initiative.org/WINNER+/WINNER2-Deliverables/D4.6.1.pdf

[9] B. H. Fleury, "First- and second-order characterization of direction dispersion and space selectivity in the radio channel," *IEEE Transactions on Information Theory*, vol. 46, no. 6, pp. 2027–2044, 2000.

[10] P. Bello, "Characterization of Randomly Time-Variant Linear Channels," *IEEE Transactions on Communications Systems*, vol. 11, no. 4, pp. 360–393, 1963. [Online]. Available: http://ieeexplore.ieee.org/xpls/abs{_}all.jsp?arnumber=1088793{&}tag=1

Paper D

On Channel Emulation Methods in Multi-Probe Anechoic Chamber Setups for Over-The-Air Testing

Yilin Ji, Wei Fan, Gert Frølund Pedersen, and Xingfeng Wu

The paper has been published in the
IEEE Transactions on Vehicular Technology Vol. 67, No. 8, pp. 6740–6751, 2018.

The layout has been revised.

Abstract

Multiple-input multiple-output (MIMO) over-the-air (OTA) testing gives a way to evaluate the radio performance of MIMO-capable devices under realistic propagation channels as an alternative to expensive and uncontrollable drive testing. In this paper, we review two major channel emulation methods for MIMO OTA testing under the multi-probe anechoic chamber (MPAC) setup, i.e. the prefaded signals synthesis (PFS) and the plane wave synthesis (PWS). The target channel model for emulation is the geometry-based stochastic channel model (GSCM). The signal models for both channel emulation methods for the whole link from the transmitter (Tx) side to the receiver (Rx) side are given. The comparison analysis gives some new insights into the two channel emulation methods. The analytic expression of the joint space-time correlation function is derived for both methods in comparison to that of the target channel. It shows the cluster-wise channel emulated by the PFS method is Kronecker structured, which is different from the general definition of GSCMs. In contrast, the channel emulated with the PWS method is consistent with GSCMs. Moreover, the emulation accuracy for the two methods are compared under different target channel settings, i.e. different cluster angular spreads. The simulation results demonstrate the advantage of the PWS method over the PFS method, especially when cluster angular spreads are small.

1 Introduction

Multiple-input multiple-output (MIMO) over-the-air (OTA) testing [1] currently plays an important role in evaluating the radio performance of any MIMO-capable device in different development stages, e.g. early-stage prototyping and mid-term refinement, before final massive roll-out. It helps researchers to reveal the potential flaws and non-idealities of the products during the design and manufacturing phase. The conventional way to conduct MIMO performance testing is called MIMO conducted testing. In conducted testing, the shell of the device-under-test (DUT) needs to be opened, and antenna ports on the DUT need to be reserved for cable connection. However, OTA testing does not suffer from these limitations. Therefore, it is standardized that the radiated performance testing of MIMO-capable devices must be performed over-the-air [1].

In general, the implementation of MIMO OTA testing can be divided into three main categories, i.e. the radiated two-stage (RTS) methods [2, 3], the reverberation chamber (RC) based methods [4, 5], and the multi-probe anechoic chamber (MPAC) based methods [6–9]. The RTS method evolves from the conducted two-stage method [10] where the physical cable connection between the channel emulator (CE) output ports and the DUT antenna ports is approached over-the-air in an anechoic chamber. By introducing a so-called

calibration matrix in the CE, the product of the calibration matrix and the transfer matrix between the CE output ports and the DUT antenna ports yields (or approximates) an identity matrix. In other words, the signals received at the DUT antenna ports are approximately the same as from the conducted two-stage method as if cables were used. Therefore, this method is also called wireless cable method [3]. Due to the use of CEs, arbitrary channel models can be implemented with the RTS method. However, the antenna array field pattern needs to be measured in the first stage with the internal receivers of the DUT and synthesized in the CE in the second stage, which means the DUT antenna response is not inherently included during the testing. Hence, the RTS method is not suitable for DUTs with reconfigurable or adaptive antenna patterns [3]. The second category is the RC based method, which generates isotropic spatial channels with Rayleigh fading by rotating mechanical stirrers and DUT in the reverberation chamber (metallic cavity). Unlike the RTS method, the DUT antenna pattern is directly included in the testing. However, the drawback of the RC based method is its limited control on the reproduced channels. The third category is the MPAC based method, which is standardized in CTIA [11] for its capability of reproducing standard channel models, i.e. geometry-based stochastic channel models (GSCMs), such as 3GPP SCM [12], SCME [13], and WINNER II model [14].

Two channel emulation methods, which are shown later in the paper, are usually adopted with MPAC setups, namely the prefaded signals synthesis (PFS) [7, 15], and the plane wave synthesis (PWS) [6–9]. The verification of both methods is usually done with channel characteristics in different domains, e.g. spatial correlation function (SCF) on the transmitter (Tx) side, SCF on the receiver (Rx) side, temporal correlation function (TCF), power delay profile, and cross-polarization ratio (XPR) [7, 16]. However, the verification in joint domain, e.g. the SCF in joint Tx-Rx space domain, is rarely mentioned. Moreover, the PFS and the PWS method are usually considered to be equally capable of emulating GSCMs [7, 17]. In this paper, the signal models for the emulated channels with the PFS and the PWS method are given. The space-time correlation function (STCF) [18–21] is derived for both methods in joint Tx space, Rx space, and time domain. Comparisons are made to the STCF of the target channel model for the first time in the literature. The commonly-believed equivalence in emulation accuracy for the two methods is evaluated. The simulation in SCF on the Rx side shows that this is only valid when the cluster angular spread of the target channel is large.

The contribution of this paper lies in the following aspects:

- The signal models of the emulated channels for the whole link from the Tx side to the Rx side are given for both the PFS and the PWS method.
- The STCF in the joint domain, i.e. the spatial domain on the Tx side, the spatial domain on the Rx side, and the time domain, is derived for

both methods, which reveals the Kronecker structure of the cluster-wise emulated channel with the PFS method. This feature is important, yet not known for the PFS method.

- The emulation accuracy of the two methods is compared in terms of the SCF of the emulated channels on the Rx side under different target channel settings, i.e. cluster angular spreads. It is demonstrated that the commonly-believed equivalence in channel emulation capabilities is only valid when the cluster spread is large.

The rest of the paper is organized as follows: In Section 2, the principles of the PFS and the PWS method are reviewed. In Section 3, the STCF of the emulated channel is derived for both methods, and the difference to that of the target channel is discussed. In Section 4, the emulation accuracy of the two methods are compared under different target channel settings. Section 5 concludes the paper.

The notation used in this paper is as follows: $(\cdot)^{\mathrm{T}}$ denotes the transpose operator, $(\cdot)^*$ the complex conjugate operator, $\|\cdot\|$ the Euclidean norm, $\langle\cdot,\cdot\rangle$ the inner product operator, and $\mathbb{E}\{\cdot\}$ the expectation operator.

2 Principle of Channel Emulation Methods Under MPAC Setup

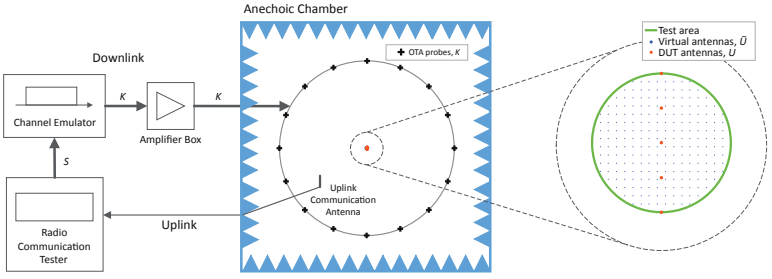

Fig. D.1: The diagram of MIMO OTA testing with an MPAC setup [16]. Note the DUT antennas are illustrated as a ULA, but they can be of arbitrary structures in practice.

The diagram of MIMO OTA testing with the MPAC setup is shown in Fig. D.1. The whole system consists of a radio communication tester, a CE, a power amplifier box, and a number of OTA probes located inside an anechoic chamber. For the downlink, test signals are generated from a radio communication tester, which mimics the behaviour of a Tx equipped with S antennas. The test signals are transmitted to the CE via cables, and further convolved with the channel in the CE, which is generated according to the

standard channel models. The output signals from the CE are fed to K OTA probes inside the anechoic chamber after being power amplified. The target spatial profiles on the Rx side, i.e. the DUT side, are generated in the so-called test area over-the-air with the channel emulation methods. The DUT with U antennas is placed in the test area to perform the testing. Note the DUT antennas are illustrated as a uniform linear array (ULA) in Fig. D.1, but they can be of arbitrary structures in practice. The focus of the testing is on the downlink, and usually only one communication antenna is placed in the anechoic chamber for uplink communication.

The goal of the channel emulation methods is to reproduce the spatial profiles of the target channel on the Rx side in the test area with the MPAC setup. The PFS method and the PWS method achieve the objective in two different ways. In this section, we introduce the target channel models, i.e. the GSCMs, and the two channel emulation methods, i.e. the PFS and the PWS method.

2.1 Target Channel Models

For a MIMO system with S antenna elements on the Tx array and U antenna elements on the Rx array, the time-variant channel transfer function $h_{u,s}(t,f)$ between the sth Tx element and the uth Rx element can be expressed as [12]

$$h_{u,s}(t,f) = \sum_{n=1}^{N} h_{u,s,n}(t,f), \tag{D.1}$$

where N is the number of clusters, t denotes the time, and f the frequency. The contribution of the nth cluster can be further expressed as

$$\begin{aligned} h_{u,s,n}(t,f) = \sqrt{\frac{P_n}{M}} \sum_{m=1}^{M} \begin{bmatrix} F^V_{s,\mathrm{Tx}}(\varphi_{n,m}) \\ F^H_{s,\mathrm{Tx}}(\varphi_{n,m}) \end{bmatrix}^{\mathrm{T}} \mathbf{A} \begin{bmatrix} F^V_{u,\mathrm{Rx}}(\phi_{n,m}) \\ F^H_{u,\mathrm{Rx}}(\phi_{n,m}) \end{bmatrix} \\ \cdot \exp(j2\pi\vartheta_{n,m}t) \exp(-j2\pi f\tau_n), \end{aligned} \tag{D.2}$$

where P_n and τ_n are the power and the delay of the nth cluster, respectively. M is the number of subpaths for each cluster, $F^V_{s,\mathrm{Tx}}$ and $F^H_{s,\mathrm{Tx}}$ are the antenna field patterns of the sth Tx antenna for vertical and horizontal polarization, respectively. Similarly, $F^V_{u,\mathrm{Rx}}$ and $F^H_{u,\mathrm{Rx}}$ are the antenna field patterns of the uth Rx antenna for vertical and horizontal polarization, respectively. $\varphi_{n,m}$, $\phi_{n,m}$, and $\vartheta_{n,m}$ are the angle of departure (AoD), angle of arrival (AoA), and Doppler frequency of the mth subpath of the nth cluster, respectively. Note that the antenna field pattern is defined with a common phase center over the antenna array, so the phase differences corresponding to the array geometry

are inherently included. **A** is the polarization matrix, and can be written as

$$\mathbf{A} = \begin{bmatrix} \exp\left(j\Phi_{n,m}^{VV}\right) & \sqrt{\kappa_{n,m}^{-1}}\exp\left(j\Phi_{n,m}^{VH}\right) \\ \sqrt{\kappa_{n,m}^{-1}}\exp\left(j\Phi_{n,m}^{HV}\right) & \exp\left(j\Phi_{n,m}^{HH}\right) \end{bmatrix} \tag{D.3}$$

where $\Phi_{n,m}^{VV}$, $\Phi_{n,m}^{VH}$, $\Phi_{n,m}^{HV}$, and $\Phi_{n,m}^{HH}$ are independent and identically distributed (i.i.d.) random variables which are uniformly distributed over $[0, 2\pi]$. $\kappa_{n,m}$ is the XPR of the mth subpath of the nth cluster.

For MPAC based methods, the key problem to solve is to reproduce the target spatial profile on the Rx side over-the-air, since the other channel properties, e.g. spatial profile on the Tx side, Doppler spectrum, power delay profile, and XPR, can be perfectly reproduced in the CE [16, 22]. The dual polarization control is realized by using OTA probes with two co-located orthogonally polarized elements with independent feeds. For simplicity, we only discuss the vertical polarization case hereafter. In the single polarization case, the polarization matrix **A** diminishes to a scalar, and (D.2) is simplified to

$$\begin{aligned} h_{u,s,n}(t,f) = \sqrt{\frac{P_n}{M}} \sum_{m=1}^{M} & F_s^{\mathrm{Tx}}(\varphi_{n,m}) F_u^{\mathrm{Rx}}(\phi_{n,m}) \\ & \cdot \exp(j2\pi\vartheta_{n,m}t + j\Phi_{n,m}) \cdot \exp(-j2\pi f\tau_n), \end{aligned} \tag{D.4}$$

where F_s^{Tx} and F_u^{Rx} are the vertically polarized antenna field pattern for the sth Tx antenna and uth Rx antenna, respectively. $\Phi_{n,m}$ is the i.i.d. random initial phase of the mth subpath of the nth cluster. We further restrict our discussion to two-dimensional (2D) channel models, which means the OTA probes and the test area are in the same plane, i.e. the azimuth plane. Consequently, AoDs and AoAs correspond to azimuth angles.

2.2 Prefaded Signals Synthesis Method

For link level simulations, channels are generated based on drops, within which channel parameters are fixed and motions are only virtual [14]. Due to the wide-sense stationary uncorrelated scattering (WSSUS) assumption [18–20] for every drop, the channel can be fully characterized with its second-order statistics, i.e. the correlation functions. The PFS method generates the channel, whose correlation functions approximate those of the target channel cluster-wise.

For an MPAC setup equipped with K OTA probes, the transfer function emulated with the PFS method from the sth Tx antenna to the kth OTA probe

for the nth cluster can be expressed as

$$\hat{h}^{\mathrm{PFS}}_{k,s,n}(t,f) = \sqrt{\frac{P_n}{M}} \sum_{m=1}^{M} F^{\mathrm{Tx}}_{s}(\varphi_{n,m}) \sqrt{g_{n,k}} \cdot \exp(j2\pi\vartheta_{n,m}t + j\Phi_{n,m,k}) \cdot \exp(-j2\pi f\tau_n), \tag{D.5}$$

where $\Phi_{n,m,k}$ is the i.i.d. random initial phase of the mth subpath of the nth cluster for the kth OTA probe. $g_{n,k}$ is the power weight applied on the kth OTA probe for the nth cluster with $\sum_{k=1}^{K} g_{n,k} = 1$.

In order to observe the emulated channel in the test area, the test area is sampled with $\tilde{U}$ virtual isotropic antennas. The emulated channel observed at the $\tilde{u}$th virtual antenna (VA) from the sth Tx antenna for the nth cluster can be calculated as the sum of the contribution from all K OTA probes as

$$\begin{aligned}\hat{h}^{\mathrm{PFS}}_{\tilde{u},s,n}(t,f) &= \sum_{k=1}^{K} \hat{h}^{\mathrm{PFS}}_{k,s,n}(t,f) \cdot F^{\mathrm{VA}}_{\tilde{u}}(\phi^{\mathrm{OTA}}_{k}) \\ &= \sqrt{\frac{P_n}{M}} \sum_{k=1}^{K} \sum_{m=1}^{M} F^{\mathrm{Tx}}_{s}(\varphi_{n,m}) F^{\mathrm{VA}}_{\tilde{u}}(\phi^{\mathrm{OTA}}_{k}) \sqrt{g_{n,k}} \\ &\quad \cdot \exp(j2\pi\vartheta_{n,m}t + j\Phi_{n,m,k}) \cdot \exp(-j2\pi f\tau_n),\end{aligned} \tag{D.6}$$

where $F^{\mathrm{VA}}_{\tilde{u}}(\phi^{\mathrm{OTA}}_{k})$ is the antenna field pattern of the virtual antenna $\tilde{u}$ with $\|F^{\mathrm{VA}}_{\tilde{u}}\| = 1$. $\phi^{\mathrm{OTA}}_{k} = 2\pi(k-1)/K$ is the angle where the kth OTA probe is located with respect to the center of the test area. Note that the antenna patterns of the OTA probes and the power loss due to the free-space propagation from the OTA probes to the test area are omitted in (D.6) because the transmitting power of each OTA probe is calibrated to the same level with a calibration antenna in the center of the test area. Moreover, since the OTA probes are placed in the far field of the test area, the plane wave assumption holds across the test area with respect to each OTA probe. Also, the power variation within the test area from each OTA probe is negligible.

The spatial profile of each cluster of the target channel on the Rx side is emulated by assigning a proper power weight $g_{n,k}$ to the kth OTA probe for the nth cluster so that the emulated spatial profile in the test area approaches the target one. The spatial correlation of the nth cluster of the target channel for an arbitrary virtual antenna pair $(\tilde{u}_1, \tilde{u}_2)$ with $\tilde{u}_1 \in [1, \tilde{U}]$ and $\tilde{u}_2 \in [1, \tilde{U}]$ can be calculated as

$$\begin{aligned}\rho_{\tilde{u}_1,\tilde{u}_2} &= \frac{1}{\beta_0} \cdot \mathbb{E}\left\{h_{\tilde{u}_1,s,n}(t,f) \cdot h_{\tilde{u}_2,s,n}(t,f)^*\right\} \\ &= \frac{1}{M} \sum_{m=1}^{M} F^{\mathrm{VA}}_{\tilde{u}_1}(\phi_{n,m}) F^{\mathrm{VA}}_{\tilde{u}_2}(\phi_{n,m})^*,\end{aligned} \tag{D.7}$$

where $h_{\tilde{u},s,n}(t,f)$ is calculated from (D.4) with the virtual antenna $\tilde{u}$ as the Rx antenna. $\beta_0 = P_n$ is the normalization factor to force $\rho_{\tilde{u}_1,\tilde{u}_2} = 1$ when $\tilde{u}_1 = \tilde{u}_2$. The detailed derivation for (D.7) is given in Appendix A. The corresponding spatial correlation of the emulated channel can be derived similarly as for the target channel as

$$\begin{aligned}\hat{\rho}_{\tilde{u}_1,\tilde{u}_2} &= \frac{1}{\hat{\beta}_0} \cdot \mathbb{E}\left\{\hat{h}^{\mathrm{PFS}}_{\tilde{u}_1,s,n}(t,f) \cdot \hat{h}^{\mathrm{PFS}}_{\tilde{u}_2,s,n}(t,f)^*\right\} \\ &= \sum_{k=1}^{K} g_{n,k} F^{\mathrm{VA}}_{\tilde{u}_1}(\phi^{\mathrm{OTA}}_k) F^{\mathrm{VA}}_{\tilde{u}_2}(\phi^{\mathrm{OTA}}_k)^*, \end{aligned} \tag{D.8}$$

where $\hat{\beta}_0 = P_n$ is the normalization factor to force $\hat{\rho}_{\tilde{u}_1,\tilde{u}_2} = 1$ when $\tilde{u}_1 = \tilde{u}_2$. The detailed derivation for (D.8) is given in Appendix B.

The power weight vector $\boldsymbol{g}_n = [g_{n,1}, ..., g_{n,K}]$ is obtained by solving the optimization problem

$$\arg\min_{\boldsymbol{g}_n} \|\rho_{\tilde{u}_1,\tilde{u}_2} - \hat{\rho}_{\tilde{u}_1,\tilde{u}_2}(\boldsymbol{g}_n)\|^2, \tag{D.9}$$

for all combinations of $(\tilde{u}_1, \tilde{u}_2)$ pairs. Equation (D.9) is convex and can be solved efficiently [23]. Finally, the emulated channel for the nth cluster from the sth Tx antenna to the uth DUT antenna can be written as

$$\begin{aligned}\hat{h}^{\mathrm{PFS}}_{u,s,n}(t,f) = \sqrt{\frac{P_n}{M}} \sum_{k=1}^{K} \sum_{m=1}^{M} F^{\mathrm{Tx}}_s(\varphi_{n,m}) F^{\mathrm{Rx}}_u(\phi^{\mathrm{OTA}}_k) \sqrt{g_{n,k}} \\ \cdot \exp(j2\pi\vartheta_{n,m}t + j\Phi_{n,m,k}) \cdot \exp(-j2\pi f\tau_n). \end{aligned} \tag{D.10}$$

2.3 Plane Wave Synthesis Method

In comparison to the PFS method, where the target channel model is emulated cluster-wise, the PWS method is capable of reproducing each subpath within clusters. For the PWS method, the channel transfer function from the sth Tx antenna to the kth OTA probe for the mth subpath of the nth cluster can be written as [7]

$$\begin{aligned}\hat{h}^{\mathrm{PWS}}_{k,s,n,m}(t,f) = \sqrt{\frac{P_n}{M}} F^{\mathrm{Tx}}_s(\varphi_{n,m}) \cdot w_{n,m,k} \\ \cdot \exp(j2\pi\vartheta_{n,m}t + j\Phi_{n,m}) \cdot \exp(-j2\pi f\tau_n), \end{aligned} \tag{D.11}$$

where $w_{n,m,k}$ is the complex weight added on the kth OTA probe for the mth subpath of the nth cluster. Note that unlike the PFS method where real-valued power weights are applied, complex-valued weights are used in the PWS method. Again, virtual antennas are introduced in the test area to

observe the emulated channel. The emulated channel observed on the virtual antenna $\tilde{u}$ can be calculated as the sum of the contribution from all K OTA probes as

$$\begin{aligned}\hat{h}^{\mathrm{PWS}}_{\tilde{u},s,n,m}(t,f) &= \sum_{k=1}^{K} \hat{h}^{\mathrm{PWS}}_{k,s,n,m}(t,f) \cdot F^{\mathrm{VA}}_{\tilde{u}}(\phi^{\mathrm{OTA}}_{k}) \\ &= \sqrt{\frac{P_n}{M}} \sum_{k=1}^{K} F^{\mathrm{Tx}}_{s}(\varphi_{n,m}) F^{\mathrm{VA}}_{\tilde{u}}(\phi^{\mathrm{OTA}}_{k}) \cdot w_{n,m,k} \\ &\quad \cdot \exp(j2\pi\vartheta_{n,m}t + j\Phi_{n,m}) \cdot \exp(-j2\pi f\tau_n). \end{aligned} \tag{D.12}$$

Since the array response of a single plane wave from the target AoA $\phi_{n,m}$ on the $\tilde{u}$th virtual antenna is $F^{\mathrm{VA}}_{\tilde{u}}(\phi_{n,m})$, the complex weight vector $\boldsymbol{w}_{n,m} = [w_{n,m,1}, ..., w_{n,m,K}]$ is calculated by

$$\arg\min_{\boldsymbol{w}_{n,m}} \sum_{\tilde{u}=1}^{\tilde{U}} \left\| \sum_{k=1}^{K} F^{\mathrm{VA}}_{\tilde{u}}(\phi^{\mathrm{OTA}}_{k}) \cdot w_{n,m,k} - F^{\mathrm{VA}}_{\tilde{u}}(\phi_{n,m}) \right\|^2 . \tag{D.13}$$

Equation (D.13) can be solved with the least squares method. Finally, the emulated channel for the mth subpath of the nth cluster from the sth Tx antenna to the uth DUT antenna with the PWS method results in

$$\begin{aligned}\hat{h}^{\mathrm{PWS}}_{u,s,n,m}(t,f) &= \sqrt{\frac{P_n}{M}} \sum_{k=1}^{K} F^{\mathrm{Tx}}_{s}(\varphi_{n,m}) F^{\mathrm{Rx}}_{u}(\phi^{\mathrm{OTA}}_{k}) \cdot w_{n,m,k} \\ &\quad \cdot \exp(j2\pi\vartheta_{n,m}t + j\Phi_{n,m}) \cdot \exp(-j2\pi f\tau_n). \end{aligned} \tag{D.14}$$

Using channel linearity, we can further obtain the contribution of the nth cluster of the emulated channel from the sth Tx antenna to the uth DUT antenna with the PWS method as

$$\begin{aligned}\hat{h}^{\mathrm{PWS}}_{u,s,n}(t,f) &= \sqrt{\frac{P_n}{M}} \sum_{m=1}^{M} \sum_{k=1}^{K} F^{\mathrm{Tx}}_{s}(\varphi_{n,m}) F^{\mathrm{Rx}}_{u}(\phi^{\mathrm{OTA}}_{k}) \cdot w_{n,m,k} \\ &\quad \cdot \exp(j2\pi\vartheta_{n,m}t + j\Phi_{n,m}) \cdot \exp(-j2\pi f\tau_n). \end{aligned} \tag{D.15}$$

Note that since the PWS method utilizes complex weights on OTA probes for each subpath, both power and phase calibration are needed before testing, which is more demanding than the PFS method in terms of calibration complexity. It was shown in [24] that both power and phase calibration can be achieved at high accuracy for traditional user equipment (UE) OTA testing. However, for the upcoming fifth-generation (5G) communication systems [25–28], the phase calibration could be difficult to achieve for base station (BS) OTA testing due to the non-linearity of radio frequency (RF) components, e.g. switches and power amplifiers, at high frequency band, and

the increased number of OTA probes. Nonetheless, the hardware resources required for the PFS and the PWS method are identical for testing the same DUT.

3 Space-Time Correlation Function Analysis

In this section, we derive the cluster-wise STCF of the emulated channels for the PFS and the PWS method in comparison to that of the target channel model. It is straightforward to extend the derived cluster-wise STCF for the whole channel with multiple clusters due to channel linearity. In order to focus on the channel properties, both the Tx and the Rx antennas are assumed to be isotropic, i.e. $\|F_s^{\mathrm{Tx}}\| = \|F_u^{\mathrm{Rx}}\| = 1$. We further assume the target channel can be perfectly emulated by the PFS and the PWS method in the test area. There exists a power weight vector $\boldsymbol{g}_n$ with $n \in [1, N]$ for the PFS method that yields

$$\hat{\rho}_{u_1,u_2} = \rho_{u_1,u_2}, \tag{D.16}$$

for all (u_1, u_2) DUT antenna pairs with $u_1 \in [1, U]$ and $u_2 \in [1, U]$. Similarly, there exists a complex weight vector $\boldsymbol{w}_{n,m}$ with $n \in [1, N]$ and $m \in [1, M]$ for the PWS method that yields

$$\sum_{k=1}^{K} F_u^{\mathrm{Rx}}(\phi_k^{\mathrm{OTA}}) \cdot w_{n,m,k} = F_u^{\mathrm{Rx}}(\phi_{n,m}), \tag{D.17}$$

for all U DUT antennas. This assumption can be approximately achieved when the number of OTA probes is sufficient to support the desired test area size with respect to an acceptable emulation error, e.g. within 0.2 in deviation from the target SCF [7].

3.1 The STCF for the Target Channel Model

Using the property of the i.i.d. random initial phase $\Phi_{n,m}$ in (D.4), the STCF for the nth cluster of the target channel can be derived as

$$\begin{aligned} R(u_1, s_1, t_1; u_2, s_2, t_2) &= \frac{1}{\beta_0} \cdot \mathbb{E}\left\{h_{u_1,s_1,n}(t_1, f) \cdot h_{u_2,s_2,n}(t_2, f)^*\right\} \\ &= \frac{1}{M} \sum_{m=1}^{M} F_{s_1}^{\mathrm{Tx}}(\varphi_{n,m}) F_{s_2}^{\mathrm{Tx}}(\varphi_{n,m})^* F_{u_1}^{\mathrm{Rx}}(\phi_{n,m}) \\ &\quad \cdot F_{u_2}^{\mathrm{Rx}}(\phi_{n,m})^* \exp(j2\pi\vartheta_{n,m}t_1) \exp(j2\pi\vartheta_{n,m}t_2)^*, \end{aligned} \tag{D.18}$$

where $\beta_0 = P_n$ is the normalization factor to force $R(u_1, s_1, t_1; u_2, s_2, t_2) = 1$ when $u_1 = u_2$, $s_1 = s_2$, and $t_1 = t_2$. The derivation for (D.18) is similar to that given in Appendix A, and thus omitted here.

By assigning $u_1 = u_2$ and $t_1 = t_2$, we obtain the target SCF on the Tx side,

$$R(s_1; s_2) = \frac{1}{M} \sum_{m=1}^{M} F_{s_1}^{\mathrm{Tx}}(\varphi_{n,m}) F_{s_2}^{\mathrm{Tx}}(\varphi_{n,m})^*. \tag{D.19}$$

By assigning $s_1 = s_2$ and $t_1 = t_2$, we obtain the target SCF on the Rx side,

$$R(u_1; u_2) = \frac{1}{M} \sum_{m=1}^{M} F_{u_1}^{\mathrm{Rx}}(\phi_{n,m}) F_{u_2}^{\mathrm{Rx}}(\phi_{n,m})^*. \tag{D.20}$$

By assigning $s_1 = s_2$ and $u_1 = u_2$, we obtain the target TCF,

$$R(t_1; t_2) = \frac{1}{M} \sum_{m=1}^{M} \exp(j2\pi\vartheta_{n,m} t_1) \exp(j2\pi\vartheta_{n,m} t_2)^*. \tag{D.21}$$

3.2 The STCF for the PFS Method

Using the property of the i.i.d. random initial phase $\Phi_{n,m,k}$ in (D.10), the STCF for the nth cluster of the emulated channel with the PFS method can be derived as

$$\begin{aligned}
&\hat{R}^{\mathrm{PFS}}(u_1, s_1, t_1; u_2, s_2, t_2) \\
&= \frac{1}{\hat{\beta}_0^{\mathrm{PFS}}} \cdot \mathbb{E}\left\{ \hat{h}_{u_1,s_1,n}^{\mathrm{PFS}}(t_1, f) \cdot \hat{h}_{u_2,s_2,n}^{\mathrm{PFS}}(t_2, f)^* \right\} \\
&= \frac{1}{M} \sum_{m=1}^{M} F_{s_1}^{\mathrm{Tx}}(\varphi_{n,m}) F_{s_2}^{\mathrm{Tx}}(\varphi_{n,m})^* \exp(j2\pi\vartheta_{n,m} t_1) \exp(j2\pi\vartheta_{n,m} t_2)^* \\
&\quad \cdot \sum_{k=1}^{K} g_{n,k} F_{u_1}^{\mathrm{Rx}}(\phi_k^{\mathrm{OTA}}) F_{u_2}^{\mathrm{Rx}}(\phi_k^{\mathrm{OTA}})^*,
\end{aligned} \tag{D.22}$$

where $\hat{\beta}_0^{\mathrm{PFS}} = P_n$ is the normalization factor. The derivation for (D.22) is similar to that given in Appendix B, and therefore omitted here. Using the equality in (D.16), (D.22) is recast to

$$\begin{aligned}
&\hat{R}^{\mathrm{PFS}}(u_1, s_1, t_1; u_2, s_2, t_2) \\
&= \frac{1}{M^2} \sum_{m=1}^{M} F_{s_1}^{\mathrm{Tx}}(\varphi_{n,m}) F_{s_2}^{\mathrm{Tx}}(\varphi_{n,m})^* \exp(j2\pi\vartheta_{n,m} t_1) \exp(j2\pi\vartheta_{n,m} t_2)^* \\
&\quad \cdot \sum_{m'=1}^{M} F_{u_1}^{\mathrm{Rx}}(\phi_{n,m'}) F_{u_2}^{\mathrm{Rx}}(\phi_{n,m'})^*.
\end{aligned} \tag{D.23}$$

By assigning $u_1 = u_2$ and $t_1 = t_2$, we obtain the emulated SCF on the Tx side,

$$\hat{R}^{\mathrm{PFS}}(s_1; s_2) = \frac{1}{M} \sum_{m=1}^{M} F_{s_1}^{\mathrm{Tx}}(\varphi_{n,m}) F_{s_2}^{\mathrm{Tx}}(\varphi_{n,m})^*. \tag{D.24}$$

By assigning $s_1 = s_2$ and $t_1 = t_2$, we obtain the emulated SCF on the Rx side,

$$\hat{R}^{\mathrm{PFS}}(u_1; u_2) = \frac{1}{M} \sum_{m=1}^{M} F_{u_1}^{\mathrm{Rx}}(\phi_{n,m}) F_{u_2}^{\mathrm{Rx}}(\phi_{n,m})^*. \tag{D.25}$$

By assigning $s_1 = s_2$ and $u_1 = u_2$, we obtain the emulated TCF,

$$\hat{R}^{\mathrm{PFS}}(t_1; t_2) = \frac{1}{M} \sum_{m=1}^{M} \exp(j2\pi\vartheta_{n,m} t_1) \exp(j2\pi\vartheta_{n,m} t_2)^*. \tag{D.26}$$

By comparing the SCF and TCF for the target channel, i.e. (D.19) to (D.21), with those for the emulated channel with the PFS method, i.e. (D.24) to (D.26), it can be seen the channel second-order characteristics are very well reproduced in each domain separately. However, in the joint domain, the target STCF in (D.18) is different from the emulated STCF in (D.23). Actually, it can be observed the emulated STCF has the Kronecker structure [29] between the joint AoD-Doppler domain and the AoA domain, i.e.

$$\hat{R}^{\mathrm{PFS}}(u_1, s_1, t_1; u_2, s_2, t_2) = \hat{R}^{\mathrm{PFS}}(s_1, t_1; s_2, t_2) \cdot \hat{R}^{\mathrm{PFS}}(u_1; u_2), \tag{D.27}$$

where $\hat{R}(s_1, t_1; s_2, t_2)$ is obtained by setting $u_1 = u_2$ in (D.23). Since the correlation function and the power spectrum are Fourier transform pairs in their respective domains [20], the Kronecker structure of the STCF indicates that the power AoD-Doppler spectrum is independent to the power AoA spectrum cluster-wise for the channel emulated with the PFS method. More intuitively, the same power AoD-Doppler spectrum would be seen by the DUT irrespective of the AoA within each cluster. Note this property is different from the general definition of the target channel model except the target channel model is set so specifically.

3.3 The STCF for the PWS Method

Using the property of the i.i.d. random initial phase $\Phi_{n,m}$ in (D.15), the STCF for the nth cluster of the emulated channel with the PWS method can be

derived as

$$\begin{aligned}
&\hat{R}^{\mathrm{PWS}}(u_1, s_1, t_1; u_2, s_2, t_2) \\
&= \frac{1}{\hat{\beta}_0^{\mathrm{PWS}}} \cdot \mathbb{E}\left\{ \hat{h}^{\mathrm{PWS}}_{u_1,s_1,n}(t_1, f) \cdot \hat{h}^{\mathrm{PWS}}_{u_2,s_2,n}(t_2, f)^* \right\} \\
&= \frac{1}{\hat{\beta}_0^{\mathrm{PWS}}} \frac{P_n}{M} \cdot \sum_{m=1}^{M} F^{\mathrm{Tx}}_{s_1}(\varphi_{n,m}) F^{\mathrm{Tx}}_{s_2}(\varphi_{n,m})^* \exp(j2\pi\vartheta_{n,m}t_1) \exp(j2\pi\vartheta_{n,m}t_2)^* \\
&\quad \cdot \sum_{k=1}^{K} F^{\mathrm{Rx}}_{u_1}(\phi_k^{\mathrm{OTA}}) w_{n,m,k} \sum_{k'=1}^{K} F^{\mathrm{Rx}}_{u_2}(\phi_{k'}^{\mathrm{OTA}})^* w^*_{n,m,k'},
\end{aligned} \tag{D.28}$$

where

$$\hat{\beta}_0^{\mathrm{PWS}} = \frac{P_n}{M} \sqrt{\sum_{m=1}^{M} \left\| \sum_{k=1}^{K} F^{\mathrm{Rx}}_{u_1}(\phi_k^{\mathrm{OTA}}) w_{n,m,k} \right\|^2} \cdot \sqrt{\sum_{m'=1}^{M} \left\| \sum_{k'=1}^{K} F^{\mathrm{Rx}}_{u_2}(\phi_{k'}^{\mathrm{OTA}}) w_{n,m',k'} \right\|^2}, \tag{D.29}$$

is the normalization factor. Using the equality in (D.17), we can obtain

$$\hat{R}^{\mathrm{PWS}}(u_1, s_1, t_1; u_2, s_2, t_2) = R(u_1, s_1, t_1; u_2, s_2, t_2). \tag{D.30}$$

Straightforwardly, the respective correlation functions in individual domains, i.e. the SCF on the Tx/Rx side and the TCF, for the PWS method is the same as that of the target channel as well, and thus omitted here to avoid redundancy.

4 Emulation Accuracy Comparison

As mentioned in Section 2, reproducing the spatial profile on the Rx side is the goal for the MPAC based methods, since the other channel properties can be realized in the CE as in conducted testing. In this section, we first show the emulation accuracy of the PWS method in terms of relative field error (RFE). Then, we compare the emulated SCF on the Rx side between the PFS and the PWS method. The power spectrum in the joint AoD-AoA domain is lastly given to show the Kronecker structure of the emulated channel with the PFS method.

An MPAC setup with $K = 16$ OTA probes evenly located on the OTA ring is used for the simulation throughout this section, as shown in Fig. D.2. The test area is set to 1.6λ in diameter, where λ denotes the wavelength at carrier frequency.

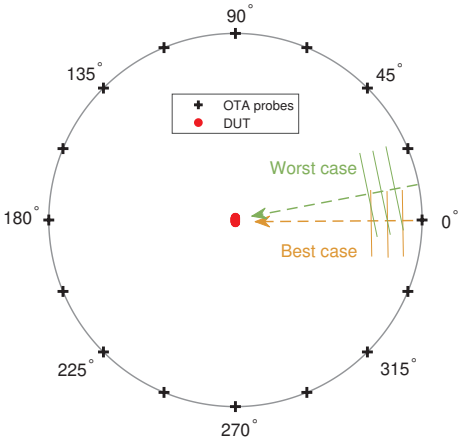

Fig. D.2: The OTA probe configuration for the simulation in Section 4. "Best case" denotes the impinging angle at 0°, and "Worst case" the impinging angle at 11.25°.

4.1 RFE for the PWS Method

The target channel is set to a single plane wave with AoA ϕ_0. It is natural to see the target plane wave being well emulated when its AoA is aligned to any OTA probe, so we present two cases here to check the emulation accuracy of the PWS method, namely the best case and the worst case, as shown in Fig. D.2. In the best case, ϕ_0 is set to 0° at which angle there locates an OTA probe. In the worst case, ϕ_0 is set to 11.25° which is the direction in the middle of two adjacent OTA probes.

The target and the emulated field are evaluated in the local area of size $2.4\lambda \times 2.4\lambda$ containing the test area. For any arbitrary location q in this local area, the amplitude of the target field can be expressed as

$$F_q(\phi_0) = \exp\left(j\frac{2\pi}{\lambda}\langle \boldsymbol{r}_q, \boldsymbol{e}(\phi_0)\rangle\right), \tag{D.31}$$

where $\boldsymbol{r}_q$ is the vector of coordinates for location q. $\boldsymbol{e}(\phi_0)$ is the unit vector pointing at angle ϕ_0. The amplitude of the emulated field can be calculated as

$$\hat{F}_q(\phi_0) = \sum_{k=1}^{K} \exp\left(j\frac{2\pi}{\lambda}\langle \boldsymbol{r}_q, \boldsymbol{e}(\phi_k^{\mathrm{OTA}})\rangle\right) \cdot w_k, \tag{D.32}$$

where w_k is obtained through solving (D.13) with $\phi_{n,m} = \phi_0$ and $w_{n,m,k} = w_k$ for the single plane wave. The magnitude and the phase of $F_q(\phi_0)$ and $\hat{F}_q(\phi_0)$ for the best and the worst case are shown in Fig. D.3. The white circle represents the boundary of the test area with a diameter of 1.6λ. To tell the

difference between the target and the emulated field, the RFE is used as an indicator of deviation, and is calculated as

$$\varepsilon_q = 10 \cdot \log_{10} \frac{\left\| F_q(\phi_0) - \hat{F}_q(\phi_0) \right\|^2}{\left\| F_q(\phi_0) \right\|^2}. \tag{D.33}$$

Fig. D.4 shows the RFE in the region containing the test area in xy plane. The white circle indicates the boundary of the test area. Although we can see the RFE increases outside the test area in the worst case, the RFE within the test area is always low, i.e. up to -25 dB, for both cases. Therefore, the PWS method is capable of reproducing plane waves impinging from any angle with high emulation accuracy.

4.2 SCF on the Rx Side under Different Cluster Angular Spreads

The target channel model is changed to a single cluster with different cluster angular spreads of arrival (CASA), i.e. from 5° to 35° with 5° steps. The cluster is generated with its power AoA spectrum following the Laplacian distribution [1, 14]. The total power of the cluster is set to 1. In total, 20 subpaths are generated in the cluster with equal power, i.e. 0.05 each, but non-uniform AoAs as in [14, Table 4-1]. Similar to Subsection 4.1, the discussion is also split into the best and the worst case. The cluster mean AoA $\bar{\phi}_0$ is set to 0° and 11.25° for the best and the worst case, respectively. The target power spectrum in the AoA domain with 5° CASA for both cases is shown as an example in Fig. D.5. A shift in the cluster mean AoA can be observed between the best case and the worst case.

The power weights for the PFS method and the complex weights for the PWS method are solved with the cost functions given in (D.9) and (D.13), respectively. The SCFs on the Rx side for the emulated channels with the PFS and the PWS method are then calculated with (D.22) and (D.28), respectively, with $s_1 = s_2$ and $t_1 = t_2$. The results are shown in Fig. D.6. It can be observed that the SCF for the PWS method follows the target one almost perfectly for an antenna separation up to 1.6λ for all CASAs in both cases. It is because the PWS method is capable of reproducing a plane wave from arbitrary directions in the test area with a sufficient number of OTA probes as illustrated in Subsection 4.1.

As mentioned in the introduction, the PFS and the PWS method are usually considered to be equal in emulation accuracy [7, 17]. However, it can be observed in Fig. D.6 the deviation in SCF for the PFS method is always larger than that for the PWS method. For both the best and the worst case, the deviation decreases with the increase of CASAs, which shows the PFS method is poor at reproducing clusters with small angular spreads. This is more obvious in the worst case as the deviation occurs at a smaller antenna separation.

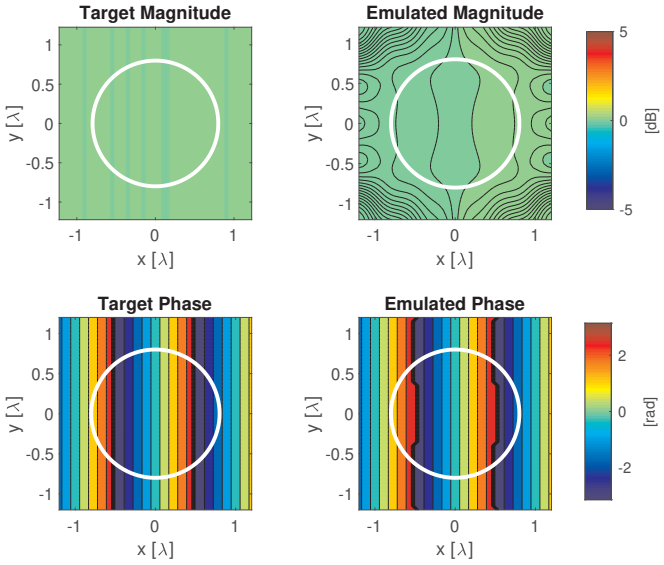

(a)

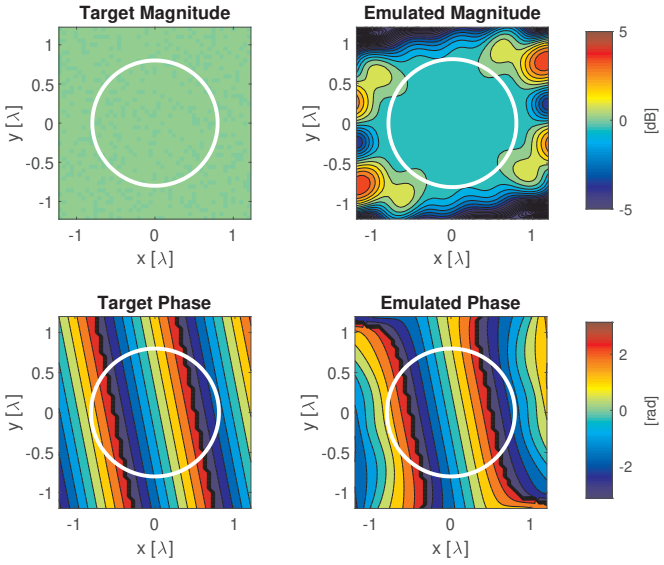

(b)

Fig. D.3: The magnitude and the phase of the target and the emulated field of a single plane wave for (a) the best case, i.e. $\phi_0 = 0°$, and (b) the worst case, i.e. $\phi_0 = 11.25°$ in the local area containing the test area. White circle denotes the boundary of the test area which is 1.6λ in diameter.

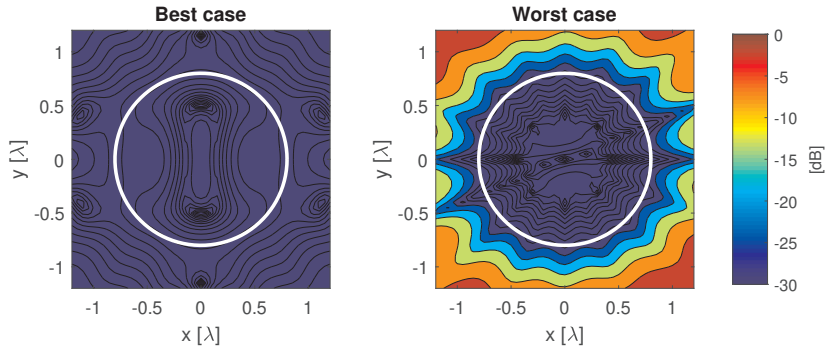

Fig. D.4: RFE calculated in the local area containing the test area for (left) the best case, i.e. $\phi_0 = 0°$, and (right) the worst case, i.e. $\phi_0 = 11.25°$. White circle denotes the boundary of the test area which is 1.6λ in diameter.

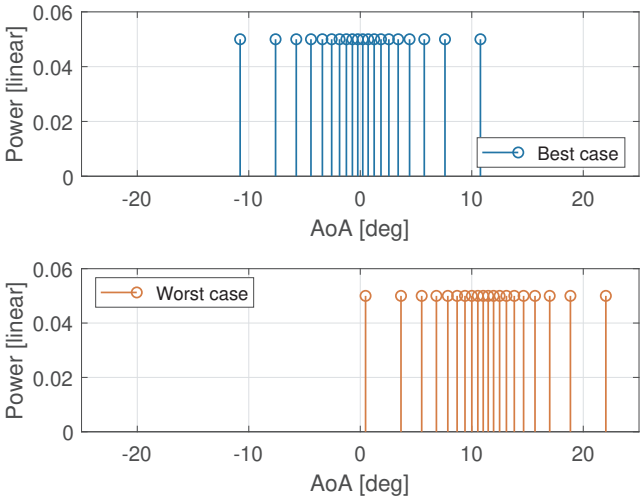

Fig. D.5: Target power spectrum in the AoA domain consisting of 20 subpaths generated according to the standards with 5° CASA for (top) the best case, i.e. $\bar{\phi}_0 = 0°$, and (bottom) the worst case, i.e. $\bar{\phi}_0 = 11.25°$.

When the CASA is very small compared to the angular separation of adjacent OTA probes, e.g. CASA $= 5°$ and $10°$ compared to the $22.5°$ OTA probe separation, the cluster becomes very specular in angular domain. If the specular cluster comes in the direction where there is no OTA probe as in the worst case, the PFS method cannot reproduce it, and the deviation of the SCF is significant even at a small antenna separation as seen in Fig. D.6(b). Recall that the supported test area size is usually determined on the largest antenna separation with respect to an acceptable deviation level in SCF. Therefore, the PWS method supports a larger test area than the PFS method with the same

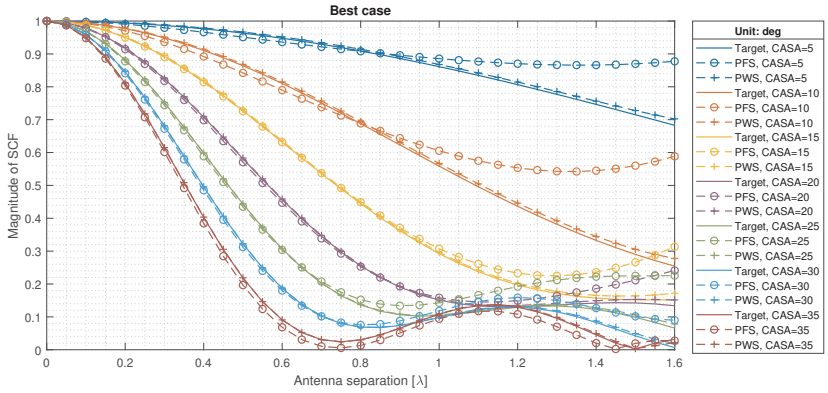

(a)

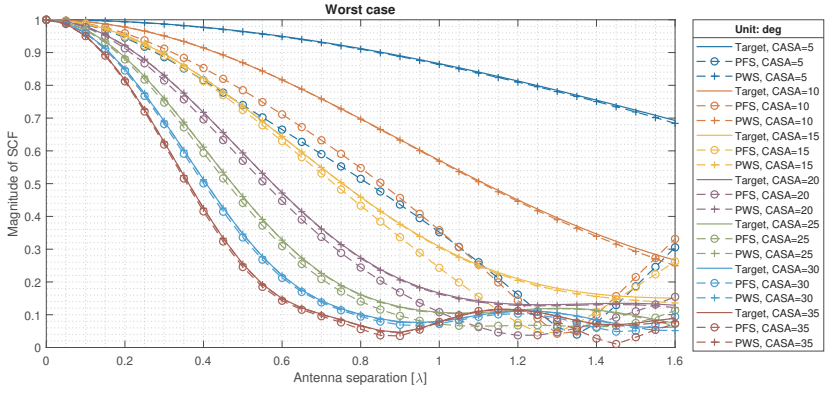

(b)

Fig. D.6: The SCF on the Rx side for (a) the best case, i.e. $\tilde{\phi}_0 = 0°$, and (b) the worst case, i.e. $\tilde{\phi}_0 = 11.25°$, for the target and the emulated channels with the PFS and the PWS method at different CASAs, respectively.

MPAC setup, especially at small CASAs. Note that the results presented in Fig. D.6 are consistent with those reported in [7, 17], where channel models with large CASAs (i.e. 35°) were investigated.

Nonetheless, the SCFs for both methods well follow the target at large CASAs, e.g. 30° and 35°. Therefore, the emulation accuracy can be considered the same for cases such as UE testing where the CASA is large due to surrounding rich scatterers. However, for cases like BS testing where the CASA is small, e.g. 2° and 5° as for SCME Urban Micro-cell (UMi) and Urban Macro-cell (UMa) scenario respectively [13], the two methods shall not be considered the same in terms of emulation accuracy.

4.3 Power Spectrum in Joint AoD-AoA Domain

The target channel is set to a single cluster. The cluster angular spread of departure (CASD) is set to 5°, and the CASA is set to 35° in accordance with the SCME UMi scenario [13]. The cluster mean AoA is set to 0° which corresponds to the best case in Fig. D.6. The cluster mean AoD is also set to 0°. The AoD and the AoA of subpaths are randomly paired to each other. The Tx antenna array is set to a ULA of 4 isotropic antenna elements with 0.5λ element spacing (i.e. 1.5λ in array aperture). The Rx antenna array is set to a ULA with 33 isotropic antenna elements with 0.05λ element spacing (i.e. 1.6λ in array aperture). The broadsides of the Tx and the Rx array are aligned to 0° for the AoD and the AoA domain, respectively. This simulation setting leads to a fair comparison of the emulated channels between the PFS and the PWS method because both methods are capable of emulating the target channel in the test area of size 1.6λ with low errors as observed in Fig. D.6. The true power AoD-AoA spectrum is shown in Fig. D.7 as a reference. However, it is not observable unless we have an infinite large array aperture on both Tx and Rx side.

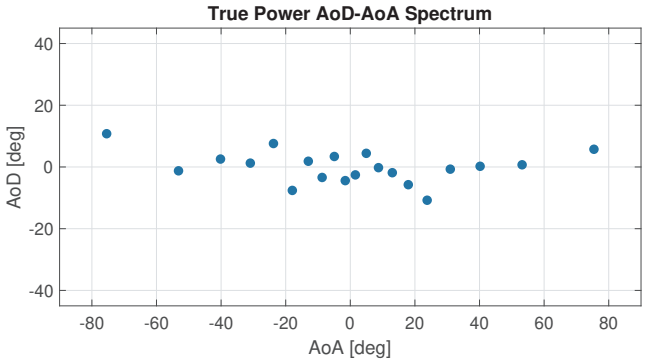

Fig. D.7: True power spectrum of 20 subpaths in the joint AoD-AoA domain generated as the target channel for emulating with the PFS and the PWS method.

Alternatively, the power AoD-AoA spectrum is estimated with the Bartlett beamforming and the multiple signal classification (MUSIC) algorithm [30]. As the input for the Bartlett beamforming and the MUSIC algorithm, the joint Tx-Rx spatial correlation function is obtained from (D.18), (D.22), and (D.28) with $t_1 = t_2$ for the target channel, the PFS method, and the PWS method, respectively.

The estimated power AoD-AoA spectra from the Bartlett beamforming are shown in the upper row in Fig. D.8. Due to the small array aperture confined in the test area, the angular resolution of the Bartlett beamforming is limited. However, we can see that the estimated power AoD-AoA spectrum for the PWS method is more consistent with that for the target channel com-

pared to the PFS method. The MUSIC algorithm is further applied to obtain the power AoD-AoA spectra with a finer angular resolution, as shown in the lower row in Fig. D.8. We can see the estimated power AoD-AoA spectrum of the target channel is more similar to the true one shown in Fig. D.7. However, since the high-resolution MUSIC algorithm is sensitive to emulation errors, the sidelobes in the power AoD-AoA spectrum for the PWS method are higher than those for the target channel. In addition, the Kronecker structure of the power AoD-AoA spectrum for the PFS method can be clearly seen from both the Bartlett beamforming and the MUSIC results, which is consistent with the correlation function analysis given in Subsection 3.2.

Fig. D.9 shows the marginal power AoD spectra and the marginal power AoA spectra obtained from the Bartlett beamforming results given in Fig. D.8. It shows although the power spectra in the joint AoD-AoA domain is different between the two methods, the marginal power spectra are still the same in both domains as expected. Note the marginal power spectra of the MUSIC results are not shown due to the pseudo-spectrum of the MUSIC algorithm.

It was discussed in the literature [31, 32] that the Kronecker model usually underestimates the channel capacity, especially when the spatial correlation at either Tx side or Rx side is high. Therefore, when single cluster channel models are used during performance testing, the underlying channel capacity is supposed to be underestimated. However, for multi-cluster channel models, since the Kronecker structure only appears within the cluster, the AoDs and the AoAs are still dependent between different clusters from the whole channel point of view. In [33, 34], it was shown experimentally the difference between the target channel and the emulated channel with the PFS method is negligible in terms of capacity with small arrays, e.g. 2×2 or 4×2 MIMO. In [17], similar results were observed experimentally in terms of throughput. We postulate the difference is more pronounced for massive MIMO systems due to their higher angular resolution.

5 Conclusions

In this paper, two channel emulation methods for MIMO OTA testing with the MPAC setup, i.e. the PFS and the PWS method, are reviewed. The standard channel model, i.e. the GSCM, is used as the target channel model in this study. The signal models of the emulated channels for the two methods are given. Moreover, the STCF is derived for both methods. It shows the STCF for the PWS method is consistent with that of the target channel, whereas the STCF for the PFS method is Kronecker structured cluster-wise between the joint AoD-Doppler domain and the AoA domain. The correlation functions in the respective AoD, AoA, and Doppler domain are also derived from the STCF for both methods, which agree well with those of the

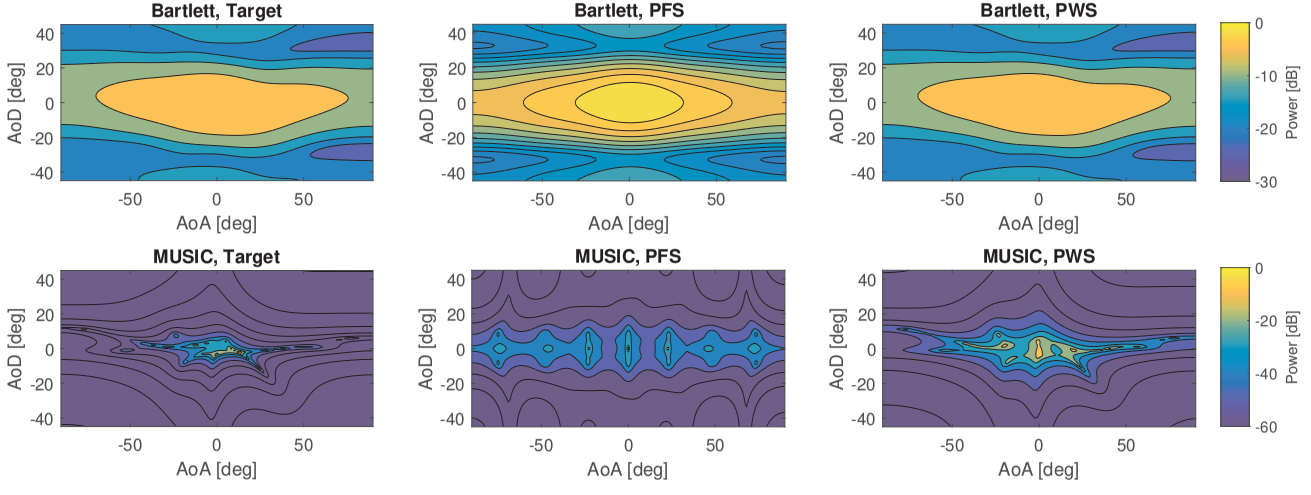

Fig. D.8: The estimated power spectra in the joint AoD-AoA domain for the PFS and PWS method. The Bartlett beamforming results are shown in the upper row with 30 dB power range, and the MUSIC results are shown in the lower row with 60 dB power range.

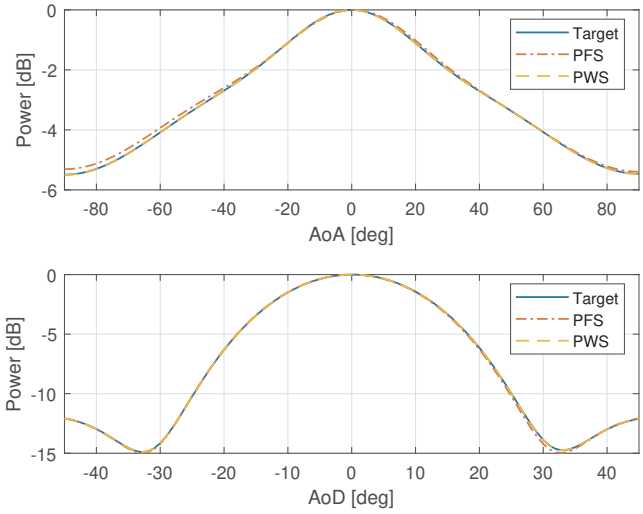

Fig. D.9: The normalized marginal power spectra calculated from the Bartlett power spectrum estimated in Fig. D.8 in (top) the AoA domain, and (bottom) the AoD domain.

target channel.

Simulation is further conducted for both methods with an MPAC setup of 16 OTA probes evenly located on the OTA ring. The SCFs on the Rx side are calculated for the target channel, the PFS method, and the PWS method at different CASAs ranging from 5° to 35° with 5° steps. It shows both methods are capable of reproducing clusters of large CASAs, e.g. from 20° to 35°, for a test area of 1.6λ in size with an acceptable error. However, for a smaller CASA, only the SCF for the PWS method still maintains a good match to the target SCF. The SCF for the PFS method starts to deviate from the target SCF at a small antenna separation, especially when there is no OTA probe located in the direction of the target cluster mean AoA. This difference between the PFS and the PWS method might not be observable for UE-type DUTs due to the large CASA of 35° according to SCME model, but it could be severe for BS-type DUTs. Therefore, it is suggested to remap the target cluster mean AoA to its closest OTA probe to achieve a better emulation accuracy for small CASAs with the PFS method.

The power spectrum in joint AoD-AoA domain is also estimated with the Bartlett beamforming and the MUSIC algorithm for the emulated channels with both methods. A good match can be seen between the estimated power spectrum for the PWS method and the target one. The Kronecker structure of the emulated cluster-wise channel with the PFS method is also observed from the estimated power spectrum. This channel property shall be noted when the target channel model is a single cluster model for performance testing. Although this channel property did not seem to cause huge impact

on UE OTA testing in terms of throughput in the literature, it might be more significant for massive MIMO systems with higher angular resolution.

Finally, the PWS method is more demanding than the PFS method in terms of calibration efforts, but in return, the emulation accuracy of the PWS method is better.

A Derivation of (D.7)

Note that $\left\|F_s^{\mathrm{Tx}}\right\| = 1$ is assumed when calculating $g_{n,k}$ to leave out the effect of Tx antenna pattern on spatial correlation. Inserting (D.4) into (D.7), we can obtain

$$\begin{aligned}
&\rho_{\tilde{u}_1,\tilde{u}_2} \\
&= \frac{1}{\beta_0} \cdot \mathbb{E}\left\{h_{\tilde{u}_1,s,n}(t,f) \cdot h_{\tilde{u}_2,s,n}(t,f)^*\right\} \\
&= \mathbb{E}\Bigg\{\left[\sum_{m=1}^{M} F_s^{\mathrm{Tx}}(\varphi_{n,m}) F_{\tilde{u}_1}^{\mathrm{VA}}(\phi_{n,m}) \cdot \exp(j2\pi\vartheta_{n,m}t + j\Phi_{n,m}) \cdot \exp(-j2\pi f\tau_n)\right] \\
&\quad \cdot \left[\sum_{m'=1}^{M} F_s^{\mathrm{Tx}}(\varphi_{n,m'}) F_{\tilde{u}_2}^{\mathrm{VA}}(\phi_{n,m'}) \cdot \exp(j2\pi\vartheta_{n,m'}t + j\Phi_{n,m'}) \cdot \exp(-j2\pi f\tau_n)\right]^*\Bigg\} \\
&\quad \cdot \frac{1}{\beta_0}\frac{P_n}{M},
\end{aligned} \tag{D.34}$$

where $\beta_0 = P_n$ is the normalization factor. Since we have

$$\mathbb{E}\left\{\exp(j\Phi_{n,m})\exp(j\Phi_{n,m'})^*\right\} = \begin{cases} 1 & \text{when } m = m' \\ 0 & \text{when } m \neq m' \end{cases}, \tag{D.35}$$

(D.34) can be simplified to

$$\rho_{\tilde{u}_1,\tilde{u}_2} = \frac{1}{M}\sum_{m=1}^{M} F_{\tilde{u}_1}^{\mathrm{VA}}(\phi_{n,m}) F_{\tilde{u}_2}^{\mathrm{VA}}(\phi_{n,m})^*, \tag{D.36}$$

by taking only the terms with $m = m'$ into account.

B Derivation of (D.8)

As mentioned in Appendix A, $\left\|F_s^{\mathrm{Tx}}\right\| = 1$ is assumed when calculating $g_{n,k}$ to leave out the effect of Tx antenna pattern on spatial correlation. Inserting

(D.6) into (D.8), we can obtain

$$\begin{aligned}\hat{\rho}_{\tilde{u}_1,\tilde{u}_2} &= \frac{1}{\hat{\beta}_0}\cdot\mathbb{E}\left\{\hat{h}^{\mathrm{PFS}}_{\tilde{u}_1,s,n}(t,f)\cdot\hat{h}^{\mathrm{PFS}}_{\tilde{u}_2,s,n}(t,f)^*\right\}\\ &= \mathbb{E}\Bigg\{\Bigg[\sum_{k=1}^{K}\sum_{m=1}^{M}F_s^{\mathrm{Tx}}(\varphi_{n,m})F^{\mathrm{VA}}_{\tilde{u}_1}(\phi_k^{\mathrm{OTA}})\sqrt{g_{n,k}}\cdot\exp(-j2\pi f\tau_n)\\ &\quad\cdot\exp(j2\pi\vartheta_{n,m}t+j\Phi_{n,m,k})\Bigg]\\ &\quad\cdot\Bigg[\sum_{k'=1}^{K}\sum_{m'=1}^{M}F_s^{\mathrm{Tx}}(\varphi_{n,m'})F^{\mathrm{VA}}_{\tilde{u}_2}(\phi_{k'}^{\mathrm{OTA}})\sqrt{g_{n,k'}}\cdot\exp(-j2\pi f\tau_n)\\ &\quad\cdot\exp(j2\pi\vartheta_{n,m'}t+j\Phi_{n,m',k'})\Bigg]^*\Bigg\}\cdot\frac{1}{\hat{\beta}_0}\frac{P_n}{M},\end{aligned}\tag{D.37}$$

where $\hat{\beta}_0 = P_n$ is the normalization factor. Regarding

$$\mathbb{E}\left\{\exp(j\Phi_{n,m,k})\exp(j\Phi_{n,m',k'})^*\right\} = \begin{cases}1 & \text{when } m=m' \text{ and } k=k'\\ 0 & \text{when } m\neq m' \text{ or } k\neq k'\end{cases},\tag{D.38}$$

(D.37) can be simplified to

$$\hat{\rho}_{\tilde{u}_1,\tilde{u}_2} = \sum_{k=1}^{K} g_{n,k}F^{\mathrm{VA}}_{\tilde{u}_1}(\phi_k^{\mathrm{OTA}})F^{\mathrm{VA}}_{\tilde{u}_2}(\phi_k^{\mathrm{OTA}})^*,\tag{D.39}$$

by taking only the terms with $m = m'$ and $k = k'$ into account.

References

[1] 3GPP, "Measurement of radiated performance for Multiple Input Multiple Output (MIMO) and multi-antenna reception for High Speed Packet Access (HSPA) and LTE terminals," Technical Specification Group Radio Access Network, Tech. Rep. 3GPP TR 37.976 V11.0.0, 2012.

[2] W. Yu, Y. Qi, S. Member, K. Liu, Y. Xu, and A. Two-stage, "Radiated Two-Stage Method for LTE MIMO User," *IEEE Transactions on Electromagnetic Compatibility*, vol. 56, no. 6, pp. 1691–1696, 2014.

[3] W. Fan, P. Kyösti, L. Hentilä, and G. F. Pedersen, "MIMO Terminal Performance Evaluation With a Novel Wireless Cable Method," *IEEE Transactions on Antennas and Propagation*, vol. 65, no. 9, pp. 4803–4814, 2017. [Online]. Available: http://ieeexplore.ieee.org/document/7967858/

[4] P. S. Kildal and K. Rosengren, "Correlation and capacity of MIMO systems and mutual coupling, radiation efficiency, and diversity gain of their antennas: Simulations and measurements in a reverberation chamber," *IEEE Communications Magazine*, vol. 42, no. 12, pp. 104–112, 2004.

[5] X. Chen, "Throughput modeling and measurement in an isotropic-scattering reverberation chamber," *IEEE Transactions on Antennas and Propagation*, vol. 62, no. 4, pp. 2130–2139, 2014.

[6] J. T. Toivanen, T. A. Laitinen, V. M. Kolmonen, and P. Vainikainen, "Reproduction of arbitrary multipath environments in laboratory conditions," *IEEE Transactions on Instrumentation and Measurement*, vol. 60, no. 1, pp. 275–281, 2011.

[7] P. Kyösti, T. Jämsä, and J.-P. Nuutinen, "Channel modelling for multiprobe over-the-air MIMO testing," *International Journal of Antennas and Propagation*, vol. 2012, 2012.

[8] R. K. Sharma, W. Kotterman, M. H. Landmann, C. Schirmer, C. Schneider, F. Wollenschläger, G. Del Galdo, M. A. Hein, and R. S. Thomä, "Over-the-Air Testing of Cognitive Radio Nodes in a Virtual Electromagnetic Environment," *International Journal of Antennas and Propagation*, vol. 2013, 2013.

[9] A. Khatun, V. M. Kolmonen, V. Hovinen, D. Parveg, M. Berg, K. Haneda, K. I. Nikoskinen, and E. T. Salonen, "Experimental Verification of a Plane-Wave Field Synthesis Technique for MIMO OTA Antenna Testing," *IEEE Transactions on Antennas and Propagation*, vol. 64, no. 7, pp. 3141–3150, 2016.

[10] Y. Jing, X. Zhao, H. Kong, S. Duffy, and M. Rumney, "Two-Stage Over-the-Air (OTA) TEST METHOD for LTE MIMO Device Performance Evaluation," *International Journal of Antennas and Propagation*, vol. 2012, 2012.

[11] CTIA, "Test Plan for 2x2 Downlink MIMO and Transmit Diversity Over-the-Air Performance," Tech. Rep. Version 1.1.1, 2017.

[12] 3GPP, "Spatial channel model for Multiple Input Multiple Output (MIMO) simulations," Tech. Rep. 3GPP TR 25.996 V12.0.0, 2014.

[13] D. S. Baum, J. Hansen, G. D. Galdo, and M. Milojevic, "An Interim Channel Model for Beyond-3G Systems," *Vehicular Technology Conference, 2005. VTC 2005-Spring. 2005 IEEE 61st*, vol. 5, pp. 3132–3136, 2005.

[14] WINNER, "WINNER II Channel Models: Part I Channel Models," Tech. Rep. D1.1.2 V1.2, 2007. [Online]. Available: http://projects.celtic-initiative.org/WINNER+/WINNER2-Deliverables/D4.6.1.pdf

[15] W. Fan, X. Carreño, F. Sun, J. Ø. Nielsen, M. B. Knudsen, and G. F. Pedersen, "Emulating spatial characteristics of MIMO channels for OTA testing," *IEEE Transactions on Antennas and Propagation*, vol. 61, no. 8, pp. 4306–4314, 2013.

[16] W. Fan, P. Kyösti, J.-P. Nuutinen, À. O. Martínez, J. Ø. Nielsen, and G. F. Pedersen, "Generating spatial channel models in multi-probe anechoic chamber setups," in *Vehicular Technology Conference (VTC Spring), 2016 IEEE 83rd*, 2016, pp. 1–5.

[17] M. S. Miah, D. Anin, A. Khatun, K. Haneda, L. Hentilä, and E. T. Salonen, "On the Field Emulation Techniques in Over-the-air Testing: Experimental Throughput Comparison," *IEEE Antennas and Wireless Propagation Letters*, vol. 16, pp. 2224–2227, 2017. [Online]. Available: http://ieeexplore.ieee.org/document/7934105/

[18] P. Bello, "Characterization of Randomly Time-Variant Linear Channels," *IEEE Transactions on Communications Systems*, vol. 11, no. 4, pp. 360–393, 1963. [Online]. Available: http://ieeexplore.ieee.org/xpls/abs{_}all.jsp?arnumber=1088793{&}tag=1

[19] B. H. Fleury, "First- and second-order characterization of direction dispersion and space selectivity in the radio channel," *IEEE Transactions on Information Theory*, vol. 46, no. 6, pp. 2027–2044, 2000.

[20] R. Vaughan and J. B. Andersen, *Channels , Propagation and Antennas for Mobile Communications*. The Institution of Electrical Engineers, 2003.

[21] R. He, B. Ai, G. L. Stuber, G. Wang, and D. Z. Zhong, "Geometrical Based Modeling for Millimeter Wave MIMO Mobile-to-Mobile Channels," *IEEE Transactions on Vehicular Technology*, vol. PP, no. 99, pp. 1–16, 2017. [Online]. Available: http://ieeexplore.ieee.org/document/8166731/

[22] J. Meinilä, P. Kyösti, L. Hentilä, T. Jämsä, E. Suikkanen, E. Kunnari, and M. Narandžić, "D5.3: WINNER+ Final Channel Models," Tech. Rep., 2010.

[23] S. Boyd and L. Vandenberghe, *Convex Optimization*. Cambridge University Press, 2004.

[24] W. Fan, X. Carreño, J. Ø. Nielsen, K. Olesen, M. B. Knudsen, and G. F. Pedersen, "Measurement verification of plane wave synthesis technique based on multi-probe MIMO-OTA setup," in *IEEE Vehicular Technology Conference (VTC Fall)*, 2012, pp. 1–5.

[25] E. G. Larsson, O. Edfors, F. Tufvesson, and T. L. Marzetta, "Massive MIMO for next generation wireless systems," *IEEE Communications Magazine*, vol. 52, no. 2, pp. 186–195, 2014. [Online]. Available: http://ieeexplore.ieee.org/lpdocs/epic03/wrapper.htm?arnumber=6736761

[26] K. Guan, G. Li, T. Kurner, A. F. Molisch, B. Peng, R. He, B. Hui, J. Kim, and Z. Zhong, "On Millimeter Wave and THz Mobile Radio Channel for Smart Rail Mobility," *IEEE Transactions on Vehicular Technology*, vol. 66, no. 7, pp. 5658–5674, 2017.

[27] B. Ai, K. Guan, R. He, J. Li, G. Li, D. He, Z. Zhong, and K. M. S. Huq, "On Indoor Millimeter Wave Massive MIMO Channels: Measurement and Simulation," *IEEE Journal on Selected Areas in Communications*, vol. 35, no. 7, pp. 1678–1690, 2017.

[28] P. Kyösti, W. Fan, and J. Kyröläinen, "Assessing measurement distances for OTA testing of massive MIMO base station at 28 GHz," in *2017 11th European Conference on Antennas and Propagation, EUCAP 2017*, 2017, pp. 3679–3683.

[29] C. Oestges, "Validity of the Kronecker Model for MIMO Correlated Channels," in *Vehicular Technology Conference, 2006. VTC 2006-Spring. IEEE 63rd*, vol. 6, 2006, pp. 2818–2822.

[30] H. Krim and M. Viberg, "Two decades of array signal processing research: The parametric approach," *IEEE Signal Processing Magazine*, vol. 13, no. 4, pp. 67–94, 1996.

[31] H. Özcelik, M. Herdin, W. Weichselberger, J. Wallace, and E. Bonek, "Deficiencies of 'Kronecker' MIMO radio channel model," *Electronics*

Letters, vol. 39, no. 16, pp. 1209–1210, 2003. [Online]. Available: http://digital-library.theiet.org/content/journals/10.1049/el{_}20020198

[32] V. Raghavan, J. H. Kotecha, and A. M. Sayeed, "Why does the Kronecker model result in misleading capacity estimates?" *IEEE Transactions on Information Theory*, vol. 56, no. 10, pp. 4843–4864, 2010.

[33] W. Fan, P. Kyösti, J. Ø. Nielsen, and G. F. Pedersen, "Wideband MIMO Channel Capacity Analysis in Multiprobe Anechoic Chamber Setups," *IEEE Transactions on Vehicular Technology*, vol. 65, no. 5, pp. 2861–2871, 2016.

[34] W. Fan, L. Hentilä, P. Kyösti, and G. F. Pedersen, "Test Zone Size Characterization with Measured MIMO Throughput for Simulated MPAC Configurations in Conductive Setups," *IEEE Transactions on Vehicular Technology*, vol. 66, no. 11, pp. 10 532–10 536, 2017. [Online]. Available: http://ieeexplore.ieee.org/document/7981384/

Paper E

Virtual Drive Testing Over-The-Air for Vehicular Communications

Yilin Ji, Wei Fan, Mikael Nilsson, Lassi Hentilä,
Kristian Karlsson, Fredrik Tufvesson,
and Gert Frølund Pedersen

The paper has been published in the
IEEE Transactions on Vehicular Technology Vol. 69, No. 2, pp. 1203–1213, 2020.

Abstract

Multiple-input multiple-output (MIMO) over-the-air (OTA) testing is a standardized procedure to evaluate the performance of MIMO-capable devices such as mobile phones and laptops. With the growth of the vehicle-to-everything (V2X) service, the need for vehicular communication testing is expected to increase significantly. The so-called multi-probe anechoic chamber (MPAC) setup is standardized for MIMO OTA testing. Typically, a test zone of 0.85 *wavelength in diameter can be achieved with an 8-probe MPAC setup, which can encompass device-under-test (DUT) of small form factors. However, a test zone of this size may not be large enough to encompass DUTs such as cars. In this paper, the sufficient number of OTA probes for the MPAC setup for car testing is investigated with respect to the emulation accuracy. Our investigation shows that the effective antenna distance of the DUT is more critical than its physical dimensions to determine the required number of OTA probes. In addition, throughput measurements are performed under the standard SCME UMa and UMi channel models with the 8-probe MPAC setup and the wireless cable setup, i.e. another standardized testing setup. The results show reasonably good agreement between the two setups for MIMO OTA testing with cars under the standard channel models.*

1 Introduction

1.1 Background of MIMO OTA Testing

Virtual drive testing (VDT) refers to evaluating the radio performance of wireless devices in laboratory environments [1]. Compared to unpredictable and expensive field trials in open environment, it allows for testing in more controllable and reproducible conditions. Within the context of VDT, multiple-input multiple-output (MIMO) over-the-air (OTA) testing is a standardized procedure to perform testing for MIMO-capable devices. It helps the manufacturers identify potential design flaws and production defects during the early-stage prototyping, mid-term refinement, and final massive roll-out.

Basically, three main types of MIMO OTA testing setups are defined in the standard [1], namely the multi-probe anechoic chamber (MPAC) setup, the wireless cable setup, and the reverberation chamber (RC) setup. The purpose of MIMO OTA testing is to evaluate the radio performance of device-under-test (DUT) under target propagation channels. Therefore, the key difference between different testing setups, besides the cost in complexity and expense, can be viewed in terms of the capability of emulating target channels.

The MPAC setup utilizes a channel emulator and a set of OTA probes to emulate target channels. The challenge of the MPAC setup usually occurs for emulating the target power angle spectrum (PAS) on the DUT side with

OTA probes. The so-called test zone of an MPAC setup is defined as a geometric area where the target spatial correlation, i.e. the Fourier transform of the PAS, on the DUT side can be well approximated. The size of the test zone is determined mainly by the number of OTA probes with its diameter approximately proportional to the number of OTA probes [2]. Another terminology, namely the quiet zone, is also important to the MPAC setup, and it is often used in antenna measurement. It is defined as the geometric area where the field is homogeneous, and it is determined by the measurement range and reflectivity level. Note that in this study we focus on the test zone where channel spatial profiles can be controlled.

The wireless cable setup [3], also called the radiated two-stage (RTS) setup, utilizes a channel emulator to emulate target channels. The principle of the wireless cable setup is similar to that of the conducted two-stage setup except that the cable connections between the channel emulator output ports and the DUT antenna ports are realized over the air, and hence the name wireless cable. The quality of the realized wireless cable connections is measured by the isolation level. An ill-conditioned transfer function between the channel emulator output ports and the DUT antenna ports, e.g. in the case where the DUT antennas are closely located, may limit the achievable isolation level. In addition, the DUT antenna pattern is implemented numerically in the channel emulator, so the wireless cable setup is not capable of testing DUT with active antenna arrays. Therefore, the wireless cable setup is not a true end-to-end testing method as the MPAC setup.

Finally, the RC setup utilizes a metallic cavity and stirrers to generate isotropic spatial channels with Rayleigh fading due to the rich multipaths in the RC [4, 5]. Therefore, it is not as capable of generating arbitrary channel models as the MPAC and the wireless cable setup.

1.2 Problem Statement

Long term evolution for vehicles (LTE-V) has been proposed to embody the vehicle-to-everything (V2X) service defined in the standardization group 3GPP [6]. With the LTE-V technology, it is expected to make road traffic safer and more efficient. A key component to enable the V2X service is a high-quality communication for vehicles. To assess the communication performance of the LTE-V during design phase, LTE mobile phones connected with external test antennas, e.g. shark-fin antennas, can be used to perform the standard MIMO OTA testing.

Since shark-fin antennas are usually mounted on car roofs for a clear field of view, potentially the roof also participates in the antenna radiation, which leads to induced surface currents being distributed on it. In such cases, the effective antenna distance of the DUT can be larger than the physical distance between the DUT antennas. However, depending on the specific radiation

pattern of the DUT antennas, it is also possible that the induced surface currents concentrate only in the vicinity of the DUT antennas. Consequently, the resulting effective antenna distance can be much smaller than the dimension of the whole car, i.e. the upper bound of the effective antenna distance.

For the MPAC setup, it is required that the underlying test zone is larger than the effective antenna distance. There is a strong need in the industry to find out to which extent the presence of cars will affect the effective antenna distance, or equivalently the required size of the test zone, since a smaller test zone leads to a smaller number of required OTA probes and hence a lower system cost of the MPAC setup. To the best of our knowledge, this is still remained unknown in the literature.

1.3 State-of-the-art

The state-of-the-art on OTA testing for vehicles can be found for testing methodology verification [7–12] and vehicular channel models [12–15], respectively. In [7], an experiment with a car under a multi-probe setup in an open area was performed, and it was found the coupling from the OTA probes and the reflection and diffraction from cars are negligible, which verified the effectiveness of the quiet zone of the multi-probe setup for car testing. In [8], antenna correlation on cars was investigated with 3 OTA probes, and the measurements showed the similarity with the theoretical antenna correlation to some extent. In [9], an isolation level of about 40 dB was achieved experimentally for a wireless cable setup with 6 OTA probes in a radio-frequency (RF) shielded room, which demonstrated the achievable quality of wireless cable connections for cars. In [10], throughput measurements for cars were performed in a semi-anechoic chamber, where the ground was not covered by absorber, with a single OTA probe under single-path line-of-sight (LoS) channels. In [11], a plane-wave generator (PWG) solution was reported as an alternative for the compact antenna test range (CATR) setup [12] under single-path LoS channels. In [13], discussion was given on the properties of vehicular channels, and measurement-based path loss and shadowing models were proposed for vehicle-to-vehicle (V2V) communication in highway and urban scenarios in [14, 15]. However, to the best of our knowledge, investigation on MIMO OTA testing for cars with the MPAC and the wireless cable setup under the standardized channel models is still missing in the literature.

1.4 Contribution

In this paper, the principles of the MPAC and the wireless cable method for MIMO OTA testing are briefly revisited. Three DUT setups are used for testing with supposedly different effective antenna distances. For the MPAC

method, the sufficient number of OTA probes for different DUT setups is synthetically investigated in terms of the emulation accuracy based on three metrics, i.e. the average received power, branch power ratio, and antenna correlation at the DUT side. For the wireless cable method, the isolation level between connections is used to evaluate the emulation accuracy, and the achieved values in the measurements are shown. Finally, throughput measurements are performed with the two methods under standard channel models, and comparison between the results is made.

The main contribution of the paper lies in the following aspects:

- The sufficient size of the test zone, or equivalently the sufficient number of OTA probes, is synthetically investigated for cars with the MPAC setup.
- Throughput measurements are performed for cars with the MPAC and the wireless cable setup, and comparison between the results is presented.

The rest of the paper is structured as follows: Section 2 introduces the principle of the MPAC and the wireless cable method for MIMO OTA testing. The metrics to evaluate the emulation accuracy for the MPAC and the wireless cable setup are also given in Section 2. Section 3 describes the measurement campaign with the detailed setup and setting information. Section 4 presents the obtained values for the emulation accuracy metrics and the measured throughput results. Section 5 concludes the paper.

2 Principle of OTA Methods

2.1 The Target Channel Model

In the current standard [1], the channel model mostly used for MIMO OTA testing is the 3GPP Spatial Channel Model Extended (SCME) including Urban Macro-cell (UMa) and Urban Micro-cell (Umi) scenarios [16]. The SCME model belongs to the family of geometry-based stochastic channel models (GSCM) [17–19]. Within the context of GSCMs, propagation channels are modelled as the superposition of a number of propagation paths, and paths having similar propagation parameters are further grouped into clusters to lower the model complexity.

Given a MIMO communication system with S transmit (Tx) antennas and U receive (Rx) antennas, the time-variant channel transfer function from the sth Tx antenna to the uth Rx antenna can be expressed as [19]

$$h_{u,s}(t,f) = \sum_{n=1}^{N} h_{u,s,n}(t,f), \tag{E.1}$$

where t and f denote the time and the frequency, respectively. The subscript n is the index of the cluster and N the total number of clusters. The contribution of the nth cluster can be further expressed as

$$h_{u,s,n}(t,f) = \sqrt{\frac{P_n}{M}} \sum_{m=1}^{M} \begin{bmatrix} F^{\mathrm{V}}_{s,\mathrm{Tx}}(\phi_{n,m}) \\ F^{\mathrm{H}}_{s,\mathrm{Tx}}(\phi_{n,m}) \end{bmatrix}^{\mathrm{T}} \boldsymbol{A} \begin{bmatrix} F^{\mathrm{V}}_{u,\mathrm{Rx}}(\theta_{n,m}) \\ F^{\mathrm{H}}_{u,\mathrm{Rx}}(\theta_{n,m}) \end{bmatrix} \cdot \exp(j2\pi v_{n,m} t) \cdot \exp(-j2\pi f \tau_n), \tag{E.2}$$

where m is the index of the path of a cluster, and $v_{n,m}$, $\theta_{n,m}$, and $\phi_{n,m}$ denote the Doppler frequency, the angle of arrival (AoA), and the angle of departure (AoD) of the (n,m)th path, i.e. the mth path of the nth cluster, respectively. M is the total number of paths in a cluster. P_n and τ_n are the power and the delay of the nth cluster, respectively. The terms $F^{\mathrm{V}}_{u,\mathrm{Rx}}(\cdot)$ and $F^{\mathrm{H}}_{u,\mathrm{Rx}}(\cdot)$ are the complex radiation pattern of the uth Rx antenna in the vertical (V) and the horizontal (H) polarization, respectively. Similarly, $F^{\mathrm{V}}_{s,\mathrm{Tx}}(\cdot)$ and $F^{\mathrm{H}}_{s,\mathrm{Tx}}(\cdot)$ are those of the sth Tx antenna in the V and the H polarization, respectively. Furthermore, $\boldsymbol{A}$ is the polarization matrix which reads

$$\boldsymbol{A} = \begin{bmatrix} \exp\left(j\Phi^{\mathrm{VV}}_{n,m}\right) & \sqrt{\kappa^{-1}_{n,m}} \exp\left(j\Phi^{\mathrm{VH}}_{n,m}\right) \\ \sqrt{\kappa^{-1}_{n,m}} \exp\left(j\Phi^{\mathrm{HV}}_{n,m}\right) & \exp\left(j\Phi^{\mathrm{HH}}_{n,m}\right) \end{bmatrix}, \tag{E.3}$$

where $\Phi^{\mathrm{VV}}_{n,m}$, $\Phi^{\mathrm{VH}}_{n,m}$, $\Phi^{\mathrm{HV}}_{n,m}$, and $\Phi^{\mathrm{HH}}_{n,m}$ are the initial phases of the (n,m)th path for the vertical-to-vertical (VV), the horizontal-to-vertical (HV), the vertical-to-horizontal (VH), and the horizontal-to-horizontal (HH) polarizations, respectively. Moreover, they are usually characterized as independent and identical distributed (i.i.d.) random variables following the uniform distribution over $[0, 2\pi]$. $\kappa_{n,m}$ is the cross-polarization ratio (XPR) of the (n,m)th path.

2.2 The MPAC Based Methods

2.2.1 Principle

The MPAC based methods generally include two specific methods called the prefaded signals synthesis (PFS) and the plane wave synthesis (PWS), respectively. The detailed emulation principle can be found in [2]. Here we briefly describe that of the PFS method, which is more commonly used in practice in the industry.

The PFS method is developed based on the wide-sense stationary uncorrelated scattering (WSSUS) assumption [20] for the target channel model. Since the parameters of the target channel are time-invariant and the initial phases of the (n,m)th path are i.i.d. random variables, the target channel model fulfils the WSSUS assumption, with which the channel can be fully

characterized by its second-order statistics, i.e. the correlation functions in the respective domains of the channel [21].

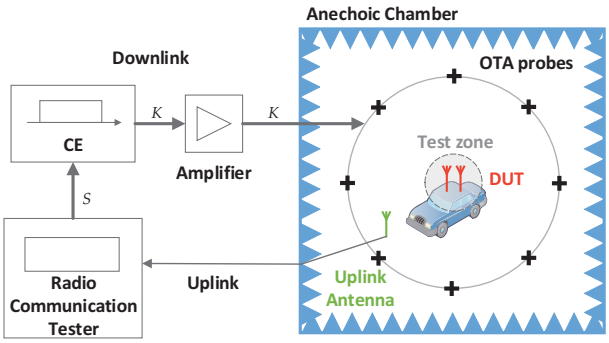

Fig. E.1: The diagram of MIMO OTA testing with an MPAC setup. S is the number of Tx antennas, and K is the number of dual-polarized OTA probes. Acronyms: channel emulator (CE).

A typical MPAC setup is shown in Fig. E.1. For the downlink, test signals are sent from a radio communication tester, e.g. a base station emulator, through coaxial cables to a channel emulator. The test signals are convolved with the channel in the channel emulator so the prefaded signals are generated. Further, the signals are amplified and fed to the OTA probes. Finally, the emulated channel complied with the target channel is generated in the test zone to test the DUT. For the uplink, the uplink antenna picks up the signal from the DUT and sends it back to the radio communication tester.

For an MPAC setup with K dual-polarized OTA probes, the fading sequences corresponding to the nth cluster fed to the kth OTA probe antenna can be expressed as [2, 22]

$$h^{\mathrm{V}}_{k,s,n}(t,f) = \sqrt{\frac{P_n}{M}} \sum_{m=1}^{M} \begin{bmatrix} F^{\mathrm{V}}_{s,\mathrm{Tx}}(\phi_{n,m}) \\ F^{\mathrm{H}}_{s,\mathrm{Tx}}(\phi_{n,m}) \end{bmatrix}^{\mathrm{T}} \boldsymbol{A}_k \begin{bmatrix} 1 \\ 0 \end{bmatrix} \cdot \sqrt{g_{k,n}} \cdot \exp(j2\pi v_{n,m} t) \cdot \exp(-j2\pi f \tau_n), \tag{E.4}$$

$$h^{\mathrm{H}}_{k,s,n}(t,f) = \sqrt{\frac{P_n}{M}} \sum_{m=1}^{M} \begin{bmatrix} F^{\mathrm{V}}_{s,\mathrm{Tx}}(\phi_{n,m}) \\ F^{\mathrm{H}}_{s,\mathrm{Tx}}(\phi_{n,m}) \end{bmatrix}^{\mathrm{T}} \boldsymbol{A}_k \begin{bmatrix} 0 \\ 1 \end{bmatrix} \cdot \sqrt{g_{k,n}} \cdot \exp(j2\pi v_{n,m} t) \cdot \exp(-j2\pi f \tau_n), \tag{E.5}$$

for the V and the H polarization, respectively. In (E.4) and (E.5), $g_{k,n}$ with $\sum_{k=1}^{K} g_{k,n} = 1$ is the power weight applied at the kth OTA probe for the nth cluster. Moreover, $\boldsymbol{A}_k$ is the polarization matrix for the kth OTA probe, which

reads

$$\boldsymbol{A}_k = \begin{bmatrix} \exp\left(j\Phi^{\mathrm{VV}}_{n,m,k}\right) & \sqrt{\kappa^{-1}_{n,m}}\exp\left(j\Phi^{\mathrm{VH}}_{n,m,k}\right) \\ \sqrt{\kappa^{-1}_{n,m}}\exp\left(j\Phi^{\mathrm{HV}}_{n,m,k}\right) & \exp\left(j\Phi^{\mathrm{HH}}_{n,m,k}\right) \end{bmatrix}, \tag{E.6}$$

where $\Phi^{\mathrm{VV}}_{n,m,k}$, $\Phi^{\mathrm{VH}}_{n,m,k}$, $\Phi^{\mathrm{HV}}_{n,m,k}$, and $\Phi^{\mathrm{HH}}_{n,m,k}$, similar to those in (E.3), are also i.i.d. random variables following the uniform distribution over $[0, 2\pi]$, respectively. We can see in (E.4) and (E.5) that the parameter domains of the target channel, i.e. the delay, Doppler frequency, AoD, and polarizations, are implemented in the channel emulator and with the dual-polarized OTA probes. Therefore, the core of the PFS method is to emulate the target PAS on the DUT side, or alternatively its Fourier transform dual, the spatial correlation on the DUT side by applying a proper set of $g_{k,n}$. The set of $g_{k,n}$ can be solved by minimizing the difference between the spatial correlation of the emulated channel and that of the target channel through convex optimization in the test zone [2]. The emulated channel for the nth cluster from the sth Tx antenna to the uth DUT antenna can be written as

$$\begin{aligned} &\hat{h}_{u,s,n}(t,f) \\ &= \sum_{k=1}^{K} \left\{ F^{\mathrm{V}}_{u,\mathrm{Rx}}(\theta_k) \cdot h^{\mathrm{V}}_{k,s,n}(t,f) + F^{\mathrm{H}}_{u,\mathrm{Rx}}(\theta_k) \cdot h^{\mathrm{H}}_{k,s,n}(t,f) \right\}, \end{aligned} \tag{E.7}$$

which shares the common second-order statistics with the target channel $h_{u,s,n}(t,f)$ [21].

2.2.2 Metrics of Emulation Accuracy for the MPAC Method

Given the DUT antenna radiation pattern, we can calculate metrics such as the average received power, the branch power ratio, and the antenna correlation at the DUT side under the target and the emulated channel, respectively, to evaluate the emulation accuracy [22].

Taking a 2×2 MIMO system for example, the average received power at the uth Rx branch with $u = \{1, 2\}$, under the target channel can be calculated as

$$\bar{P}_u = \mathbb{E}_t\left\{ \sum_s \left| \sum_\tau H_{u,s}(t,\tau) \right|^2 \right\}, \tag{E.8}$$

where $\mathbb{E}_t\{\cdot\}$ is the averaging operator over time t, $|\cdot|$ is the modulus operator, and $H_{u,s}(t,\tau)$ is the time-variant channel impulse response in the delay τ domain transformed from $h_{u,s}(t,f)$ through inverse Fourier transform.

The branch power ratio between the two Rx antennas can be further calculated as

$$\Delta\bar{P} = \left| 10\log_{10}(\bar{P}_1) - 10\log_{10}(\bar{P}_2) \right|. \tag{E.9}$$

Similarly, by replacing the target channel with the emulated channel in (E.8), we can obtain the average received power and the branch power ratio for the emulated channel.

The complex-valued antenna correlation between the two Rx antennas with respect to the sth Tx antenna with $s = \{1, 2\}$ can be calculated as [8]

$$\begin{aligned}\rho_s &= corr\left(\sum_{\tau} H_{1,s}(t,\tau), \sum_{\tau} H_{2,s}(t,\tau)\right) \\ &= \frac{\mathbb{E}_t\{\sum_{\tau} H_{1,s}(t,\tau) \cdot \sum_{\tau'} H_{2,s}(t,\tau')^*\}}{\sqrt{\mathbb{E}_t\{|\sum_{\tau} H_{1,s}(t,\tau)|^2\} \cdot \mathbb{E}_t\{|\sum_{\tau'} H_{2,s}(t,\tau')|^2\}}},\end{aligned} \tag{E.10}$$

where $corr(\cdot,\cdot)$ denotes the Pearson correlation, and $(\cdot)^*$ is the complex conjugate. Since the antenna gain pattern is the same between the two assumed base station (BS) antennas [1], the antenna correlation between the Rx antennas is irrelevant to the Tx antennas, i.e. $\rho_1 = \rho_2$.

2.3 The Wireless Cable Method

2.3.1 Principle

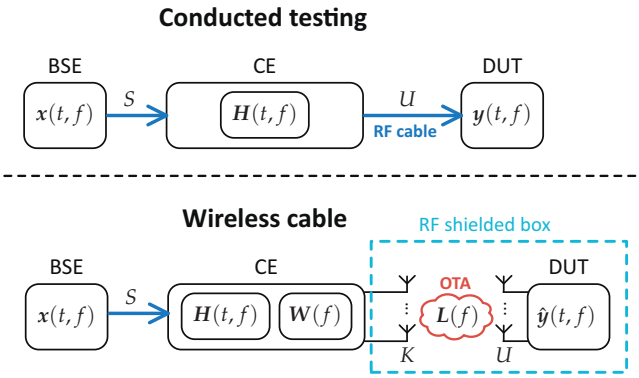

Fig. E.2: The block diagrams of the conducted testing method and the wireless cable method. S and U are the number of Tx and Rx antennas, respectively. K is the number of OTA probes. Acronyms: base station emulator (BSE), channel emulator (CE).

The wireless cable method is another way to replace the traditional conducted testing method. The block diagrams of the conducted testing method and the wireless cable method are shown in Fig. E.2. For the conducted testing, the test signals $\boldsymbol{x}(t,f) \in \mathbb{C}^{S\times 1}$ are sent from a base station emulator to the channel emulator via RF coaxial cables. After convolving with the target channel $\boldsymbol{H}(t,f) = \{h_{u,s}(t,f)\} \in \mathbb{C}^{U\times S}$ as in (E.1), the faded signals

$\boldsymbol{y}(t,f) \in \mathbb{C}^{U\times 1}$ are forwarded to the DUT, again via cables. The signal model for the conducted method can be written as

$$\boldsymbol{y}(t,f) = \boldsymbol{H}(t,f) \cdot \boldsymbol{x}(t,f). \tag{E.11}$$

For the wireless cable method, a weighting matrix $\boldsymbol{W}(f) \in \mathbb{C}^{K\times S}$ is generated in the channel emulator in addition to the target channel $\boldsymbol{H}$. The signals output from the channel emulator are first radiated via K OTA probes. The signals then propagate over the air with a transfer function $\boldsymbol{L}(f) \in \mathbb{C}^{U\times K}$. Lastly they are received by the U DUT antennas. An RF shielded box is used to exclude interference from the environment. The signal model for the wireless cable method can be written as

$$\hat{\boldsymbol{y}}(t,f) = \boldsymbol{L}(f) \cdot \boldsymbol{W}(f) \cdot \boldsymbol{H}(t,f) \cdot \boldsymbol{x}(t,f). \tag{E.12}$$

The weighting matrix $\boldsymbol{W}$ is designed so that $\boldsymbol{L}(f) \cdot \boldsymbol{W}(f)$ approximates an identity matrix $\boldsymbol{I}_U \in \mathbb{C}^{U\times U}$, and hence $\hat{\boldsymbol{y}}$ approximates $\boldsymbol{y}$. Note that $\boldsymbol{L}(f)$ and $\boldsymbol{W}(f)$ are usually evaluated at center frequencies for narrowband systems. If the transfer function $\boldsymbol{L}$ is known, $\boldsymbol{W}$ can be easily solved by the least squares method. Note that $K \geq U$ is required, and it is a necessary but insufficient condition to obtain a unique solution of $\boldsymbol{W}$ [3]. However, knowing $\boldsymbol{L}$ requires that the DUT is able to report the transfer function, which is not a common feature of current user terminals. Therefore, the transfer function $\boldsymbol{L}$ is typically unavailable in practice. In this case, methods for determining $\boldsymbol{W}$ with the average received power level, e.g. the reference signal received power (RSRP) in LTE, have been developed [3].

2.3.2 Metrics of Emulation Accuracy for the Wireless Cable Method

Consider a 2×2 MIMO system with $K = 4$ OTA probes for example to establish the wireless cable connections. Due to the maximum rank of the weighting matrix $\boldsymbol{W} \in \mathbb{C}^{4\times 2}$ is 2, one way to formulate $\boldsymbol{W}$ can be found in [3] as

$$\boldsymbol{W} = \begin{bmatrix} 1 & 0 \\ w_1 & 0 \\ 0 & 1 \\ 0 & w_2 \end{bmatrix}, \tag{E.13}$$

with two degrees of freedom w_1 and w_2. The upper two rows in (E.13) are responsible for establishing the wireless cable connection to the first Rx antenna on the DUT, and the lower two rows are for the connection to the second Rx antenna. The proper weights w_1 and w_2 are found sequentially for the first and the second wireless cable connection. To find the weight w_1, the lower two rows of $\boldsymbol{W}$ are set to zeros. The amplitude and phase of w_1 are tuned,

and the received signal power RSRP on the two Rx antennas are reported. The isolation level for the first and the second wireless cable connection can be calculated as

$$\eta_1(w_1) = \frac{RSRP_1(w_1)}{RSRP_2(w_1)}, \tag{E.14}$$

$$\eta_2(w_2) = \frac{RSRP_2(w_2)}{RSRP_1(w_2)}, \tag{E.15}$$

respectively, where $RSRP_u$ denotes the RSRP value at the uth Rx branch with $u = \{1,2\}$. The proper weight w_1 is found when the isolation level $\eta_1(w_1)$ achieves its maximum. Similarly, the proper weight w_2 for the second wireless cable connection can be found when $\eta_2(w_2)$ achieves its maximum with the upper two rows of $\boldsymbol{W}$ set to zeros. The isolation level is used as a metric to evaluate the quality of the wireless cable connections.

3 Measurement Campaign

3.1 Measurement Setup and Equipment

Photos of the measurement setup are given in Fig. E.3. The measurements were performed in an anechoic chamber of dimensions 20.6 m × 11.8 m × 7.8 m. In total, 8 dual-polarized OTA probes were evenly placed in the azimuth plane on a circle of 5 m in radius (OTA ring). Two-element shark-fin antennas were used as the DUT antennas, which were connected to a mobile phone (UE) to perform throughput measurements. The OTA probes were placed on the same hight of the DUT antennas at around 1.78 m above the floor. The measurements with the MPAC and the wireless cable method were both done with this setup. Table E.1 details the equipment specifications and the measurement settings.

3.2 DUT antenna Setups

Three DUT setups are considered in the measurements, namely "Setup A", "Setup B", and "Setup C". In Setup A, a shark-fin antenna was mounted on a 1 m × 1 m metal sheet. The shark-fin antenna consists of two antenna elements with around 80 mm spacing, which forms a two-port system. In Setup B, a shark-fin antenna of the same type was mounted on the roof of a car (of dimensions 495 cm × 201 cm × 178 cm) at the regular position for vehicle antennas. In Setup C, two shark-fin antennas were mounted on the sides of the roof with around 81 cm spacing. In this setup, one element for each shark-fin antenna was used so that still a two-port system was formed

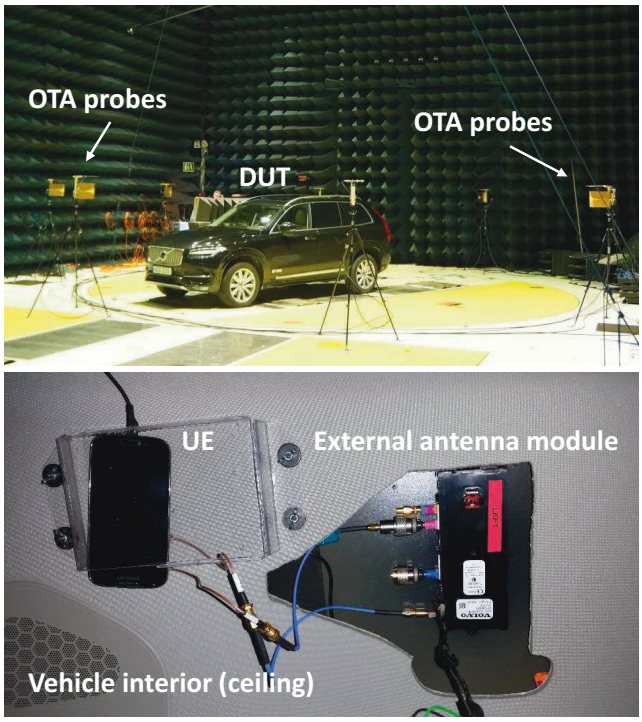

Fig. E.3: A photo of the OTA measurement Setup. (Top) the measurement car with 8 dual-polarized OTA probes in the anechoic chamber; (bottom) the two-port external antenna module connected to an LTE device for throughput measurements.

but with a larger element spacing compared to Setup B. Photos of the three setups are given in Fig. E.4. The center of the antenna was aligned to the center of the OTA ring in Setup A and B, while the geometry center of the two antennas was aligned to the center of the OTA ring in Setup C.

The antenna radiation pattern was measured for all three DUT setups in the same chamber, and the results are given in Fig. E.5. Higher gain is observed in the V polarization for all setups, which indicates the measured shark-fin antennas are vertically polarized. Moreover, the measured antenna radiation pattern varies significantly among the three setups.

4 Measurement Results Analysis

Table E.1: Equipment specifications and measurement settings.

Components	Specifications and settings
Base Station Emulator	• Model: Anritsu MT8820C. • Reference channel: R.35 FDD [23]. • Frame structure: frequency division duplex. • LTE frequency band: 1 (i.e. 2140 MHz). • Channel bandwidth: 10 MHz. • Transmission mode: 2×2 open loop MIMO.
Channel Emulator	• Model: Keysight PropSim F32. • BS antenna: 2 co-located $\pm 45^{\circ}$ slanted isotropic dipoles [1]. • Channel model: SCME UMa and UMi channel model [16].
OTA Probes	• MPAC: 8 dual-polarized Vivaldi antennas evenly distributed on the OTA ring. • Wireless cable: 4 vertical-polarized antennas out of the 8 dual-polarized Vivaldi antennas. • OTA ring radius: 5 m.
DUT	• External antennas: Shark-fin antennas with 2 antenna elements under 3 setups as described in Subsection 3.2. Element spacing: 80 mm. • UE: Samsung Galaxy S4. • Vehicle: Volvo XC 90. Dimensions: 495 cm $\times$ 201 cm $\times$ 178 cm. • Metal sheet: Dimensions: 1 m $\times$ 1 m.

4.1 Synthetic Evaluation of the Emulation Accuracy for the MPAC Method

It is reported in the standard [1] that an 8-probe MPAC setup can support a test zone of 0.85λ (about 12 cm at the testing frequency) in diameter for the target channel model, i.e. the SCME UMa and UMi model. This size is big enough to enclose one shark-fin antenna in our case. However, considering the ground plane in Setup A and the car in Setup B and Setup C, on which the induced surface current is distributed, the total size of the DUT including the ground plane or the car can be larger than the test zone. Therefore, it is necessary to verify the emulation accuracy under those conditions.

The three metrics discussed in Subsection 2.2.2, i.e. the average received power, the branch power ratio, and the antenna correlation at the DUT side were evaluated with the synthetic 8-probe (8P), 16-probe (16P), and 32-probe (32P) MPAC setup [24] according to (E.8) to (E.10). Recall that the size of

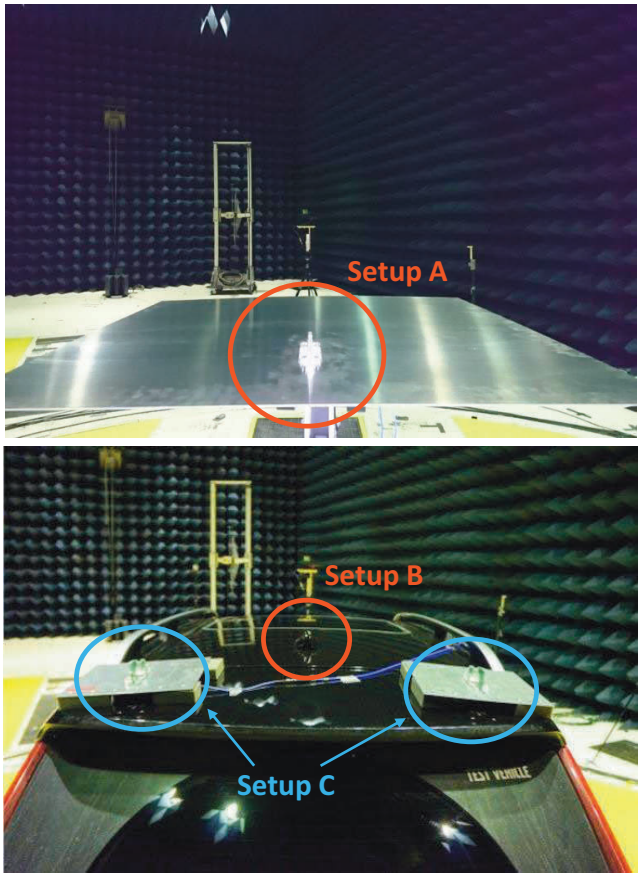

Fig. E.4: Photos of the three DUT setups.

the test zone is approximately proportional to the number of OTA probes [2]. Therefore, the 8P, 16P, and 32P MPAC setups correspond to the test zones of about 12 cm, 24 cm, and 48 cm in diameter at the testing frequency, respectively, all of which are smaller than the maximum physical dimensions of the three DUT setups in the measurements.

The values of the average received power and the branch power ratio under the target and the emulated channel for the three DUT setups are summarized in Table E.2. We can see that both the average received power and the branch power ratio under the emulated channel are quite close to the target values with a deviation up to around 1 dB, except for a deviation of around 2 dB in the branch power ratio for Setup B under the UMa scenario with the 8P MPAC setup.

The target and the emulated antenna correlation, i.e. ρ and $\hat{\rho}$, are shown

Table E.2: The Average Received Power and the Branch Power Ratio of the Target and the Emulated Channel with the Synthetic 8-probe (8P), 16-probe (16P), and 32-probe (32P) MPAC Setup (unit: [dB]).

SCME UMa															
	Setup A					Setup B					Setup C				
	8P	16P	32P	Target	Dev.	8P	16P	32P	Target	Dev.	8P	16P	32P	Target	Dev.
$\bar{P}_1$	−8.61	−8.59	N/A	−8.68	0.09	−7.84	−7.84	N/A	−6.70	1.14	−8.24	−8.46	−9.15	−8.62	0.53
$\bar{P}_2$	−9.10	−9.16	N/A	−8.99	0.17	−5.64	−6.08	N/A	−6.50	0.86	−2.82	−1.38	−1.68	−2.09	0.73
$\Delta\bar{P}$	0.49	0.57	N/A	0.31	0.26	2.20	1.76	N/A	0.20	2.00	5.42	7.08	7.46	6.53	1.11
SCME UMi															
	Setup A					Setup B					Setup C				
	8P	16P	32P	Target	Dev.	8P	16P	32P	Target	Dev.	8P	16P	32P	Target	Dev.
$\bar{P}_1$	−9.36	−9.16	N/A	−9.34	0.18	−7.34	−8.42	N/A	−7.58	0.84	−6.38	−5.94	−6.83	−6.47	0.53
$\bar{P}_2$	−8.55	−8.34	N/A	−8.31	0.24	−7.42	−7.90	N/A	−7.90	0.48	−6.87	−5.43	−5.68	−5.97	0.90
$\Delta\bar{P}$	0.81	0.82	N/A	1.02	0.21	0.07	0.52	N/A	0.32	0.25	0.49	0.51	1.14	0.49	0.65

*The values (marked in red) are for the emulated channels with the largest deviation to the corresponding target values (marked in blue).

**"Dev." denotes the absolute value of the largest deviation.

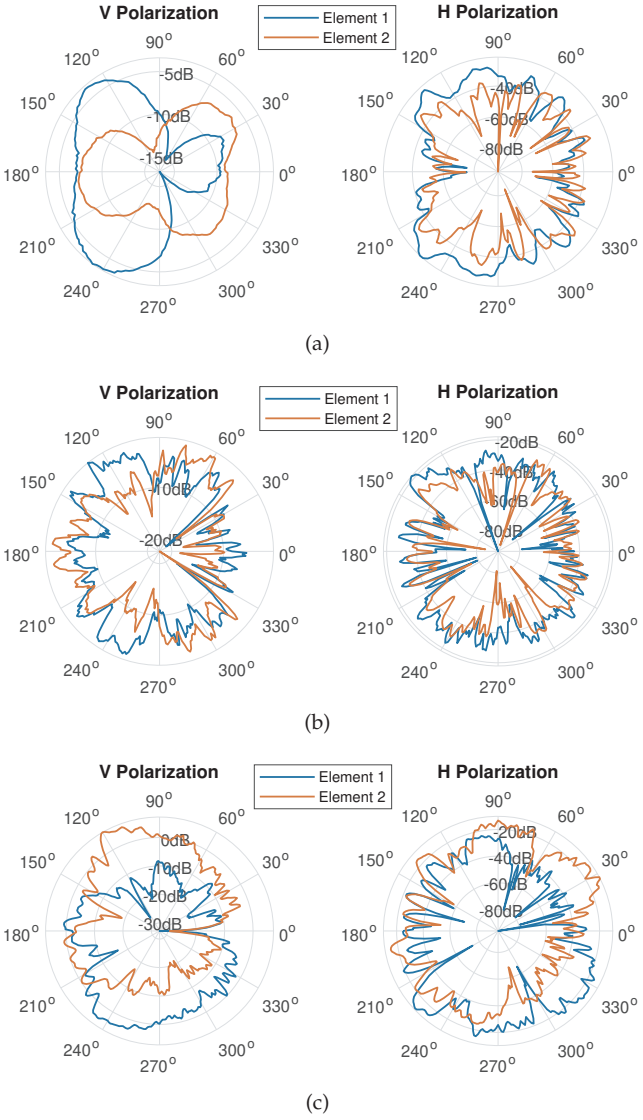

Fig. E.5: Measured antenna radiation pattern for (a) Setup A, (b) Setup B, and (c) Setup C.

in the complex plane in Fig. E.6 for the three DUT setups under the UMa and the UMi scenario. The deviation $|\rho - \hat{\rho}|$ against the number of OTA probes is further shown in Fig. E.7. For Setup A (supposedly with the smallest effective antenna distance), the antenna correlation deviation is very small for different numbers of OTA probes with a deviation of about 0.03 for the 8P MPAC setup under the UMi scenario. For Setup B (supposedly with a

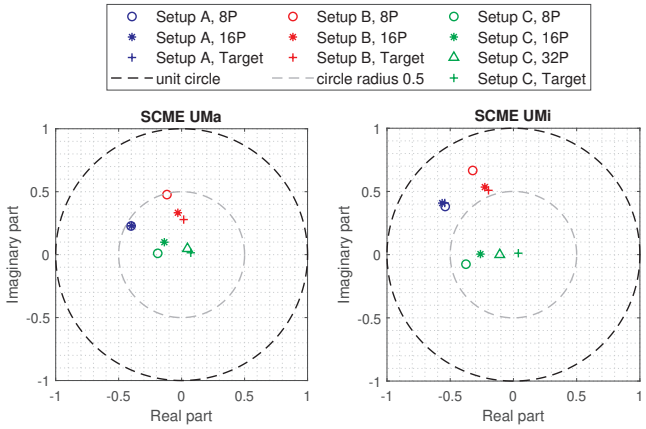

Fig. E.6: DUT antenna correlation for the target and the emulated channel under (left) the SCME UMa scenario and (right) the SCME UMi scenario.

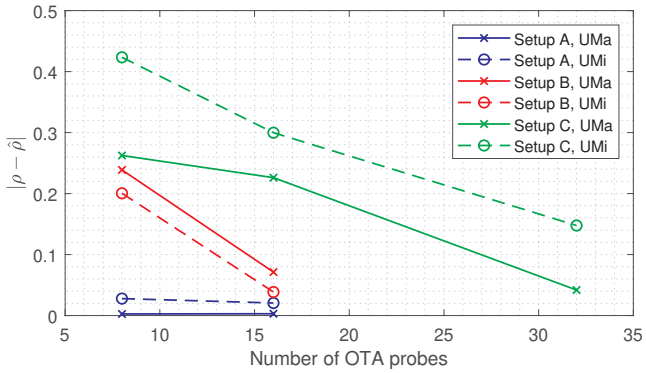

Fig. E.7: Difference of the DUT antenna correlation between the target and the emulated channel under the UMa and UMi scenarios.

median effective antenna distance), the emulated antenna correlation poses a deviation of about 0.2 with the 8P MPAC setup, but it approaches the target with the 16P MPAC setup. This indicates that the 8P MPAC setup is not capable of accurately emulating the target spatial profile on the DUT side for Setup B. For Setup C (supposedly with the largest effective distance), the antenna correlation deviation decreases significantly with the increase of the number of OTA probes. This is expected since a larger number of OTA probes results in a larger size of the test zone. However, similar to Setup B, the 8P MPAC is not capable of accurately emulating the target spatial profile on the DUT side for Setup C with an antenna correlation deviation of over 0.4 under the UMi scenario. Note that the three metrics under the 32P MPAC setup are not shown for Setup A and Setup B since the antenna correlation

deviation $|\rho - \hat{\rho}|$ is already very small (below 0.1) for these two cases with the 8P and 16P MPAC setup, respectively (see Fig. E.7).

4.2 Verification for the Wireless Cable Method

In our measurements, the amplitude of w_1 and w_2 was fixed to unity, and only their phase was tuned within the range $[-200^\circ, 200^\circ]$ to establish the wireless cable connections. The RSRP_u with $u = \{1, 2\}$ was recorded against the phase of w_1 and w_2 as shown in Fig. E.8. The red and the magenta circles denote the selected phase of w_1 and w_2 for the wireless cable connections with the maximum isolation level, respectively. A lowest isolation level of $\eta_2 = 6\,\text{dB}$ was achieved for the wireless cable connection to the second Rx antenna in Setup B, whereas a highest isolation level of $\eta_1 = 22.1\,\text{dB}$ was achieved for the connection to the first Rx antenna in Setup C. Note that in the standard [1], an isolation level of 18 dB is recommended for wireless cable connections; otherwise, interference from other wireless cable connections may influence the measurement results. Therefore, the throughput results for Setup A ($\eta_2 = 9.2\,\text{dB}$) and Setup B ($\eta_2 = 6\,\text{dB}$) might have suffered from a relatively high interference in the measurements. The low isolation that occurred in the measurements can be due to the phase-only tuning of $\boldsymbol{W}$ instead of both amplitude and phase tuning for establishing the wireless cable connections. Another possible cause is that the transfer function $\boldsymbol{L}$ was ill-conditioned, as the low isolation occurred for the two similar DUT setups, i.e. Setup A and Setup B, where the antenna element spacing is small.

4.3 Throughput Results Analysis

Throughput is a high-level metric which reflects the end-user experience directly. It is also used as a measure to check the validity of different OTA methods [1]. In our case, the throughput performance is compared between the MPAC and the wireless cable method. The throughput measurements with the MPAC and the wireless cable method were done according to the standard MIMO OTA testing procedure described in [1]. The measurement results are shown in Fig. E.9.

For the UMa scenario (the solid curves), the throughput results are in good agreement between the MPAC and the wireless cable method for Setup B and Setup C. The result of Setup A with the wireless cable method probably indicates a failed measurement due to some practical issues during the measurements, given the observation that the resulting throughput did not reach 100% even with a significantly high signal power (i.e. with $-75\,\text{dBm}$ RSRP). As mentioned in Appendix 4.1, the 8P MPAC setup is not capable of accurately emulating the target channel for Setup B and Setup C. However, no significant difference in the measured throughput results between

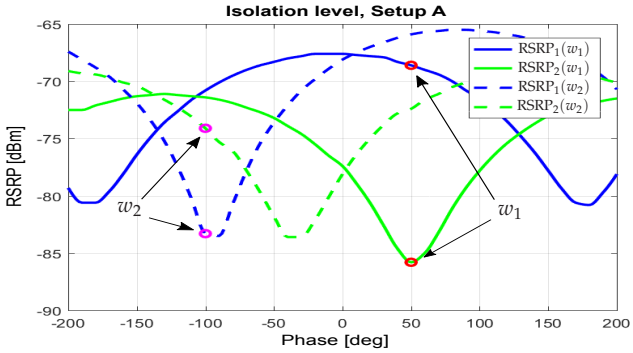

(a)

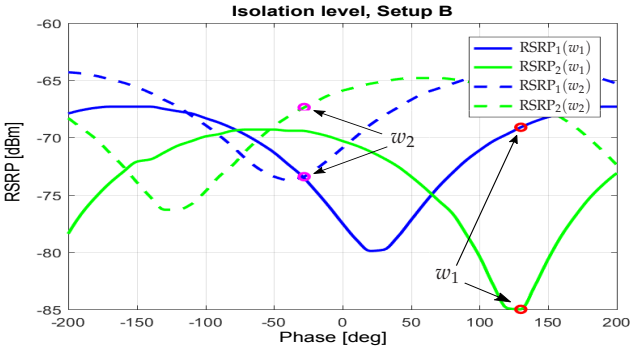

(b)

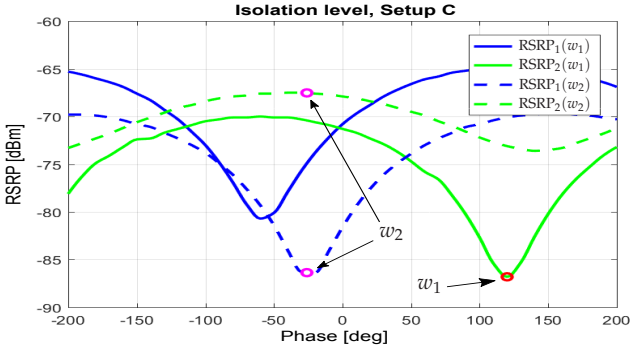

(c)

Fig. E.8: Wireless cable connection established for (a) Setup A with an isolation level of 17.2 dB for the first Rx antenna and 9.2 dB for the second Rx antenna; (b) Setup B with an isolation level of 14.3 dB for the first Rx antenna and 6 dB for the second Rx antenna; (c) Setup C with an isolation level of 22.1 dB for the first Rx antenna and 19 dB for the second Rx antenna.

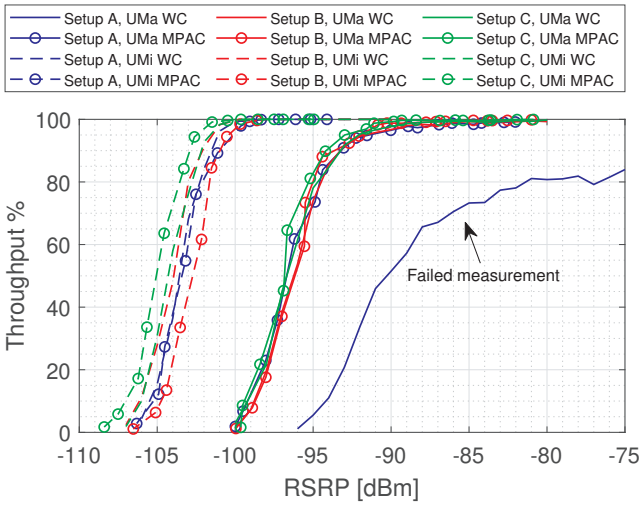

Fig. E.9: Measured relative throughput against RSRP for the three DUT setups with the MPAC and the wireless cable (WC) method with 100% throughput corresponding to 35.424 Mbps.

the MPAC and the wireless cable method is observed. This is probably due to the high antenna correlation at the BS side (i.e. 0.9 in magnitude) under the UMa scenario, which leads to an ill-conditioned target MIMO channel, and hence the throughput results are not sensitive to the antenna correlation at the DUT side [24]. Therefore, even when the antenna correlation deviation for the 8P MPAC setup is high (e.g. about 0.25 for Setup B, see Fig. E.7), the emulation error is not reflected in the throughput results. Moreover, the measured throughput results are very similar among the three DUT setups for the same reason.

For the UMi scenario (the dashed curves), the throughput results are still in reasonably good agreement between the MPAC and the wireless cable method. Relatively large difference in the throughput results can be seen for Setup B and Setup C between the MPAC and the wireless cable method (e.g. with a difference up to 1.5 dB in RSRP for Setup B). In contrast to the UMa scenario, the magnitude of the antenna correlation at the BS side is 0.01 for the UMi scenario. Therefore, the throughput results are more dependent on the antenna correlation at the DUT side. Consequently, the emulation error of the 8P MPAC setup is more noticeable under the UMi scenario in terms of the difference between the throughput results of the MPAC and the wireless cable method. However, it is interesting to point out that with an emulation deviation of around 0.4 in antenna correlation for Setup C under the UMi scenario (see Fig. E.7), a relatively small difference of up to around 1 dB in RSRP is observed between the MPAC and the wireless cable method. It was found in [24] that antenna correlation deviation does not have a significant

effect on throughput if the magnitudes of both the target and the emulated antenna correlation are below 0.5 under the UMi scenario, which explains the observation in our case.

Comparing the results between the UMa and the UMi scenarios, we can also see that the required RSRP for the same throughput percentage under the UMi scenario is always lower than that under the UMa scenario by about 5 dB for all three DUT setups, which indicates that a better throughput performance was achieved under the UMi scenario. This complies with our expectation due to the lower antenna correlation at the BS side for the UMi scenario [1], which is beneficial for spatial multiplexing for MIMO systems, and hence improves the throughput performance. Moreover, Setup C results in the best throughput performance under the UMi scenario as expected since the corresponding antenna correlation is the smallest among the three DUT setups (see Fig. E.6).

In general, the difference in the throughput results between different DUT setups for each scenario is small. This is caused jointly by the underlying DUT antenna radiation pattern and the channel models. It can be inferred that the throughput is not very sensitive to the DUT setups and their respective emulation error in our measurement. Other types of DUT antennas and channel models can be considered to reflect more significantly their effect on the throughput.

4.4 Discussion on the MPAC and the Wireless Cable Setup for Car Testing

The MPAC setup is a true end-to-end MIMO OTA testing method. However, it suffers from a high system cost with the increase of the required test zone for large DUTs. As shown in Fig. E.7, a 32P MPAC setup may be just adequate to emulate the target channel accurately, as for Setup C. The wireless cable setup may result in a lower cost compared to the MPAC setup, since the number of OTA probes for the wireless cable setup is not related to the size of the DUT but the number of the DUT antennas. However, due to the two-stage principle of the wireless cable setup, the DUT antenna radiation pattern is numerically implemented in the channel emulator. Therefore, the wireless cable setup is not for true end-to-end testing in principle. If DUT antenna patterns are non-adaptive as in the measurements, the wireless cable setup can approximate the true end-to-end testing. From the throughput results shown in Fig. E.9, no significant difference in measured throughput between the MPAC and the wireless cable setup has been observed (except for the failed measurement). Therefore, the more cost-effective wireless cable setup is recommended for MIMO OTA testing for cars with non-adaptive DUT antenna patterns.

5 Conclusion

In this paper, the principles of two MIMO OTA testing methods, i.e. the MPAC and the wireless cable method, have been briefly revisited. One key question for performance testing for cars with the MPAC method is that to which extent the presence of vehicles will affect the required size of the test zone. Three DUT antenna setups are considered in the study, i.e. a two-element shark-fin antenna mounted on a 1 m $\times$ 1 m ground plane (Setup A), a two-element shark-fin antenna on a car roof (Setup B), and two shark-fin antennas on the sides of the car roof with one element for each antenna being used (Setup C). The effect of the large ground plane and the car is accounted in the measured DUT antenna radiation pattern.

From the emulation accuracy point of view, different numbers of OTA probes do not lead to much deviation in the resulting average received power and branch power ratio with respect to the target values (with a deviation up to around 1 dB). However, by the metric of the antenna correlation at the DUT side, the target channels can be well emulated with the 8P MPAC setup for the DUT Setup A, whereas more OTA probes (i.e. the 16P and the 32P MPAC setups) are needed for the DUT Setup B and Setup C, respectively. It can be inferred that the MPAC setup is capable of car testing but 16 or 32 OTA probes will be needed for a DUT antenna setup with large effective antenna distances to maintain a high emulation accuracy.

Moreover, throughput measurements have been performed with the 8P MPAC and the wireless cable setup under SCME UMa and UMi scenarios. A better throughput performance has been observed under the UMi scenario as expected. Except for the failed measurement, the throughput results from the MPAC and the wireless cable method are in good agreement (with a difference up to 1.5 dB in RSRP for Setup B under the UMi scenario). Furthermore, a better agreement is observed under the UMa scenario, due to the high antenna correlation of 0.9 in magnitude at the BS side under the UMa scenario, which results in an ill-conditioned MIMO channel. Hence the emulation error with the 8P MPAC setup in the antenna correlation at the DUT side does not affect the resulting throughput as much as it does under the UMi scenario. Given the similarity of the throughput results between the MPAC and the wireless cable setup, the more cost-effective wireless cable setup is recommended for car testing with non-adaptive DUT antenna patterns.

References

[1] 3GPP, "Verification of radiated multi-antenna reception performance of User Equipment (UE)," Tech. Rep. 3GPP TR 37.977 V15.0.0, 2018.

[2] P. Kyösti, T. Jämsä, and J.-P. Nuutinen, "Channel modelling for multiprobe over-the-air MIMO testing," *International Journal of Antennas and Propagation*, vol. 2012, 2012.

[3] W. Fan, P. Kyösti, L. Hentilä, and G. F. Pedersen, "MIMO Terminal Performance Evaluation With a Novel Wireless Cable Method," *IEEE Transactions on Antennas and Propagation*, vol. 65, no. 9, pp. 4803–4814, 2017. [Online]. Available: http://ieeexplore.ieee.org/document/7967858/

[4] X. Chen, J. Tang, T. Li, S. Zhu, Y. Ren, Z. Zhang, and A. Zhang, "Reverberation Chambers for Over-the-Air Tests: An Overview of Two Decades of Research," *IEEE Access*, vol. 6, pp. 49 129–49 143, 2018. [Online]. Available: https://ieeexplore.ieee.org/document/8447191/

[5] D. Micheli, M. Barazzetta, R. Diamanti, P. Obino, R. Lattanzi, L. Bastianelli, V. M. Primiani, and F. Moglie, "Over-The-air tests of high-speed moving LTE users in a reverberation chamber," *IEEE Transactions on Vehicular Technology*, vol. 67, no. 5, pp. 4340–4349, 2018.

[6] 3GPP, "Study on LTE Support for V2X Services," Tech. Rep. 3GPP TR 22.885 V1.0.0, 2015.

[7] M. G. Nilsson, P. Hallbjörner, N. Arabäck, B. Bergqvist, T. Abbas, and F. Tufvesson, "Measurement Uncertainty, Channel Simulation, and Disturbance Characterization of an Over-the-Air Multiprobe Setup for Cars at 5.9 GHz," *IEEE Transactions on Industrial Electronics*, vol. 62, no. 12, pp. 7859–7869, 2015.

[8] P. Berlt, C. Bornkessel, and M. A. Hein, "Spatial Correlation of C-V2X Antennas Measured in the Virtual Road Simulation and Test Area," in *12th European Conference on Antennas and Propagation (EuCAP 2018)*, 2018, pp. 1–5.

[9] C. Schirmer, M. Lorenz, W. A. Kotterman, R. Perthold, M. H. Landmann, and G. Del Galdo, "MIMO over-the-air testing for electrically large objects in non-anechoic environments," in *2016 10th European Conference on Antennas and Propagation, EuCAP 2016*. European Association of Antennas and Propagation, 2016, pp. 1–6.

[10] M. Schilliger Kildal, J. Kvarnstrand, J. Carlsson, A. A. Glazunov, A. Majidzadeh, and P.-S. Kildal, "Initial Measured OTA Throughput of 4G LTE Communication to Cars with Roof-Mounted Antennas in 2D Random-LOS," in *2015 International Symposium on Antennas and Propagation (ISAP)*, 2015, pp. 1–4.

[11] M. S. Kildal, J. Carlsson, and A. Alayon Glazunov, "Measurements and simulations for validation of the random-LOS measurement accuracy for vehicular OTA applications," *IEEE Transactions on Antennas and Propagation*, vol. 66, no. 11, pp. 6291–6299, 2018.

[12] A. Razavi, A. A. Glazunov, P. S. Kildal, and R. Maaskant, "Array-fed cylindrical reflector antenna for automotive OTA tests in Random Line-Of-Sight," in *2016 10th European Conference on Antennas and Propagation, EuCAP 2016*, 2016, pp. 3–6.

[13] R. K. Sharma, C. Schneider, W. Kotterman, G. Sommerkorn, P. Grosse, F. Wollenschlager, G. Del Galdo, M. A. Hein, and R. S. Thoma, "Over-the-air testing of Car-to-Car and car-to-infrastructure communication in a virtual electromagnetic

environment," in *IECON Proceedings (Industrial Electronics Conference)*, 2013, pp. 6897–6902.

[14] M. G. Nilsson, C. Gustafson, T. Abbas, and F. Tufvesson, "A Measurement-Based Multilink Shadowing Model for V2V Network Simulations of Highway Scenarios," *IEEE Transactions on Vehicular Technology*, vol. 66, no. 10, pp. 8632–8643, 2017.

[15] ——, "A path loss and shadowing model for multilink vehicle-to-vehicle channels in urban intersections," *Sensors*, vol. 18, no. 12, pp. 1–19, 2018.

[16] D. S. Baum, J. Hansen, G. D. Galdo, and M. Milojevic, "An Interim Channel Model for Beyond-3G Systems," *Vehicular Technology Conference, 2005. VTC 2005-Spring. 2005 IEEE 61st*, vol. 5, pp. 3132–3136, 2005.

[17] 3GPP, "Spatial channel model for Multiple Input Multiple Output (MIMO) simulations," Tech. Rep. 3GPP TR 25.996 V12.0.0, 2014.

[18] WINNER, "WINNER II Channel Models: Part I Channel Models," Tech. Rep. D1.1.2 V1.2, 2007. [Online]. Available: http://projects.celtic-initiative.org/WINNER+/WINNER2-Deliverables/D4.6.1.pdf

[19] 3GPP, "Study on channel model for frequencies from 0.5 to 100 GHz," Tech. Rep. 3GPP TR 38.901 V14.0.0, 2017. [Online]. Available: http://www.etsi.org/standards-search

[20] P. Bello, "Characterization of Randomly Time-Variant Linear Channels," *IEEE Transactions on Communications Systems*, vol. 11, no. 4, pp. 360–393, 1963. [Online]. Available: http://ieeexplore.ieee.org/xpls/abs{_}all.jsp?arnumber=1088793{&}tag=1

[21] Y. Ji, W. Fan, G. F. Pedersen, and X. Wu, "On Channel Emulation Methods in Multiprobe Anechoic Chamber Setups for Over-the-Air Testing," *IEEE Transactions on Vehicular Technology*, vol. 67, no. 8, pp. 6740–6751, 2018.

[22] W. Fan, P. Kyösti, Y. Ji, L. Hentilä, X. Chen, and G. F. Pedersen, "Experimental Evaluation of User Influence on Test Zone Size in Multi-Probe Anechoic Chamber Setups," *IEEE Access*, vol. 5, pp. 18 545–18 556, 2017.

[23] 3GPP, "Evolved Universal Terrestrial Radio Access (E-UTRA); User Equipment (UE) radio transmission and reception," Tech. Rep. 3GPP TS 36.101 V15.7.0, 2019.

[24] W. Fan, L. Hentilä, P. Kyösti, and G. F. Pedersen, "Test Zone Size Characterization with Measured MIMO Throughput for Simulated MPAC Configurations in Conductive Setups," *IEEE Transactions on Vehicular Technology*, vol. 66, no. 11, pp. 10 532–10 536, 2017. [Online]. Available: http://ieeexplore.ieee.org/document/7981384/

ISSN (online): 2446-1628
ISBN (online): 978-87-7210-661-8

AALBORG UNIVERSITY PRESS